

pubs.acs.org/JPCC Article

# Nanoparticle Formation Kinetics, Mechanisms, and Accurate Rate Constants: Examination of a Second-Generation $Ir(0)_n$ Particle Formation System by Five Monitoring Methods Plus Initial Mechanism-Enabled Population Balance Modeling

Christopher B. Whitehead, Derek R. Handwerk, Patrick D. Shipman, Yuanyuan Li, Anatoly I. Frenkel, Bridget Ingham, Nigel M. Kirby, and Richard G. Finke\*



Cite This: J. Phys. Chem. C 2021, 125, 13449-13476



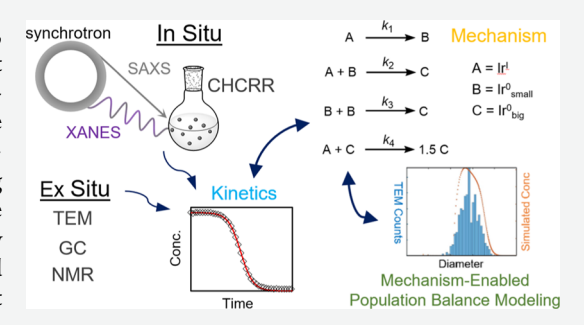
**ACCESS** 

Metrics & More

Article Recommendations

Supporting Information

**ABSTRACT:** The kinetics and mechanism of a second-generation iridium, bimetallic  $\{[(1,5\text{-COD})\text{Ir}^1\text{-HPO4}]_2\}^{2^-}$  nanoparticle precursor system that produces  $\text{Ir}(0)_{\sim 150^{\circ}}(\text{HPO}_4)_x$  nanoparticles are investigated herein. Specifically, a list of seven open questions is addressed via a total of five experimental techniques used to monitor the kinetics of the  $\{[(1,5\text{-COD})\text{Ir}^1\text{-HPO4}]_2\}^{2^-}$  system plus mechanism-enabled population balance modeling (ME-PBM), hence six total methods. To start, an indirect but in-house cyclohexene catalytic reporter reaction monitoring method is used to follow the formation of the catalytically active  $\text{Ir}(0)_n$ . Next, gas—liquid chromatography is used to quantify the amount of cyclooctane product formed versus time as a second way to monitor the loss of the  $\{[(1,5\text{-COD})\text{Ir}^1\text{-HPO4}]_2\}^{2^-}\}$ 



COD)Ir<sup>I</sup>·HPO4]<sub>2</sub>}<sup>2-</sup> precatalyst. Synchrotron X-ray absorption near-edge structure is used next to more directly monitor the reduction of Ir<sup>I</sup> to Ir<sup>0</sup>, and small-angle X-ray scattering is employed in separate experiments at a second synchrotron to monitor the formation of Ir(0)<sub>n</sub> versus time. Transmission electron microscopy (TEM) on reaction aliquots is used to determine the particle size distribution (PSD) versus time. The experimental kinetics data are then fit and analyzed to start using a minimal, two-step mechanism of nucleation,  $A \rightarrow B$  (rate constant  $k_1$ ), and autocatalytic growth,  $A + B \rightarrow 2B$  (rate constant  $k_2$ ). How well the rate constants agree between the various methods is addressed as is the overall estimated accuracy of the kinetics in light of the multiple methods employed to monitor the particle formation kinetics. ME-PBM is then used to analyze the TEM PSD data versus time, specifically to answer the question of whether or not the minimum mechanism consistent with all the kinetic data from the five physical methods can explain the observed PSD? An important finding is that it cannot. The Discussion section returns to the seven primary questions posed in the Introduction and includes 16 recommendations for future studies. A Conclusions section is also provided in this final experimental study from our group of prototype Ir(0)<sub>n</sub> nanoparticle formation kinetics and mechanisms.

## 1. INTRODUCTION

Metal nanoparticles are known for their catalytic<sup>1-6</sup> and medicinal<sup>7,8</sup> applications. These properties are connected to the particle size and size distributions, which can be tuned through ligands<sup>9-11</sup> and reaction conditions.<sup>12,13</sup> To control the final particle size and size distribution, one needs to fully understand the particle formation processes—that is, the mechanism—of nucleation, growth, and any possible agglomeration.

**1.1. Minimal, Disproof-Based Mechanisms for Particle Formation.** Deliberately minimalist (i.e., Ockham's razor<sup>14</sup> obeying), disproof-based<sup>15–17</sup> mechanisms for particle formation are of considerable current interest because such mechanisms can inform rational particle syntheses. Mechanism-designed syntheses can, in turn, control particle size and size distributions<sup>18,19</sup> of interest in a myriad of applications of nanoparticles and nanocrystals.<sup>20–24</sup> For this reason, the

kinetics and mechanisms of particle formations,  $^{25-33}$  as well as the use of multiple, ideally direct physical methods  $^{34-42}$  to follow the particle formations in real time, continue to be of current interest.  $^{26-33}$  Despite this interest, the work that follows is an example of only a few studies in the literature where  $\geq 3$  multiple, direct, or indirect methods are used to follow the kinetics of nanoparticle nucleation and growth  $^{43,44}$  and only the second example where the powerful, mechanism-checking tool of mechanism-enabled population balance modeling (ME-PBM) has been employed.  $^{18,19}$ 

Received: April 18, 2021 Revised: May 4, 2021 Published: June 9, 2021





1.2. First-Generation, Extensively Studied {(1,5-COD)- $Ir^{I}$ -POM}<sup>8-</sup> Nanoparticle Formation System. Extensive studies of a first-generation {(1,5-COD)Ir<sup>I</sup>.POM}<sup>8-</sup> precursor system<sup>45,46</sup> (POM = polyoxometalate) are responsible for the minimum, disproof-based kinetics and mechanisms summarized in Scheme 1. The {(1,5-COD)Ir<sup>I</sup>.POM}<sup>8-</sup> precursor

Scheme 1. Fast CHCRR Monitoring Method and a Minimalistic Two-Step Mechanism<sup>52</sup> Used as a Starting Point for the Analysis of the Kinetic Data

Cyclohexene Hydrogenation Catalytic Reporter Reaction Monitoring Method

2-Step Mechanism

system self-assembles n equiv of  $\{(1,5\text{-COD})\text{Ir}^1\text{-POM}\}^{8-1}$  under  $H_2$  typically in acetone (alternatively sometimes in propylene carbonate<sup>47</sup>) solvent to yield well-formed, highly (polyoxometalate) stabilized  $\text{Ir}(0)_n \cdot (\text{POM}^{9-1})_x$  nanoparticles, such as  $\text{Ir}(0)_{\sim 300} \cdot (\text{POM}^{9-1})_x$  ( $x \sim 17$ )<sup>45</sup> in acetone, where POM is  $\text{POM}^{9-1} = P_2 W_{15} \text{Nb}_3 O_{62}^{9-1}$ . Eq 1 is the experimentally established, balanced reaction stoichiometry. Eq. (1)

$$n \{(1,5\text{-COD})|r^1\text{-POM}\}^{8-} + 2.5n \text{ H}_2$$

$$|r(0)_{\sim n}\text{-}(POM^{9-})_X + (n-x)POM^{9-} + n + n \text{ H}^+ \text{ (Eq 1)}$$

A custom-built<sup>48</sup> sterically bulky, highly negatively charged, "electrosteric" 49 POM9- "Gold standard" nanoparticle stabilizer affords five outstanding features and five advantages to the  $Ir(0)_n \cdot (POM^{9-})_x$  nanoparticle system (as summarized in p 2850 elsewhere<sup>63</sup> as well as in the Supporting Information). However, despite the positives of the {(1,5-COD)Ir<sup>I</sup>·POM}<sup>8-</sup> precursor and the resultant  $Ir(0)_n \cdot (POM^{9-})_r$  nanoparticle system, two significant limitations of this classic system (discussed more elsewhere 63) directly relevant to the present contribution are the following: (i) the large, ca. 1.2 nm width by ca. 1.5 nm length of the cigar-shaped POM, P<sub>2</sub>W<sub>15</sub>Nb<sub>3</sub>O<sub>62</sub><sup>9-</sup>, interferes with small-angle X-ray scattering (SAXS) observation of early nucleation events. Those early nucleation clusters can easily be below 1.0 nm, as for example, as modeled by a crystallographically characterized tetrairidium-hydride,  $Ir_4H_4(1,5-COD)_4$  cluster<sup>50,51</sup> that is 0.8  $\pm$ 0.1 nm by SAXS observation control experiments (performed in collaboration with Karim and his group 9,32,39). An additional limitation of the {(1,5-COD)Ir<sup>I</sup>·POM}<sup>8-</sup> system is (ii) that W in the POM interferes with the Ir X-ray absorption fine structure (XAFS) (specifically, the overlap of the W L<sub>2</sub>-edge with the preferred Ir L3-edge). Hence, there was a need to develop a second-generation  $Ir(0)_n$  nanoparticle system that retained the multiple advantages of the IrI(1,5-COD)+ precursor system, yet replaced the POM9- polyoxometalate stabilizer by a smaller but still effective polyanionic stabilizer. Those studies were started back in 2003 and will be summarized in a moment, after some additional, necessary background material is covered.

1.3. Cyclohexene Catalytic Hydrogenation Reporter Reaction Methodology. In 1994, we developed 45,46 a way to monitor in-house—and hence routinely and rapidly albeit indirectly—the formation of  $Ir(0)_n$  and other catalytically active nanoparticles shown in the equations below, a method we expanded and refined in a 1997 paper. 52 The method involves exploiting the perhaps single most important concept in studying modern, complex, multistep reactions kinetically and mechanistically, namely, the pseudo-elementary step (PEStep) concept. 52,53 In a PEStep, multiple steps—sometimes thousands of steps, as in the case of nanoparticle formation—are summed and thereby condensed into and represented kinetically by composite, "pseudo-elementary" 52,53 steps, such as the A  $\rightarrow$  B and A + B  $\rightarrow$  2B two-step minimum mechanism<sup>52</sup> shown in Scheme 1. There, the PEStep concept<sup>52,53</sup> and fast cyclohexene hydrogenation catalysis by the resultant Ir(0), nanoparticles are used to monitor the nanoparticle formation reaction indirectly, but in real time and with thousands of data points from a high-precision, ±0.01 psig pressure transducer monitoring the loss of H<sub>2</sub>, as detailed in Scheme 1.

$$A \xrightarrow{R_1} B$$
 (Eq 2)

$$A + B \xrightarrow{\frac{n_2}{H_2}} 2B$$
 (Eq 3)

~500 
$$\begin{bmatrix} B + \bigcirc + H_2 & \xrightarrow{fast} B + \bigcirc + H \end{bmatrix}$$
 (Eq 4)

SUM: A + ~500 
$$\bigcirc$$
 + ~500 H<sub>2</sub>  $\xrightarrow{k_{\text{obs}}}$  B + ~500  $\bigcirc$  H (Eq.5)

The mathematical derivation and details behind the use of the above PESteps have been available since 1997. The key part for monitoring the catalytically active particle formation is that eq 5 allows one to write the differentials shown in eq 6 (i.e., under certain conditions,  $^{52}$  notably an excess of cyclohexene and  $H_2$  compared to A).

$$\frac{\left(-\frac{d[A]}{dt}\right)}{1} = \frac{\left(+\frac{d[B]}{dt}\right)}{1} = \frac{\left(-\frac{d[cyclohexene]}{dt}\right)}{500}$$

$$= \frac{\left(+\frac{d[cyclohexane]}{dt}\right)}{500}$$
(6)

Equation 6 teaches that one can in turn monitor the loss of  $H_2$  by a pressure transducer due to the fast catalytic hydrogenation of cyclohexene, yet actually be following kinetically the slow steps of nanoparticle formation. In the above case in eq 1, the slow steps are nucleation (represented minimalistically by the PEStep A  $\rightarrow$  B) and autocatalytic surface growth (represented minimalistically by the PEStep A + B  $\rightarrow$  2B). Normally, the excess of cyclohexene to Ir precursor is 500–1500 equiv, shown as 500 in the denominator of eq 6 because that will apply to the studies examined in the present work.

That the PEStep and cyclohexene hydrogenation catalytic reporter reaction (CHCRR) monitoring methods work at least semiquantitatively was confirmed first in  $^{52}$  1997, and many times since,  $^{54}$  by (i) control experiments showing that the kinetics are of zero-order in cyclohexene (i.e., [cyclohexene] $^0$ ), so that the hydrogenation reporter reaction step must be fast compared to the nanoparticle formation PESteps of A  $\rightarrow$  B and

Scheme 2. Deliberately Minimalistic, Ockham's Razor-Obeying Mechanistic PESteps<sup>52,53</sup> for Particle Formation in A (=Precursor), B (=on Average "Smaller Particles"), and C (=on Average "Larger Particles") Generalized Form; Adapted from Ref 18 with Permission; Copyright 2019 American Chemical Society

Pseudo-elementary Steps (in a more generalized form) Pictorial representation (for smaller, initial clusters)

(1) 
$$A \xrightarrow{k_1} B$$
  $Ir^1 \xrightarrow{k_1} Ir^0$   $\Rightarrow x_1 = x_2 \xrightarrow{k_1} Ir^0 = x_2 \xrightarrow{k_1} Ir^0 = x_2 \xrightarrow{k_1} Ir^0 = x_2 \xrightarrow{k_2} Ir^0 = x_1 \xrightarrow{k_2} Ir^0 = x_2 \xrightarrow{k_1} Ir^0 = x_2 \xrightarrow{k_2} Ir^0 = x_2 \xrightarrow{k_2} Ir^0 = x_2 \xrightarrow{k_1} Ir^0 = x_2 \xrightarrow{k_2} Ir^0 = x_2 \xrightarrow{k_2} Ir^0 = x_2 \xrightarrow{k_1} Ir^0 =$ 

 $A + B \rightarrow 2B$ . These two PESteps are, then, actually controlling the observed kinetics. Additionally, (ii) controls were done independently monitoring the reaction somewhat more directly via the evolution of cyclooctane (COA) (see eq 1, vide supra), controls that confirm the sigmoidal shape of the kinetic curves and also yielded rate constants within experimental error of those from the CHCRR.<sup>52</sup>

The CHCRR kinetic methodology has since allowed ≥1500 kinetic experiments to be done routinely and in-house by 11 different researchers over a period of ≥23 years. Even though the PEStep and CHCRR methodologies have been available since 1997 and have been used and discussed many times before, 52,63 details are presented in the Supporting Information as a convenience to the reader who might not be familiar with the CHCRR and PEStep methodologies. We will see that the results obtained herein document that such in-house methods, even if indirect, can be an important addition to and compliment of synchrotron-radiation-based methods.

For some time now, we have had studies in progress striving to test the CHCRR methodology and resultant mechanisms even further, especially as presented herein by more direct, synchrotron-radiation-based methods. In that regard, the present contribution is the result of the multiyear effort that started in 2003 with the synthesis and development of a second-generation  $\{[(1,5\text{-COD})\text{Ir}^{\text{I}}\cdot\text{HPO}_4]_2\}^{2-}$  system, <sup>55</sup> vide infra, employed herein that overcomes the two main limitations of the first-generation {(1,5-COD)Ir<sup>I</sup>·POM}<sup>8-</sup> system by allowing the use of synchrotron XAFS and SAXS methods. The present contribution is also the result of two separate collaborations using synchrotrons on two continents as well as our on-going collaboration with mathematicians in developing and employing ME-PBM. Perhaps, the most interesting question addressed herein is whether or not the five physical methods, including two synchrotron methods, are sufficient to obtain the more detailed, reliable nanoparticle formation mechanism in a second-generation system studied at the state-of-the-art that includes five physical methods, rare knowledge of the nucleation mechanism, 63 as well as checking by ME-PBM. 18,19

1.4. Minimum, Disproof-Based Mechanisms for Particle Formation. The primary PEStep-based minimum mechanisms for particle formation 47,52,54,56-63 needed to

enable ME-PBM and that have been discovered over time using the first-generation  $\{(1,5\text{-COD})\text{Ir}^{1}\text{-POM}\}^{8-}$  precursor to  $\text{Ir}(0)_{n}\cdot(\text{POM}^{9-})_{x}$  system are shown in Scheme 2, <sup>18</sup> illustrated there for that prototype, first-generation  $Ir(0)_n$  nanoparticle system. The proposed mechanisms are based on experimentally established, full, balanced reaction stoichiometries (e.g., Scheme 2). TEM product versus time data, extensive CHCRR kinetic data, and multiple controls and checks where possible such as COA evolution kinetic data obtained by gas-liquid chromatography (GLC).

The PESteps presented in Scheme 1 were uncovered through the extensive study of the first-generation Ir system, 47,52,54,56-63 and specifically by: (i) elucidating the reaction speciation; (ii) establishing experimentally the balanced reaction stoichiometry; (iii) collecting the TEM-based particle-size distribution (PSD); (iv) monitoring the loss of the Ir<sup>I</sup>(1,5-COD)<sup>+</sup>-containing precursor versus time by GLC (of the hydrogenated COA formed, as shown in eq 1); and notably (v) collecting extensive kinetic studies by the CHCRR kinetic methodology with checking by GLC-monitored kinetics, as detailed in the Supporting Information and utilized herein, vide infra.

The significance of the minimum mechanisms in Scheme 2 is that they are the first of their kind, and also the first mechanistic alternatives to the unsupported<sup>64,65</sup> 1950 LaMer model<sup>66</sup> for particle formation postulating "instantaneous/ burst nucleation" and then "diffusion-controlled growth". The minimum mechanisms in Scheme 1 serve as the working mechanistic hypotheses going forward for further attempted disproof and the expected, normal refinement to more complex mechanisms as is the fate of all Ockham's razor obeying, deliberately initially minimalistic mechanisms (i.e., and once additional data or new methods become available); see the Section 2.6 in a recent review<sup>64</sup> for more on this and related points ("2.6. The Critical Difference between a Physical Chemical Model and a Physical Organic Chemistry-Type, Chemical Equation- and Disproof-Based, Reaction Mechanism"<sup>64</sup>). If one writes out the combinations of the PESteps in Scheme 1, a new three-step mechanism discovered by ME-PBM<sup>18,19</sup> (vide infra), and if one then also includes Karim's important ligand-based PEStep, 32,39 along with the established first, 52 second, 61 and third (termolecular) and "alternative termolecular" nucleation mechanisms, one now has five classes containing at least 96 individual mechanisms to try to account quantitatively for one's particle formation reactions. <sup>131</sup>

The simplest, discovered first, two-step mechanism<sup>52</sup> contained within Scheme 2 and explicitly given back in Scheme 1, namely that of A  $\rightarrow$  B (rate constant  $k_1$ ) and A + B  $\rightarrow$  2B (rate constant  $k_2$ ), is especially well-tested in a number of other particle formation and growth systems across nature, including homogeneous catalyst formation, 67-69 heterogeneous catalyst formation, <sup>70–73</sup> protein aggregation, <sup>74–76</sup> solidstate kinetics, 77,78 dye aggregation, 79 and other areas of nature showing "cooperative", autocatalytic phenomena. 80 The use to date of pretty much any and all applicable physical methods in those >560 citations of the 1997 paper<sup>52</sup> documents that the two-step mechanism is the best-tested, best-supported, and currently most accepted kinetic model for the initial treatment of particle formation kinetic data at the PEStep level for a broad variety of nucleation and growth systems across nature. 45-52,54-80 However, it is not yet clear which physical methods are both necessary and sufficient to yield a reliable particle formation mechanism? Additionally, not yet addressed are which physical methods in what combinations are needed to yield what level of precision and, notably, what accuracy in the resultant rate constants?

1.5. ME-PBM: Elucidation of a New, Three-Step Minimum Mechanism in the Original A = {(1,5-COD)-Ir<sup>1</sup>-POM}<sup>8-</sup> System. The minimum mechanisms in Scheme 2 were further tested in 18 2019 and 19 2020 via the development of ME-PBM. 18,19 The underlying basis of PBM 18-86 is not hard to understand: PBM is a method applicable to any system of countable entities, 18 where "a distribution of properties changes in time and perhaps also in space". 18 As described in our 2020 ME-PBM paper, "...for every particle in the dynamic particle distribution ("population") one is simply keeping track of the evolving particle population using the law of mass balance on each and every particle size, thereby, determining the PSD as a function of time, including the key final PSD." Hence, the accumulation of particles of any given size is equal to the input of particles to that size minus the output of particles from that size.

ME-PBM builds off of and expands classic PBM by using deliberately minimalistic, extensively disproof-based 15,16 mechanisms of particle formation and agglomeration (e.g., as back in Scheme 1) to guide the construction of the computer code of an also deliberately minimalistic, hence Ockham's razorobeying, (ME)-PBM. That code takes the minimum mechanisms contained within Scheme 2 or the new threestep mechanism, 18,19 one at a time, and uses each mechanism to develop a PBM code in MATLAB corresponding to, or more correctly limited by, 18,19 the minimum PEStep mechanism being used as the input and, thereby, being tested in that specific ME-PBM. The resulting computer code is then used (i) to attempt to fit experimental PSD data without any input assumptions about the underlying rate constant parameters or the PSD shape; and therefore (ii) to test the input minimum mechanism in its coded form. The key questions being addressed are (a) can the ME-PBM corresponding to a given, minimum mechanism fit the experimental PSD data? 18,19 and (b) which specific mechanism and the corresponding ME-PBM yield the best fit to the experimental PSD?

In our initial ME-PBM studies of the first-generation {(1,5-COD)Ir<sup>I</sup>·POM}<sup>8-</sup> system, 12 total possible mechanisms were considered constructed from the steps in Scheme 2 as well

as three different, experimentally established nucleation mechanisms,  $^{47,52,61,63}$  hence a range of 36 possible mechanisms were tested by ME-PBM. That work showed that obtaining a good fit to the PSD is by no means trivial. Instead, a good fit to the PSD and its shape is a stringent test of the input mechanism as well as the resultant code, requiring the input of both the correct nucleation mechanism and a correct PEStepbased ME-PBM code. However, once the ostensibly "correct" nucleation and growth mechanism was employed in an also error-free code, the resultant mechanism-enabled-PBM code was able (iii) to fit the PSD, and also (iv) serve as a check on the proposed mechanism, as well as somewhat amazingly (v) extract rate constants from that information-rich PSD. In addition, in the current ME-PBM and code, a cut-off parameter, M, is obtained that is used to define the "smaller", B, from the "larger", C, particles, <sup>18,19</sup> Scheme 2, vide supra. The ME-PBM-derived fit of the PSD, including the PSD shape, proved excellent, all with no prior input to the PSD shape. 18,19 Noteworthy here is that the ME-PBM-based excellent, quantitative accounting of the PSD results supports in at least a general way the CHCRR kinetic methodology 47,52-62 used to obtain those minimum mechanisms (i.e., back in Scheme 2) as well as the experimentally determined nucleation mechanisms used as the input 47,52,61 to the ME-PBM.

The resultant rate constants from the ME-PBM fitting of the PSD can then be used (vi) to predict a precursor A-loss kinetic curve for comparison to the experimental CHCRR curve, the right-most part of Figure 1. This illustrates a limit of our

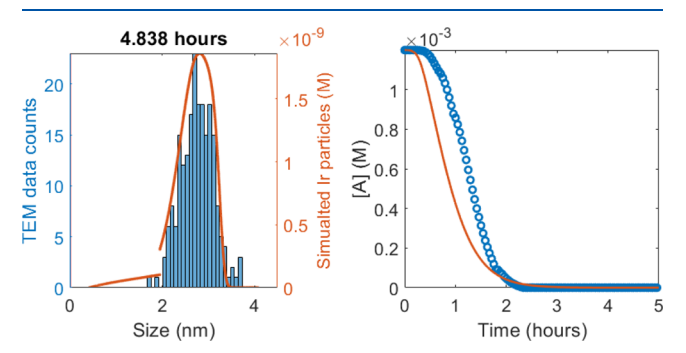


**Figure 1.** Fit of the final, 4.838 h histogram for formation of what are on-average  $Ir(0)_{\sim 730}$  nanoparticles in that particular study produced from  $\sim$ 730 equiv of  $\{(1,5\text{-COD})\text{Ir}^{\text{I}}\text{-POM}\}^{8^{-}}$ , under  $H_2$  in acetone solvent at 22 °C, to yield the final  $Ir(0)_{\sim 730}\cdot(\text{POM}^{9^{-}})_x$  nanoparticles. The resultant fit-determined rate constants (that refer to the detailed kinetics scheme and rate-constant nomenclature in a 2020 ME-PBM paper<sup>19</sup>) are  $k_{1\text{alt}}=6.55\times10^4\,\text{M}^{-2}\,\text{h}^{-1}$ ,  $k_2=1.65\times10^4\,\text{M}^{-1}\,\text{h}^{-1}$ , and  $k_3=5.63\times10^3\,\text{M}^{-1}\,\text{h}^{-1}$ , and B vs C particle-size cutoff, M=274. The fit to the PSD to the left including its shape is excellent, without any prior assumptions about the PSD shape. The computed curve shown to the right for the loss of the precursor  $A=\{(1,5\text{-COD})\text{Ir}^{\text{I}}\text{-POM}\}^{8^{-}}$  (i.e., using the rate constants from the fit to the PSD) has the proper sigmoidal shape, but undercuts the CHCRR kinetics curve by more than experimental error. Reproduced with permission from ref 19. Copyright 2020 American Chemical Society.

current knowledge as well as an impetus for the present synchrotron-based and ME-PBM studies: as shown in the right-most part of Figure 1, the predicted A-loss curve from the ME-PBM-derived rate constants (from the PSD analysis) versus the experimental CHCRR curves are both sigmoidal, but not identical. Hence, additional checking of the CHCRR kinetics by the more direct methods of X-ray absorption nearedge structure (XANES) and SAXS, plus a better under-

standing of any differences between the various kinetics monitoring methods, are two additional, subgoals of the present studies.

In a very important finding, the ME-PBM was also able to inform the "inverse problem" of what exact minimum mechanism is causing the observables by 18,19 providing a previously unconceived three-step mechanism. In that new, net three-step mechanism (that will be important in the present studies, vide infra), the A + B  $\rightarrow$  2B autocatalytic growth step of the two-step mechanism had to be expanded into two steps,  $A + B \rightarrow C$  (rate constant  $k_2$ ) and  $A + C \rightarrow 1.5C$  (rate constant  $k_3$ ), in order to account for the PSD. <sup>18,19</sup> The ME-PBM fit to the observed PSD revealed the seminal insight that  $k_2 > k_3$ , that is, the finding that "smaller particles grow faster than larger particles", <sup>18,19</sup> thereby catching up in size with the larger particles by the end of the reaction. <sup>18,19</sup> This "smaller grow faster than larger" insight in turn provides a paradigm shift in the understanding of how narrow PSDs can be formed: there is no need for (unphysical; experimentally unsupported<sup>64,65</sup>) "instantaneous/burst" nucleation as postulated in the 1950 LaMer model<sup>66</sup> for forming putatively "monodisperse" particles. Instead, near-monodisperse (by definition<sup>87</sup>  $\leq \pm 15\%$ ), PSDs can be formed despite the broadening effect of continuous nucleation<sup>52</sup> because the smaller particles grow faster than the larger ones, in the end catching up with them in size. 18,19 The interested reader is referred to two full papers for further details and additional insights and conclusions from the initial application of ME-PBM to the classic {(1,5-COD)Ir<sup>I</sup>· POM $^{8-1}$  precursor and resultant  $Ir(0)_n \cdot (POM^{9-1})_x$  system. <sup>18,19</sup> It is perhaps obvious why ME-PBM will be employed as part of the present work: it is now a required test 18,19 of any proposed particle formation mechanism(s). Can the proposed mechanism yield a ME-PBM able to account quantitatively for the PSD, including its shape? If not, then the proposed mechanism must be incorrect in one or more step(s).

1.6. Second-Generation,  $\{[(1,5\text{-COD})\text{Ir}^{\text{I}}\cdot\text{HPO}_4]_2\}^{2^-}$ , Iridium Nanoparticle System. As noted earlier, we began the development of a second-generation system back in 2003 involving  $\text{HPO}_4^{2^-}$  as a smaller, simpler nanoparticle stabilizer. Work since then, that serves as a foundation for the present studies, includes: the synthesis  $^{55,88}$  of the bimetallic nanoparticle precursor,  $\{[(1,5\text{-COD})\text{Ir}^{\text{I}}\cdot\text{HPO4}]_2\}^{2^-}$ , and the experimentally determined, balanced reaction stoichiometry under  $H_2$  for the formation of  $\text{HPO}_4^{2^-}$ -stabilized  $\{\text{Ir}(0)_n\cdot(\text{HPO}_4)_x\}^{-2x}$  nanoparticles in acetone solvent, eq  $7.^{55,88}$  Also

available are the characterization<sup>55</sup> of the resultant  $\{Ir(0)_n \cdot (HPO_4)_x\}^{-2x}$ , average  $n \sim 150$ , nanoparticles as well as the TEM-determined PSDs versus time<sup>63</sup> —PSDs begging for analysis by ME-PBM, vide infra.

Although the second-generation  $\{[(1,5\text{-}COD)\text{Ir}^{\text{I}}\cdot\text{HPO}_4]_2\}^{2-}$  nanoparticle precursor system provides seven advantages as summarized in the Supporting Information, including allowing us to use the direct monitoring methods of XANES and SAXS, one disadvantage of even this second-generation system in comparison to the classic  $P_2W_{15}\text{Nb}_3\text{O}_{62}^{9-}$  POM system merits mention upfront:  $\text{HPO}_4^{2-}$  is a somewhat less-effective stabilizer compared to the large, polyanionic POM<sup>9-</sup>. Hence, at least 2 molar equiv of  $\text{HPO}_4^{2-}$  are required to avoid the formation of bulk Ir(0) metal. PDA This in turn implies that some agglomeration of the resultant  $\text{Ir}(0)_n \cdot (\text{HPO}_4^{2-})_x$  particles is at least possible if not expected, so that the present studies should and will check for agglomeration via the kinetics, PSDs, SAXS, and ME-PBMs—in the latter separate ME-PBMs first without and then with bimolecular agglomeration, B + B  $\rightarrow$  C, as shown back in Scheme 2.

1.7. More Intimate Nucleation Mechanism for the  $\{[(1,5-COD)Ir^{l}\cdot HPO_{4}]_{2}\}^{2-}$  Precursor/Ir(0)<sub>n</sub>·(HPO<sub>4</sub><sup>2-</sup>)<sub>x</sub> Nanoparticle System Obtained via the CHCRR Methodology. Although CHCRR-monitored sigmoidal kinetics of formation of  $\{Ir(0)_n \cdot (HPO_4)_x\}^{-2x}$  nanoparticles from the A =  $\{[(1,5-1)^n]^{-2x}\}^{-2x}$ COD)Ir<sup>1</sup>·HPO<sub>4</sub>]<sub>2</sub> $\}^{2-}$  precursor are well-fit by the simple A  $\rightarrow$  B, then the A + B  $\rightarrow$  2B two-step mechanism,<sup>63</sup> the nearly constant [A] during the induction period hides higher-order, more complex nucleation mechanisms until and unless one goes looking for them with additional kinetics studies as we have done. 47,61,63 The needed studies uncovering one postulated, more intimate, molecular nucleation mechanism (as needed for the ME-PBM) have already been performed for the {[(1,5-COD)Ir<sup>I</sup>·HPO<sub>4</sub>]<sub>2</sub>}<sup>2-</sup> precursor system. Specifically, varying [A] and  $[HPO_4^{\ 2^-}]$  concentration studies allowed the identification<sup>63</sup> of a once-again<sup>47,61</sup> low-molecularity nucleation mechanism, one now first-order in the bimetallic {[(1,5-COD)Ir<sup>I</sup>·HPO<sub>4</sub>]<sub>2</sub>}<sup>2-</sup> precursor, but also involving a dissociative prior equilibrium,  $K_{\text{Diss}}$ , Scheme 3, but now dissociation of a  $\text{HPO}_4^{2-}$  dianion. That dissociative prior equilibrium could lead to a couple of possible, more reactive species, one of which is  $\{[(1,5\text{-COD})\text{Ir}^{\text{I}}]_2 \cdot \text{HPO}_4\}^0$ . Because  $\{[(1,5\text{-COD})^2]_2 \cdot \text{HPO}_4\}^0$ . Ir<sup>I</sup>]<sub>2</sub>·HPO<sub>4</sub>}<sup>0</sup> is neutral and hence less negatively charged than the dianionic precursor  $\{[(1,5-COD)Ir^{I}\cdot HPO_{4}]_{2}\}^{2}$ , because it has a more open structure,<sup>63</sup> and because NMR evidence supported the presence {[(1,5-COD)Ir<sup>I</sup>]<sub>2</sub>·HPO<sub>4</sub>}<sup>0</sup> in solution, 63 we previously postulated that this neutral species is a kinetically competent intermediate en route to facile reduction to Ir(0) by H<sub>2</sub>, Scheme 3, likely via precedented (Ir-H)<sub>m</sub> hydride intermediates. 47,63

Scheme 3. One Published More Intimate Nucleation Mechanism<sup>63</sup> Involving a Dissociative Equilibrium from  $\{[(COD)Ir^I \cdot HPO_4]_2\}^{2-}$  in Acetone, Based on the  $[HPO_4^{2-}]$  Dependence of the Kinetics and <sup>1</sup>H NMR Evidence for the Neutral,  $\{[(COD)Ir^I(solv)]_2 \cdot HPO_4\}^0$  Intermediate

$$\{ [(COD)|r^{I} \cdot HPO_{4}]_{2} \}^{2^{-}} + 2 \text{ solv}$$

$$\{ [(COD)|r^{I}(\text{solv})]_{2} \cdot HPO_{4} \}^{0} + HPO_{4}^{2^{-}}$$

$$\{ [(COD)|r^{I}(\text{solv})]_{2} \cdot HPO_{4} \}^{0} + HPO_{4}^{2^{-}}$$

$$+ 2 H^{+} + 2 \text{ solv}$$

$$(Eq 9)$$

The effects of common room dust on the nucleation, in the A = {[(1,5-COD)Ir<sup>I</sup>·HPO<sub>4</sub>]<sub>2</sub>}<sup>2-</sup> system<sup>63</sup> (and also before in the A = {(1,5-COD)Ir<sup>I</sup>·POM}<sup>8-</sup> system<sup>62</sup>), are available as part of our prior studies. It is also at least conceivable that HPO<sub>4</sub><sup>2-</sup> dissociation could occur alternatively as follows:  $\{[(1,5-COD)Ir^{I} HPO_{4}]_{2}\}^{2-} + 2 \text{ solvent } \Rightarrow HPO_{4}^{2-} + [(1,5-COD)Ir^{I} HPO_{4}]_{2}\}^{2-} + 2 \text{ solvent } \Rightarrow HPO_{4}^{2-} + [(1,5-COD)Ir^{I} HPO_{4}]_{2}\}^{2-} + 2 \text{ solvent } \Rightarrow HPO_{4}^{2-} + [(1,5-COD)Ir^{I} HPO_{4}]_{2}\}^{2-} + 2 \text{ solvent } \Rightarrow HPO_{4}^{2-} + [(1,5-COD)Ir^{I} HPO_{4}]_{2}\}^{2-} + 2 \text{ solvent } \Rightarrow HPO_{4}^{2-} + [(1,5-COD)Ir^{I} HPO_{4}]_{2})^{2-} + 2 \text{ solvent } \Rightarrow HPO_{4}^{2-} + [(1,5-COD)Ir^{I} HPO_{4}]_{2})^{2-} + 2 \text{ solvent } \Rightarrow HPO_{4}^{2-} + [(1,5-COD)Ir^{I} HPO_{4}]_{2})^{2-} + 2 \text{ solvent } \Rightarrow HPO_{4}^{2-} + [(1,5-COD)Ir^{I} HPO_{4}]_{2})^{2-} + 2 \text{ solvent } \Rightarrow HPO_{4}^{2-} + [(1,5-COD)Ir^{I} HPO_{4}]_{2})^{2-} + 2 \text{ solvent } \Rightarrow HPO_{4}^{2-} + [(1,5-COD)Ir^{I} HPO_{4}]_{2})^{2-} + 2 \text{ solvent } \Rightarrow HPO_{4}^{2-} + [(1,5-COD)Ir^{I} HPO_{4}]_{2})^{2-} + 2 \text{ solvent } \Rightarrow HPO_{4}^{2-} + [(1,5-COD)Ir^{I} HPO_{4}]_{2})^{2-} + 2 \text{ solvent } \Rightarrow HPO_{4}^{2-} + [(1,5-COD)Ir^{I} HPO_{4}]_{2})^{2-} + 2 \text{ solvent } \Rightarrow HPO_{4}^{2-} + [(1,5-COD)Ir^{I} HPO_{4}]_{2})^{2-} + 2 \text{ solvent } \Rightarrow HPO_{4}^{2-} + [(1,5-COD)Ir^{I} HPO_{4}]_{2})^{2-} + 2 \text{ solvent } \Rightarrow HPO_{4}^{2-} + [(1,5-COD)Ir^{I} HPO_{4}]_{2})^{2-} + 2 \text{ solvent } \Rightarrow HPO_{4}^{2-} + [(1,5-COD)Ir^{I} HPO_{4}]_{2})^{2-} + 2 \text{ solvent } \Rightarrow HPO_{4}^{2-} + [(1,5-COD)Ir^{I} HPO_{4}]_{2})^{2-} + 2 \text{ solvent } \Rightarrow HPO_{4}^{2-} + [(1,5-COD)Ir^{I} HPO_{4}]_{2})^{2-} + 2 \text{ solvent } \Rightarrow HPO_{4}^{2-} + [(1,5-COD)Ir^{I} HPO_{4}]_{2})^{2-} + 2 \text{ solvent } \Rightarrow HPO_{4}^{2-} + [(1,5-COD)Ir^{I} HPO_{4}]_{2})^{2-} + 2 \text{ solvent } \Rightarrow HPO_{4}^{2-} + [(1,5-COD)Ir^{I} HPO_{4}]_{2})^{2-} + 2 \text{ solvent } \Rightarrow HPO_{4}^{2-} + [(1,5-COD)Ir^{I} HPO_{4}]_{2})^{2-} + 2 \text{ solvent } \Rightarrow HPO_{4}^{2-} + [(1,5-COD)Ir^{I} HPO_{4}]_{2})^{2-} + 2 \text{ solvent } \Rightarrow HPO_{4}^{2-} + [(1,5-COD)Ir^{I} HPO_{4}]_{2})^{2-} + 2 \text{ solvent } \Rightarrow HPO_{4}^{2-} + [(1,5-COD)Ir^{I} HPO_{4}]_{2})^{2-} + 2 \text{ solvent } \Rightarrow HPO_{4}^{2-} + [(1,5-COD)Ir^{I} HPO_{4}]_{2}$  $COD)Ir^{I} \cdot HPO_{4}^{-} + (1.5 \cdot COD)Ir^{I}(solv)_{2}^{+}$ , with the cationic solvate being the (precedented) reactive intermediate.<sup>47</sup> Regardless of which nucleation mechanism is operative (a point we can probe via ME-PBM), such detailed, approaching molecular-level knowledge of a nucleation mechanism, including the quantitative effects of the common impurity of dust, is rare. 47,61 Noteworthy here is that measuring precise much less accurate nucleation kinetics and associated rate constants is notoriously difficult to even  $\pm 10^1$ . Hence, ideally doing better than  $\pm 10^1$ , while using multiple, complimentary physical methods, is another, state-of-the-art goal of the present contribution.

- 1.8. Specific Questions Addressed in the Present Study. With the required background now in hand, we can summarize the focus of the present study by listing the seven specific questions addressed herein:
  - (1) Will XANES and SAXS obtained kinetics data for the  $\{[(1,5-COD)Ir^{I}\cdot HPO_{4}]_{2}\}^{2-}$  precursor/ $Ir(0)_{n}$ . (HPO<sub>4</sub><sup>2-</sup>)<sub>r</sub>, nanoparticle system both be (i) sigmoidal as expected, and (ii) well-fit by the two-step mechanism as is found for the CHCRR and GLC-derived kinetics data?
  - (2) What level of at least semiquantitative agreement is there between the rate constants obtained by CHCRR, GLC, XANES, and SAXS monitoring methods? What is the implied level of precision and, ideally, accuracy of the resultant rate constants?
  - (3) When looking in more detail at the now well-established, prototype  $Ir^1(1,5-COD)^+$ -containing precursor systems,  $^{45-47,51,52,54-63,87-93}$  what are the known, primary sources of experimental error in measuring accurate nucleation and growth rate constants? What more generally are the error bars on the nucleation and growth rate constants and how do those error bars compare to the most precise nucleation and growth kinetics in the literature? 94,95
  - (4) Are synchrotron-based methods alone, specifically XANES and SAXS, sufficient for the present example to obtain the ostensibly "correct" mechanism according to all the available data? An underlying, broader question—one only fully addressable by the communities involved—is if synchrotron XANES and SAXS direct methods are pretty much fool-proof, or do these generally powerful methods also have limitations that merit additional investigation?
  - (5) Does the application of ME-PBM to the TEMdetermined PSDs support or refute the best fitting mechanism? Is our recent conclusion, that ME-PBM is likely to become a "must use" tool 18,19 prior to publishing any particle formation mechanism, supported or refuted?
  - (6) What, then, is (are) deemed to be "best" physical method(s) for monitoring especially the notoriously hard to measure nucleation step(s)<sup>61</sup> and to obtain accurate rate constants, at least for the present  $Ir(0)_n$ .  $(HPO_4^{2-})_x$  nanoparticle system? What are the strengths

- and weaknesses of each method in at least our hands, and how can they be used in a complimentary fashion? What roles do indirect, but in-house and hence convenient, methods such as the CHCRR have in comparison to the XANES and SAXS monitoring methods?
- (7) Finally, what additional studies are recommended going forward en route toward an even more detailed understanding of particle formation nucleation, growth, and agglomeration across nature?

### 2. EXPERIMENTAL SECTION

- 2.1. Materials. All solvents and compounds used were stored in a Vacuum Atmospheres' inert (N2) atmosphere drybox (<1.0 ppm O<sub>2</sub>, as monitored by a Vacuum Atmospheres' continuous O2-level monitor) prior to use unless otherwise indicated. The following were brought into the drybox as received: [(1,5-COD)Ir<sup>I</sup>Cl]<sub>2</sub> (STREM, 99%), (Bu<sub>4</sub>N)H<sub>2</sub>PO<sub>4</sub> (Aldrich, powder), proton-sponge (Aldrich, 99%), AgBF<sub>4</sub> (Aldrich, white powder), decane (Sigma-Aldrich), and diethyl ether [Aldrich, anhydrous, high-performance liquid chromatography (HPLC) grade]. Outside of the drybox, acetone (Aldrich, for HPLC, 99%) was sparged with argon for ≥10 min, then immediately sealed and transferred into the drybox. Cyclohexene was distilled over Na metal and benzophenone under argon, and then stored in the drybox. Ethyl acetate (Aldrich  $\geq$ 99.8%, <0.05%  $H_2O$ ), acetonitrile (Aldrich, 99.8%, anhydrous, H<sub>2</sub>O content <0.001%), benzene (Aldrich, anhydrous, 99.8%, stored under an inert atmosphere), 2-butanone (Aldrich, ≥99.0 purity), and dichloromethane (HPLC grade, stored over 4 Å molecular sieves) were degassed as needed prior to storage and use in the drybox. Outside of the drybox, Bu<sub>4</sub>N<sup>+</sup>OH<sup>-</sup> (Aldrich, 40% by mass in H<sub>2</sub>O) was stored between 8 and 10 °C in the refrigerator. Deuterated solvents were purchased from Cambridge Isotope Laboratories: chloroform- $d_1$  (99.8%), acetonitrile- $d_3$  (99.8%), and acetone- $d_6$  (99.5%). Argon (>99.9% purity) and H<sub>2</sub> (>99.5% purity) were purchased from Airgas. H<sub>2</sub> has was passed through O2- and H2O-scavenging traps (Trigon Technologies) prior to use. Silicon nitride grids (20 nm window thickness) for transmission electron microscopy (TEM) were purchased from TEM Windows and used as received.
- 2.2. Analytical Procedures. Unless otherwise stated, all synthetic works and reaction solution preparations were conducted in an oxygen- and moisture-free Vacuum Atmospheres' nitrogen drybox environment (<1 ppm O<sub>2</sub>, as monitored by a Vacuum Atmospheres' continuous O2-level monitor). All air-sensitive samples were stored double bottled inside the drybox. All glassware were dried at  $\sim$ 160  $^{\circ}$ C for 48 h to remove residual moisture before being transferred immediately into the drybox antechamber, where they cooled under the vacuum of the antechamber and then inside the drybox. CHCRR experiments were conducted using an inhouse, custom hydrogenation setup as detailed in section 2.5, vide infra. GLC was conducted using a Hewlett-Packard 5890 series II GC with a flame ionization detector equipped with a 30 m (0.25 mm i.d., 25  $\mu$ m film) Dowex DB-1 column and coupled to a Hewlett-Packard 3395 integrator. TEM experiments were examined with a JEOL JEM2100F transmission electron microscope using silicon nitride grids. The microscope had an ultrahigh resolution lens pole piece that provides

0.135 nm Scanning TEM resolution. For STEM imaging, a JEOL annular dark field detector was used. NMR ( $^{1}$ H,  $^{13}$ C, and  $^{31}$ P) spectra were collected on either a Varian Inova 400 MHz or a Bruker NEO 400 MHz spectrometer at 25  $^{\circ}$ C. Synchrotron XAFS experiments were performed at the Stanford Synchrotron Radiation Lightsource (SSRL) at beamline 2-2. Synchrotron SAXS patterns were collected at the Australian Synchrotron at the SAXS/WAXS beamline.

2.3. Preparation of the Iridium Solvate Precursor Complex, [(1,5-C<sub>8</sub>H<sub>12</sub>)Ir<sup>I</sup>(NCCH<sub>3</sub>)<sub>2</sub>][BF<sub>4</sub>], and the Stabilizer,  $(Bu_4N)_2HPO_4$ . The synthesis of  $[(1,5-C_8H_{12})-$ Ir<sup>I</sup>(NCCH<sub>3</sub>)<sub>2</sub>][BF<sub>4</sub>] was prepared on the basis of literature methods with small modifications. 55,96 The preparation and characterization details are summarized in the Experimental Section of ref 63. Below is an abridged summary from a comprehensive report available to the interested reader. 63 In a N<sub>2</sub>-atmosphere drybox, 3.00 mmol of [(1,5-COD)Ir<sup>I</sup>Cl]<sub>2</sub> was dissolved in 43 mL of CH<sub>2</sub>Cl<sub>2</sub>. After 5 min of stirring, 10 mL of CH<sub>3</sub>CN was added to the solution. The solution was stirred for 10 min and turned yellow, and 6.04 mmol of AgBF<sub>4</sub> was added to the solution. A white-gray precipitate of AgCl appeared immediately and the solution was stirred for 5 min before it was vacuum-filtered through a Whatman #2 paper. The yellow filtrate was slowly poured into ~200 mL of diethyl ether. Precipitation of fine yellow crystals of [(1,5-C<sub>8</sub>H<sub>12</sub>)- $Ir^{I}(NCCH_{3})_{2}[BF_{4}]$  occurred instantaneously, and the crystals were collected under vacuum using a 30 mL glass frit. The crystals were transferred and dried in a 20 mL vial under vacuum for 9 h. The synthesis resulted in an 80% yield and exhibited <sup>1</sup>H NMR peaks that matched the literature spectral data<sup>96</sup> provided in ref 63.

Details regarding the preparation of  $(Bu_4N)_2HPO_4$  from (Bu<sub>4</sub>N)H<sub>2</sub>PO<sub>4</sub> and Bu<sub>4</sub>N<sup>+</sup>OH<sup>-</sup> in CH<sub>3</sub>CN are provided in prior publications; 55,63 specifically the Supporting Information of ref 63 contains a series of important control experiments regarding the purity and identity of the trace impurity,  $(Bu_4N)_{4-x}(H_xP_2O_7)$ , from the preparation of  $(Bu_4N)_2HPO_4$ . Briefly, equal molar amounts of (Bu<sub>4</sub>N)H<sub>2</sub>PO<sub>4</sub> and Bu<sub>4</sub>N<sup>+</sup>OH<sup>-</sup> (0.75 mmol and 0.50 mL, respectively) were combined in 4 mL of CH<sub>3</sub>CN, stirred for 4.0 h, and placed under vacuum (~125 mmHg) at ~30 °C (temperature of the drybox environment) to remove CH<sub>3</sub>CN and H<sub>2</sub>O. Total drying time was  $\sim$ 24 h. The purity was  $\geq$ 92–97%, as determined by ¹H and ³¹P NMR. A ≤3-8% impurity of (Bu<sub>4</sub>N)<sub>4-x</sub>(H<sub>x</sub>P<sub>2</sub>O<sub>7</sub>) resulted from the well-precedented dehydration reaction  $^{97-100}$  that occurs as a function of the drying time the solution spends under vacuum. Three control experiments available in ref 63 demonstrate that the impurity does not affect the reaction kinetics within experimental error. 63 Specifically, (i) increasing the length of drying time resulted in a maximum 10% (Bu<sub>4</sub>N)<sub>4-x</sub>(H<sub>x</sub>P<sub>2</sub>O<sub>7</sub>) impurity, which did not change the  $k_1$  rate constant from when 3-8% impurity was present. Additionally, (ii) deprotonation of the commercially available (Bu<sub>3</sub>NH)<sub>2</sub>(H<sub>2</sub>P<sub>2</sub>O<sub>7</sub>) to  $(Bu_3NH)_{4y+3y}(P_2O_7)_y(HP_2O_7)_x$  was then added to the reaction mixture at 0.1, 0.2, 0.5, and 1.0 molar equiv, 63 but did not change the observed kinetics until  $\geq 0.2$  molar equiv ( $\geq 20\%$ ) were added. Finally, (iii) the kinetics with 0.00, 0.10, 0.25, 0.35, 0.50, and 2.00 molar equiv of the commercially available diprotonated salt, (Bu<sub>3</sub>NH)<sub>2</sub>(H<sub>2</sub>P<sub>2</sub>O<sub>7</sub>), were measured, and once again the kinetics only changed when ≥0.25 molar equiv  $(\geq 25\%)$  were added.<sup>63</sup> Hence, at the levels (3-8%) of  $(Bu_4N)_{4-x}(H_xP_2O_7)$  present in the reaction, no observable

effects on the reaction or the kinetics are seen within experimental error as detailed in the Supporting Information elsewhere. <sup>63</sup>

2.4. Tandem In Situ XAFS Spectroscopy and CHCRR to Monitor Iridium Nanoparticle Formation. X-ray absorption fine structure (XAFS) experiments were performed at the Stanford Synchrotron Radiation Lightsource (SSRL) at Beamline 2-2. A double-crystal Si(220) monochromator was used to collect Ir L<sub>3</sub>-edge (11,215 eV) data in transmission mode with a scan duration of 4 min. Reference Ir foil was used for energy calibration. Raw XAFS data files were processed and analyzed in Athena, within the IFEFFIT software package, 1 all in accordance with literature standards in the field of XAFS spectroscopy. Quantitative analysis of Ir L3-edge XANES was performed by doing a linear combination fit of the change from 11,172.5-11,312.5 eV with standards as the first and last scans to yield weights of the initial and final phases. 102,103 Experiments were run in a Fischer-Porter (F-P) pressure bottle modified with two windows cut into the borosilicate, each covered with 0.127 mm Kapton film. Culture tube inserts were likewise cut and covered with a 0.0254 mm Kapton film. Samples were prepared as detailed in the next section. Concomitantly, hydrogen pressure kinetics were recorded via the Omega pressure transducer. Specifically, reaction solutions were prepared at 5.0 mM  $[(1,5-COD)Ir^{I}(NCCH_3)_2][BF_4]$ (20.0  $\mu$ mol in Ir), 5.0 mM proton-sponge (20.0  $\mu$ mol), and three different HPO<sub>4</sub><sup>2-</sup> loadings: 1.8, 2.25, and 2.7 molar equiv per mole of Ir (36.0, 45.0, and 54.0  $\mu$ mol in HPO<sub>4</sub><sup>2-</sup>, respectively). Reaction solutions were prepared in 3.33 mL of acetone and 0.67 mL cyclohexene for a total solution volume of 4.0 mL. The F-P pressure bottle was initially pressurized with  $\sim$ 55 psig H<sub>2</sub> gas.

Extended XAFS (EXAFS) data were collected on the  $Ir(0)_n$  product. Figure S1 of the Supporting Information coplots the Ir(0) black standard along with the  $Ir(0)_n$  nanoparticle products from each XAFS experiment that all resemble closely the spectrum of Ir(0) black. Because somewhat accelerated nucleation and growth is observed in our XAFS (XANES) studies (and fouling on the cell windows in our SAXS studies), vide infra, precedented X-ray-induced radiolysis in XAFS  $^{104-108}$  and SAXS  $^{109-112}$  will be a topic examined in the Results and Discussion sections. Relevant here is that recent work  $^{104}$  from one of us shows that a photon flux of  $\sim$ 3 ×  $10^{13}$  photons per second results in an estimated  $\sim$ 10 solvated electrons  $^{104}$  even when that radiolysis involves the otherwise highly endoergic process of removing an electron from  $Zn^{2+}$ ,  $Zn^{2+} + h\nu \rightarrow Zn^{3+} + e^-$ .

2.5. Standard Conditions for Ir(0), Nanoparticle Formation Kinetics Experiments with Concomitant Cyclohexene Hydrogenation Serving as the Reporter Reaction. Precatalyst solution of 6.0 mM Ir and ~4 molar equiv HPO<sub>4</sub><sup>2-</sup> was prepared in a drybox by dissolving 8.4 mg  $[(1,5-COD)Ir^{I}(NCCH_{3})_{2}][BF_{4}]$ , 42.1 mg  $(Bu_{4}N)_{2}HPO_{4}$ , and 3.9 mg proton-sponge, (1,8-bis(dimethylamino)naphthalene), in 2.5 mL acetone. The 2.5 mL precatalyst solution plus 0.5 mL of cyclohexene were transferred, while still in the drybox, to a new, 22 × 175 mm<sup>2</sup> Pyrex culture tube containing a new Teflon-coated  $5/16 \times 5/8$  in.<sup>2</sup> stir bar via a disposable polyethylene pipet. All nonsynchrotron nanoparticle formation and hydrogenation reactions were carried out using a custombuilt pressurized hydrogenation apparatus using a F-P pressure bottle.<sup>52</sup> Nanoparticle formation was monitored indirectly but in real time by the well-precedented

CHCRR<sup>52,57,89-91</sup> shown in Scheme 1. The culture tube with the precatalyst solution was placed in a F-P bottle modified with Swagelok poly(tetrafluoroethylene)-sealed quick-connects, sealed, transferred out of the drybox, and attached with the quick-connects of the hydrogenation line and its computer-interfaced Omega PX621 pressure transducer. Prior to attachment, the hydrogenation line was kept under vacuum. After attachment, the hydrogenation line was filled with ~55 psig H<sub>2</sub> gas for experiments under SAXS conditions and ~40 psig H<sub>2</sub> gas for experiments under SAXS conditions. The F-P bottle was immersed in a 500 mL water-jacketed reaction flask held at 22 °C by a thermostatic recirculating temperaturecontrol bath (VWR) filled with dimethyl silicon fluid (Thomas Scientific). A total of 14 quick purges with H<sub>2</sub> gas were performed over 3.5 min (1 every 15 s). 52,60,89,90 Following the 14th purge, the F-P bottle was pressurized to ~40 psig H<sub>2</sub> over 30 s before vigorous stirring ( $\sim$ 900 rpm; to avoid  $H_2$  gasto-solution mass transfer limitations<sup>113</sup>) was initiated and pressure uptake data were collected every minute using LabView 8.2 (all as before). 52,63 As before, a required correction 54,63 for the initial vapor pressure of acetone and cyclohexene was applied to the data, a correction detailed in the next section. The H2-loss data were converted to equivalent cyclohexene-loss data using the experimentally established, 1:1 H<sub>2</sub>:cyclohexene reaction stoichiometry. 52,6

$$\begin{split} n & [(1,5\text{-COD})\text{Ir}^{l}(\text{NCCH}_{3})_{2}][\text{BF}_{4}] \ + \ n \ (\text{Bu}_{4}\text{N})_{2}\text{HPO}_{4} + n \ \text{PS}^{\text{TM}} \quad & \frac{2.5 \ \text{H}_{2}}{\text{Acetone}} \\ & & \text{Ir}(0)_{n} \cdot (\text{HPO}_{4}^{2-})_{x} \ + \ (n - x) \ \text{HPO}_{4}^{2-} \ + \ n \\ & & + n \ \text{Bu}_{4}\text{N}^{+} \cdot n \ \text{PS}^{\text{TM}} - \text{H}^{+} + 2n \ \text{CH}_{3}\text{CN} \end{split}$$

2.6. Temperature Re-equilibration and Acetone Solvent Plus Cyclohexene Vapor-Pressure Correction. Experimentally, after the H<sub>2</sub> pressure flushes, unavoidable cooling by some evaporation, and then pressurization of the F-P bottle to an initial ~40 psig as detailed in section 2.5 just above, the measured pressure increases initially<sup>54</sup> by ca. 3 psig before showing a sigmoidal H2-loss curve, see Figure S2 of the Supporting Information. Hence, the usual<sup>54</sup> correction for this pressure increase due to rewarming of the F-P bottle and solution and any acetone solvent and cyclohexene vaporpressure additions was made by running the precedented control<sup>54</sup> experiment of combining 2.5 mL of acetone and 0.5 mL of cyclohexene in a new 22 × 175 mm<sup>2</sup> Pyrex culture tube containing a new Teflon-coated  $5/16 \times 5/8$  in.<sup>2</sup> stir bar, placing the culture tube in the F-P bottle, connecting the F-P-bottle to the hydrogenation line, and starting the experiment by the same series of H2 flushes and then repressurizing to an initial ~40 psig as already described. Triplicate experiments were run to determine the difference between the F-P bottle filled with only H2 gas and with the solvent mixture, as seen in Figure S2. Then, a point-by-point subtraction/correction for the observed pressure increase was applied to the experimental CHCRR H2-loss data, resulting in the final data for that kinetics run, Figure S3 as an example. This 19 year-old procedure<sup>54</sup> is, however, re-emphasized here because one of the questions addressed by the present work is the precision and accuracy of the nucleation and growth rate constants. The above necessary treatment of the H2-loss data changes the ±0.05 psig precision-based error in Figure S2 as a typical example, ca.  $43.00(\pm 0.05) - 27.00 (\pm 0.05)$  psig = 16.00  $(\pm 0.07)$  psig, to  $\pm 0.07/16 = 0.43\%$ , a negligible source of error compared to the other sources of experimental error (e.g., as will be discussed in the Results and Discussion sections).

**2.7. Kinetic Data Analysis Using COPASI Numerical Integration.** The resultant data from the CHCRR, as well as that from GLC, XANES, or SAXS monitoring (vide infra), were processed using Microsoft Excel, Origin 7, and COPASI. Specifically and using the integrated rate equation for the two-step mechanism, eq 11, rate constants ( $k_{\text{lobs}}$  and  $k_{\text{2obs}}$ ) were extracted by fitting the cyclohexene consumption data. Origin 7 was used to perform the nonlinear least-squares fitting.

$$[A]_{t} = \frac{\frac{k_{1\text{obs}}}{k_{2\text{obs}}} + [A]_{0}}{1 + \frac{k_{1\text{obs}}}{k_{2\text{obs}}[A]_{0}} \times \exp[(k_{1\text{obs}} + k_{2\text{obs}}[A]_{0})t]}$$
(11)

As before, only the first half of the cyclohexene consumption data was fit to ensure that the assumptions underlying the CHCRR, notably a zero-order excess of cyclohexene, remain valid.  $^{52}$  The curve-fit values of  $k_{2\text{obs}}$  were corrected by the ratio of [cyclohexene]/[Ir] as the mathematics of the CHCRR require (see elsewhere  $^{52}$  for details).

2.8. Time-Resolved GLC of the COA Product: Quantification and Kinetics. The procedure employed is identical to our previous publication on the {[(1,5-COD)Ir<sup>I</sup>· HPO<sub>4</sub>]<sub>2</sub>}<sup>2-</sup> system.<sup>63</sup> Specifically, samples were prepared as detailed in section 2.5 above and given on p 2852 in ref 63. At specific, predetermined times during the hydrogenation, the stirring was stopped, the  $H_2$  pressure was reduced to ~10 psig  $H_2$ , and the F-P bottle was returned to the drybox. Inside the drybox, the reaction solution was transferred to a 1 dram vial, where 3  $\mu$ L of decane were added as an internal standard for the GLC. Approximately 0.5 mL of the reaction solution with the decane (internal standard) was transferred to a different, clean 1 dram vial, removed from the drybox, and used for GLC analysis. A 2  $\mu$ L sample was injected into the chromatograph. The amount of COA was determined by analyzing the relative peak area of COA versus the relative peak area of the decane. A calibration curve of the known amounts of authentic COA and decane was obtained and then used to determine the equivalents of COA evolved versus the total initial iridium in the sample. The equivalents of COA were divided by the equivalents of initial iridium, and then multiplied by the initial  $[Ir]_0$  concentration to yield  $[COA]_t$  values plotted as a function of time. The data were then fit using the analytic equation for the two-step mechanism of slow, continuous nucleation, and autocatalytic surface growth, eq 11.

2.9. In Situ SAXS and Tandem CHCRR Monitoring of Ir(0)<sub>n</sub> Nanoparticle Formation. SAXS was conducted at the Australian Synchrotron at the SAXS/WAXS beamline. Data were collected using a Pilatus-1M detector with a samplecamera length of 0.6 m, a collecting photon energy of 18 keV, and an integration time of 5 s. A custom-built reaction cell was built to allow for SAXS as well as for tandem CHCRR H2pressure-loss monitoring of the  $Ir(0)_n$  nanoparticle formation reaction; an image of the cell is provided in Figure S3, Supporting Information. The custom-built reaction cell has modular gas fittings, and it also uses the same quick-connect fittings as the F-P bottle to interface the H<sub>2</sub> line and pressure transducer. The beamline's peristaltic pump system was similarly assembled from Hamilton modular components with syringe pump operations programmed into beamline control. Concomitantly, hydrogen pressure kinetics were recorded via the Omega pressure transducer. Reaction solutions were prepared in an inert atmosphere drybox with

an  $O_2$ -level  $\leq 5.0$  ppm. Each sample consisted of the following: 54.0  $\mu$ mol [(1,5-COD)Ir<sup>I</sup>(NCCH<sub>3</sub>)<sub>2</sub>][BF<sub>4</sub>], 216  $\mu$ mol (Bu<sub>4</sub>N)<sub>2</sub>HPO<sub>4</sub>, 54.0 μmol proton-sponge, 5 mL acetone, and 1 mL cyclohexene. The reaction solution (at 9.0 mM Ir and 3.6 molar equiv HPO<sub>4</sub><sup>2-</sup> per mol Ir) was transferred into the cell, sealed, taken out of the drybox, and placed in the beam path. Every 76 s, 1 mL of solution as drawn by the peristaltic pump system up to a 1 mm quartz capillary before being returned to the continuously stirred solution. Background measurements were collected to subtract the scattering of both the capillary and solvent, as they were observed to contribute significantly at early reaction times. Despite the background subtraction.  $Ir(0)_n$  particle scattering was convoluted with the solvent scattering at less than 1.0 h and for small particle sizes so that useable data resulted only after the first ca. 1 h, as detailed in the Results section covering the SAXS experiments.

**2.10. SAXS Data Processing and Analysis.** The SAXS data processing and analysis were done in accordance with literature standards in the field of small-angle scattering. The SAXS data analysis equation 115,116 employed is given in eq 12, where I(q) is the scattering intensity, N is the total number of particles,  $\Delta \rho$  is the electron density contrast between the scattering object and the surround matrix, n(r) is the size distribution, V(r) is the volume of an individual particle, f(qr) is the form factor describing the particle shape, and S(qr) is the structure factor describing the particle—particle interactions.

$$I(q) = N(\Delta \rho)^2 \int n(r)V(r)^2 f(qr)^2 S(qr) dr$$
(12)

To obtain the size distribution as a function of time, several standard assumptions were made. First, due to the low concentration of the sample, particle—particle interactions are assumed to be negligible, so that S(qr) = 1. Next, a spherical form factor is assumed. The form is represented as

$$f(qr) = \frac{3[\sin(qr) - qr\cos(qr)]}{(qr)^3}$$
(13)

and the volume as  $V(r) = (4/3)\pi r^3$ . Due to the raw SAXS data not being on an absolute scale, the constant prefactor,  $N(\Delta \rho)^2$ , becomes meaningless, other than as a factor that is proportional to the number of particles. Next, three distribution functions were compared: log—normal, Gaussian, and Schulz, which are represented, respectively, as eqs 14–16.

$$n(r) = \frac{\exp\left(-\frac{1}{2\sigma^2}\left(\ln\left(\frac{r}{r_0}\right)\right)^2\right)}{\sqrt{2\pi} \times r\sigma}$$
(14)

$$n(r) = \frac{\exp\left(-\frac{(r-r_0)^2}{2w^2}\right)}{\sqrt{2\pi} \times w}$$
(15)

$$n(r) = Z^{Z}X^{Z-1} \frac{\exp(-XZ)}{r_{0}\Gamma(Z)}$$
(16)

where  $w = \sigma r_0$ ,  $Z = \frac{1}{\sigma^2}$ , and  $X = \frac{r_0}{r}$ , and  $\Gamma(x)$  is the gamma function. Fitting with each distribution function yielded little difference, as shown in Figure S4, Supporting Information, where the mode of the distributions lies at a radius of approximately 7.5 Å. Ultimately, the Gaussian distribution function was used in the fittings for this report.

Intensity (arb. units) versus q (Å<sup>-1</sup>) data were processed using the Irena software package. Initial attempts to use the full q-range, with the second form factor oscillation, gave rise to an erroneous peak at small particles size. Hence, the q-range fit was limited to the primary form factor feature. The experimental data were fit from the latest times to the earliest times. At 1.5 h and earlier, the dispersion parameter ( $\sigma$ ) was fixed at 0.3 (once the intensity of the second form factor feature dropped below 10% of the initial scan). Data before 0.72 h were not fit because the total intensity was less than 10% of the initial scan. Overall, the total volume and pressure transducer signal were collected as a function of time.

Solvent background control scans before and after the reaction revealed some fouling of the cell window due to apparent  $Ir(0)_n$  formation, the possible origins of which will be discussed in the Results and Discussion sections (including the possibility of X-ray induced radiolysis  $^{109-112}$ ).

2.11. Time-Resolved TEM Sampling, Grid Preparation, and Particle Size Determination. The procedure employed is identical to that used in our previous publication on the  $\{[(1,5\text{-COD})\text{Ir}^{\text{I}}\cdot\text{HPO}_4]_2\}^{2-}$  system.<sup>63</sup> Specifically, samples were prepared as detailed back in section 2.5. All precatalyst solutions for TEM were prepared under XAFS conditions of 5.0 mM  $[(1,5-COD)Ir^{I}(NCCH_3)_2][BF_4]$  (20  $\mu$ mol Ir), 2.25 molar equiv (Bu<sub>4</sub>N)<sub>2</sub>HPO<sub>4</sub> (45  $\mu$ mol), and 5.0 mM proton-sponge (20 µmol), 3.33 mL acetone, and 0.67 mL cyclohexene. The initial hydrogen pressure employed was 55 psig. At five specific, predetermined times during the hydrogenation (0.75, 1.5, 3.25, 5.0, and 10.0 h), the stirring was stopped, the  $H_2$  pressure was reduced to  $\sim 10$  psig  $H_2$ , and the F-P bottle was returned to the drybox. In the drybox, the remaining H<sub>2</sub> was released from the F-P bottle and the solution was transferred into a new and clean 20 mL scintillation vial. A small, ~0.5 mL aliquot of the solution was transferred to a new 20 mL scintillation vial and was approximately diluted 20-fold by 2-butanone. The use of 2butanone and the ~1:20 dilution mitigates against aggregation of the nanoparticles on the grids (a valuable experimental "trick" discovered previously via considering experimental effort<sup>63</sup>) for minimizing particle aggregation due to preparation of the TEM grids. Silicon nitride grids were used and prepared by placing a 1.0  $\mu$ L aliquot of the 1:20 solution on the grid via a micropipet and allowing excess liquid to evaporate. The grids were fully dried in the drybox environment at ~30 °C for a minimum of 12 h prior to being analyzed by TEM.

Micrographs of dark-field scanning TEM (STEM) were collected at three or more locations on the TEM grid to ensure each given micrograph was representative of the entire sample. For each sample,  $\geq$ 350 particles were measured for their size. Measuring 200 particles, at a minimum, is necessary for obtaining a reproducible and statistically relevant average size. Across the five samples, 3054 particles were measured. The open-source software ImageJ, a National Institutes of Health sponsored image processing platform (http://rsbweb.nih.gov/ij/), was used to measure particle sizes, as previously detailed. 117

Particle size distributions (PSDs) were prepared by binning the measured particles into 0.2-nm-wide bins. For example, particles between 1.20 nm and 1.39 nm were assembled into the 1.3-nm bin. A 0.2-nm-wide bin was chosen over a 0.1-nm bin because the resolution of the microscope for STEM measurements is 0.135 nm as previously mentioned.

**2.12. Mechanism-Enabled Population Balance Modeling.** ME-PBM was accomplished using a system of ordinary differential equations (ODEs) based on the experimental mechanism as detailed in refs 18 and 19. Briefly, ODEs were derived for each PEStep in the mechanism and solved using MATLAB's *ode15s* function. The PSDs were fit using MATLAB and the *patternsearch* algorithm. All fittings and simulations were performed on an early 2015 MacBook Pro with an Intel Core i5 processor at 2.7 GHz and 8 GB 1867 MHz DDR3 RAM. The code is freely available on github at the following link: https://github.com/drhandwerk/pbm.

Each mechanism was studied by running at least 100 iterations of the *patternsearch* algorithm unless the algorithm converged earlier. Fittings were done to the final, end-time histogram, and the integral  $L^1$  norm was used as the objective function with the *trapz* function after interpolating the experimental data and the simulated solution to be on the same domain via *griddedInterpolant*. The best function value (BFV) is the last result of the objective function with smaller BFVs indicating better agreement between the experimental data and the fit (i.e., smaller BFVs equal better fits). BFVs are reported in all ME-PBM figure captions. The PEStep mechanisms employed are given in the Results section of the main text followed by the resulting histogram fit and simulated precursor versus time curve. The systems of ODEs used for each ME-PBM are reported in the Supporting Information.

2.13. Is a Volume Versus Surface-Area Correction of the ME-PBM, or Perhaps Any of the Data or Resultant Rate Constants from Any of the Methods of Monitoring the Reaction, Needed to Be Able to Compare the ME-PBM to the Experimental Results? A question that comes up is if either the ME-PBM, or perhaps any of the experimental data or  $k_2$  rate constants from the various CHCRR, GLC, XANES, or SAXS monitoring of the nanoparticle formation reaction, require a volume versus surface area correction? This question arises because the simple two-step mechanism,  $A \rightarrow$ B, A + B  $\rightarrow$  2B, as written refers to the total volume or total number (i.e., also the total concentration) of B, eq 17, yet physically nanoparticle growth (i.e., nonaggregative growth) occurs only on the surface atoms of the particle—that is, only surface Ir(0) atoms can participate in surface autocatalytic growth, eq 18 (or e.g., in the CHCRR, which is also a surfacecatalysis phenomena)

$$-\frac{\mathrm{d[A]}}{\mathrm{d}t} = +\frac{\mathrm{d[B]_{Total}}}{\mathrm{d}t} = k_{\mathrm{l}}[\mathrm{A}] + k_{\mathrm{2,T}}[\mathrm{A}][\mathrm{B}]_{\mathrm{Total}}$$
 
$$\mathrm{B_{Total}} \text{ equation, } k_{\mathrm{2,T}} \tag{17}$$

[where T = total is the total volume or equivalently total number (i.e., total concentration) of B]

$$-\frac{d[A]}{dt} = +\frac{d[B]_s}{dt} = k_1[A] + k_{2,s}[A][B]_s$$

$$B_{Surface} \text{ equation, } k_{2,s}$$
(18)

(where s = surface atoms).

As derived and explained in detail in the Supporting Information, with a bit of thought several things become apparent, most importantly that: (i) because the particles are growing physically by *surface* growth, all of the physical methods employed are ultimately measuring  $[B]_{Surface}$  and, hence,  $k_{2,s}$  (and not  $k_{2,T}$ ). However, (ii) the ME-PBM is a total particle number balance, that is, a total volume or (total)

concentration of product, B, based model. Hence, (only) the ME-PBM needs to be corrected to account for the difference between the ratio of surface monomers/total monomers, as a function of the total monomer number, j, for the purposes of the ME-PBM (and as coded, as n, e.g., was already used for another variable in the code). Just such a r(j) = surface monomers/total monomer function is part of the ME-PBM. <sup>18,19</sup>

The end result is that the kinetics curves and resultant  $k_2$  values from all the physical methods and the ME-PBM are directly comparable as reported, and yield a  $k_2 = k_{2,\text{surface}}$  value. A table of each method and what  $k_2$  growth constant that method measures (Table S3), a derivation, and additional equations and discussion are provided in the Supporting Information.

2.14. Effects of Authentic tetra-Iridium-Hydride Cluster, Ir<sup>1</sup><sub>4</sub>H<sub>4</sub>(1,5-COD)<sub>4</sub>, on the Particle Formation Reaction: Does Addition of This Model of a Small, Kinetically Effective Nucleus<sup>61</sup> Accelerate the Particle Formation Reaction as Expected? In the first of two sets of intriguing control experiments, a normal  $\{[(COD)Ir^I\cdot HPO_4]_2\}^{2-}$  (0.003 M) in 2.5 mL of acetone and 0.5 mL of 1.65 M cyclohexene  $Ir(0)_n$  particle formation reaction was run, first, without, and then in a second independent experiment with, the crystallographically (as well as NMR, IR, mass spectrometry, UV-vis, and XAFS) characterized, 50,51 discrete, tetra-iridium-hydride cluster,  $Ir_4^IH_4(1,5\text{-COD})_4$  (9 × 10<sup>-5</sup> M, 0.25  $\mu$ mol = ~1.5% by weight in Ir versus {[(COD)Ir<sup>I</sup>· HPO<sub>4</sub>]<sub>2</sub>}<sup>2-</sup>). Both particle formations and associated CHCRRs were conducted as usual at 22.0  $\pm$  0.1 °C and initial 40 psig H<sub>2</sub>. The results of these experiments are given in Figure S6 of the Supporting Information.

Because the above reaction with no added Ir 4H<sub>4</sub>(1,5-COD)<sub>4</sub> produced faster rate constants than normally seen in a set of 12 repeat standard condition  $Ir(0)_n$  formation reactions and because COVID-19 restrictions limited our ability to repeat these particular nonessential but interesting control experiments, a second, independent set of two additional  $Ir(0)_n$ particle formation control reactions that we could do were performed and proved quite interesting. Those experiments employed [(COD)Ir<sup>I</sup>Cl]<sub>2</sub> (0.003 M) as the precursor with 3 molar equiv of (Bu<sub>4</sub>N)<sup>+</sup>Cl<sup>-</sup> added to slow the reaction kinetics to a range of days rather than hours. The two kinetics runs were performed analogous to those above, without to start and then with,  $Ir_4^I H_4(1,5\text{-COD})_4 (1 \times 10^{-4} \text{ M}, 0.41 \ \mu\text{mol} = \sim 2\%$ by weight in Ir), all under the otherwise identical conditions as above including 22.0  $\pm$  0.1 °C and initial 40 psig  $H_2$ . The results of these two additional control experiments are given as Figure S7 of the Supporting Information. Most intriguingly, the reaction without  $\operatorname{Ir}_{4}^{I}H_{4}(1,5\text{-COD})_{4}$  took >5 days ( $\geq 120$ h), whereas the reaction with  $Ir_4^1H_4(1,5-COD)_4$  went to completion within 1 h, an acceleration of more than  $10^2$ .

# 3. RESULTS

3.1. Monitoring of the  $Ir^1$  to  $Ir^0$  Conversion by XANES Spectroscopy as Well as by Tandem CHCRR Monitoring. XANES spectroscopy was used to monitor the  $Ir^1$  to  $Ir^0$  conversion for the  $\{[(COD)Ir^1\cdot HPO_4]_2\}^{2-}$  system at 5.0 mM Ir and 1.8, 2.25, and 2.7 equiv of  $HPO_4^{2-}$  at the SSRL in a modified F-P bottle pressure cell that also allowed tandem monitoring by the indirect CHCRR method. EXAFS data were obtained for the final  $Ir(0)_n$  nanoparticle product (Figure S1 of the Supporting Information). The 4 min-per-scan, XANES

kinetic experiments with 5.0 mM and 2.25 equiv  $HPO_4^{2-}$  are given below as Figure 2.

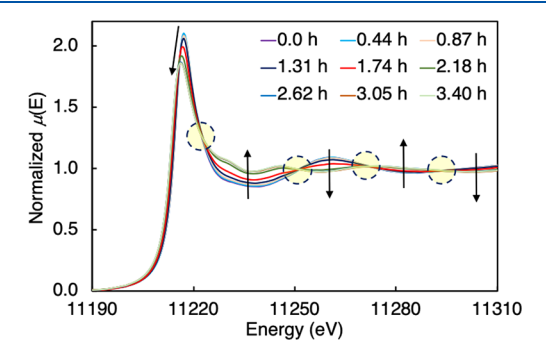


**Figure 2.** XAFS spectra evolution—normalized  $\mu(E)$  vs energy (eV)—of the Ir  $L_3$ -edge as a function of reduction time with 5.0 mM [(COD)Ir<sup>1</sup>(NCCH<sub>3</sub>)<sub>2</sub>][BF<sub>4</sub>] and 2.25 molar equiv of (Bu<sub>4</sub>N)<sub>2</sub>HPO<sub>4</sub>. The XAFS shows four tight isosbestic points at 11,222.7, 11,251.2, 11,271.9, and 11,293.5 eV. A total of 40 spectra were collected over 3.40 h, but only every fifth spectrum is given for visual clarity.

Each spectrum from Figure 2 was processed as described in the Experimental Section, vide supra, to yield the amount of iridium as Ir<sup>I</sup> versus Ir<sup>0</sup> as a function of time, Figure 3. Concurrently with the XANES measurements, tandem CHCRR data were collected. Next and upon return from the synchrotron, identical but in-house CHCRR experiments were conducted. Furthermore, in-house COA evolution by GLC was performed. The four techniques—XANES, tandem CHCRR, in-house CHCRR, and in-house GLC—are coplotted in Figure 3 along with their COPASI-based fits to the two-step mechanism via eq 11, vide supra.

The kinetics curves for all four methods and all five entries in Table 1 are sigmoidal, semiquantitatively similar, but certainly not identical. The tandem CHCRR, in-house CHCRR, and  $GLC_{COA}$  monitoring experimental curves are flat within experimental error during the majority of the induction period. Noteworthy is that the XANES begins an immediate, if slight, downward slope at the start of the reaction. All four experiments exhibit a sharp downward turn following the induction period and, again, an overall sigmoidal shape as expected.

Notable is that the tandem CHCRR reaction (i.e., done at the same time as the XANES, in the same XAFS-modified F–P bottle cell as described in the Experimental Section) is distinct from both the (tandem) XANES and the in-house CHCRR, resulting in an apparent  $10^2$  difference in  $k_{\rm lobs}$  and a 2-fold difference in (compensating, correlated variable  $^{118}$ )  $k_{\rm 2obs}$ . Table 1. Application of a z-test results in a >5 $\sigma$  difference between the tandem CHCRR data and either the XANES or the in-house CHCRR data, meaning that the tandem CHCRR is a statistical outlier by >3 $\sigma$ . If one refits the tandem CHCRR kinetics with  $k_{\rm 2obs}$  constrained to  $k_{\rm 2obs}=634~{\rm h}^{-1}~{\rm M}^{-1}$  from fitting the XANES data, (compensating, correlated variable  $^{118}$ )  $k_{\rm 1obs}$  falls back in line with  $k_{\rm 1obs}\approx 10^{-3}~{\rm h}^{-1}$  values in Table 1— although the predicted curve shifts as expected to be more like the XANES curve and is a poorer fit to the CHCRR curve, Figure S8 of the Supporting Information.

When one compares the resultant rate constants from fitting the datasets with the two-step mechanism (as shown in Table 1) but now excluding the tandem CHCRR >  $5\sigma$  outlier, the XANES, in-house CHCRR, and GLC<sub>COA</sub>  $k_{1\text{obs}}$  values all fall

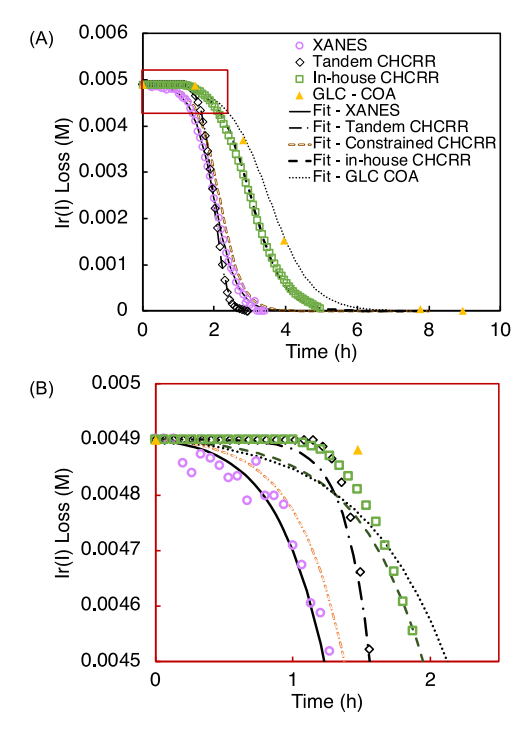


Figure 3. (A) XANES (open purple circles), Tandem CHCRR (black open diamonds), in-house CHCRR (open green squares), and GLC<sub>COA</sub> (solid gold triangles) kinetics data are coplotted with their fits to the FW two-step mechanism (solid, dot-dashed, dashed, and dotted lines, respectively). An additional fit line (brown hallow dash) is given for when  $k_{\rm 2obs}$  is constrained to the XANES fit value and  $k_{\rm 1obs}$  is allowed to vary. (B) A closer look at the first 2 h of the reaction, where the majority of nucleation is observed to take place. Experiments were conducted at 5.0 mM [(COD)Ir<sup>I</sup>(NCCH<sub>3</sub>)<sub>2</sub>][BF<sub>4</sub>] and 2.25 molar equiv of (Bu<sub>4</sub>N)<sub>2</sub>HPO<sub>4</sub>. Additional experiments, with similar kinetic profiles, were conducted at 1.8 and 2.7 molar equiv of (Bu<sub>4</sub>N)<sub>2</sub>HPO<sub>4</sub> and are reported in Table 1. Rate constants for all four experiments under XANES conditions are reported below in Table 1. Only every fifth data point from the in-house CHCRR is shown to avoid cluttering the already busy figure.

Table 1. Rate Constants from the Synchrotron XANES, Tandem CHCRR at Synchrotron, In-House CHCRR, and In-House COA Evolution at 5.0 mM [(1,5-COD)Ir<sup>I</sup>(NCCH<sub>3</sub>)<sub>2</sub>][BF<sub>4</sub>] and 2.25 molar equiv  $(Bu_4N)_2HPO_4$ 

methods	$k_{1  ext{obs}} (h^{-1})$	$(h^{-1}M^{-1})$
XANES <sup>a</sup>	$(6.2 \pm 0.3) \times 10^{-3}$	$634 \pm 5$
tandem CHCRR <sup>a,c</sup>	$(6.6 \pm 0.3) \times 10^{-5}$	$1170\pm6$
tandem CHCRR <sup><math>a,d</math></sup> (reanalyzed with $k_{2\text{obs}}$ constrained) <sup><math>d</math></sup>	$(3.9 \pm 0.8) \times 10^{-3}$	[634] <sup>c</sup>
triplicate in-house CHCRR <sup>b</sup>	$(5 \pm 1) \times 10^{-3}$	$331 \pm 28$
$GLC_{aa}$	$(4.2 \pm 0.7) \times 10^{-3}$	290 + 10

"Reported rate constant error for  $k_1$  and  $k_2$  is the fitting error. Behavior are constant error for  $k_1$  and  $k_2$  is the standard error from three replicate measurements. This tandem CHCRR entry is an outlier according to a z-test of > $\pm 3\sigma$  (> $5\sigma$  is observed, vide infra) when comparing the triplicate in-house CHCRR and the tandem CHCRR. A z-test between the XANES and the tandem CHCRR yielded the same results and, the z-test of  $k_{1\text{obs}} > 5\sigma$ ,  $\sigma = \pm 0.001$ . This entry constrains  $k_{2\text{obs}}$  to the value seen for the tandem XANES of  $k_{2\text{obs}} = 634 \, \text{h}^{-1} \, \text{M}^{-1}$  to see if the data can still be fit and to see what  $k_{1\text{obs}}$  value results.

within a factor of ~1.6 fold when one ratios the largest versus and smallest  $k_{\rm 1obs}$  entry in Table 1 (or, statistically, by a factor of ~1.5  $\sigma$ ,  $\sigma$  = 0.001 for  $k_{\rm 1obs}$ ). This level of agreement of  $k_{\rm 1obs}$  within a fact of ~1.5 (postdiscarding the tandem CHCRR outlier) is actually not too bad given that nucleation rate constants are notoriously hard to measure, even to  $\pm 10^1$ , <sup>62,95,130</sup> and hence will be defined herein as "broad" (~2-fold) agreement. The  $k_{\rm 2obs}$  values are similarly in broad agreement within a factor of ~2.2 between the largest versus smallest  $k_{\rm 2obs}$  value (or, statistically, by a factor of ~1.8  $\sigma$ ,  $\sigma$  = 188 for  $k_{\rm 2obs}$ ). The average  $k_{\rm 2obs}$  in Table 1 is  $k_{\rm 2obs}$  = (418  $\pm$  66) h<sup>-1</sup> M<sup>-1</sup> and hence approaching error bars closer to what a small-molecule chemist might be more comfortable with—but are generally harder to achieve in materials chemistry.

Even though the in-house and tandem CHCRR are ostensibly the same monitoring method, it seems inescapable that there is some difference in conditions of the two separate experiments despite every effort to keep solvent, cyclohexene, temperature, and other conditions identical and despite the effort to construct a near-identical reaction vessel out of a F–P pressure bottle (i.e., that differs only in its necessary Kapton windows needed to allow the XANES experiments, as detailed in the Experimental Section).

One obvious difference is that the XANES sample is irradiated with high-energy X-ray radiation. Hence, the possibility exists of well-precedented X-ray-induced radiolysis 104-108 being an unwelcome component of the synchrotron X-ray-based methods. Radiolysis can knock electrons off of even  $\mathrm{Zn^{2+}}$  in ionic liquids or melts,  $\mathrm{Zn^{2+}} + h\nu \rightarrow \mathrm{e^-} + \mathrm{Zn^{3+}}^{.104}$ Solvated e are of course strong reductants and, hence, could easily add to or even start Ir<sup>I</sup> reduction, thereby speeding up both nucleation and autocatalytic, exponential, "explosive" growth—possibilities consistent with the observed, accelerated sigmoidal kinetics curve CHCRR tandem to the XANES (as well as the accelerated CHCRR tandem to the SAXS in the next section). Overall, radiolysis plus at least three other possibilities exist for the quantitative differences in the  $k_{1\text{obs}}$ and  $k_{20bs}$  values seen in Table 1. Those possibilities are summarized in the Supporting Information for now, as it will prove useful to have in hand all of the kinetics data obtained by all of the monitoring methods, as well as the average of those  $k_{1\text{obs}}$  and  $k_{2\text{obs}}$  values, before addressing possible sources of error in individual measurements by the different methods in the Discussion section.

3.2. Monitoring of the  $Ir(0)_{\sim 150} \cdot (HPO_4^{2-})_x$  Nanoparticle Formation by SAXS. The kinetics of nanoparticle formation were also monitored by in situ SAXS in separate experiments done at a separate synchrotron facility with different expert collaborators as detailed in the Experimental Section. Note that in the SAXS results shown in Figure 4, the concentration of the iridium precursor was necessarily increased from the value in the XANES experiments of 5.0 to 9.0 mM in the SAXS experiments in order to better observe particle formation at early times—which we will see still proved insufficient to allow scattering beyond the solvent background sufficient to allow observation of particles smaller than ca. 0.8 nm. The amount of stabilizer was also increased (from 2.25 molar equiv vs Ir to 3.6 equiv) to slow the reaction to an observable rate at early times, something that is an advantage of the Ir<sup>I</sup>(1,5-COD)<sup>+</sup>/HPO<sub>4</sub><sup>2-</sup> system, namely the ability to prepare in situ and thereby tune the system and its kinetics for the monitoring method at hand. We will, however and in turn, see that the extra equivalents of the HPO<sub>4</sub><sup>2-</sup>

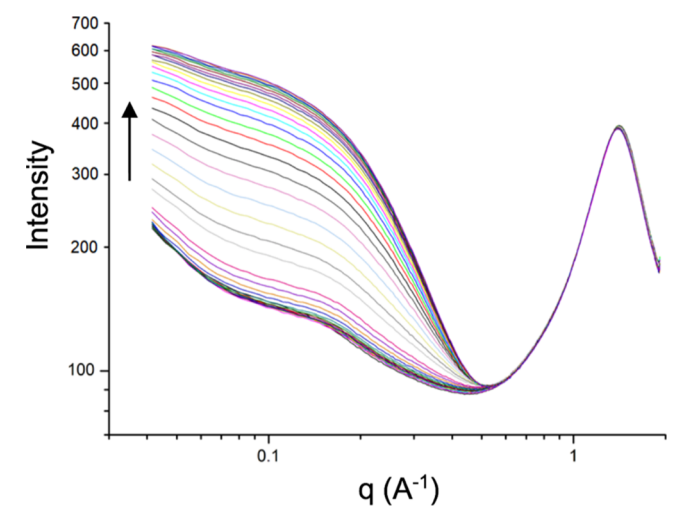


**Figure 4.** Evolution of the scattering intensity by SAXS with intensity plotted against q (Å $^{-1}$ ). Samples were prepared at 9.0 mM [(COD)Ir $^{I}$ (NCCH $_3$ ) $_2$ ][BF $_4$ ] and 3.6 molar equiv of (Bu $_4$ N) $_2$ HPO $_4$  in 5.0 mL acetone and 1.0 mL cyclohexene. Data were collected every 76 s over 4 h. The solvent scattering background (the peak at  $\sim$ 1.5 A $^{-1}$ ) is substantial so that the first 1 h proved to be unusable due to solvent interference compared to small-particle scattering (i.e., the solvent scattering background has deliberately not been subtracted in this figure so as to illustrate the magnitude of the signal from the solvent vs small particle scattering at early times). Fits to log—normal, Gaussian, and Schulz size-distribution functions and the resulting fit parameters and  $R^2$  values are provided in Figure S4 and Table S2, respectively, of the Supporting Information.

stabilizer have the expected slowing effect on the CHCRR, presumably due to ligand capping of the  $Ir(0)_n$  product particles. Additionally, the in situ SAXS were necessarily conducted using a custom-built SAXS cell able to handle the  $H_2$  gas reactant, Figure S3 of the Supporting Information, a reactor different than the F-P bottle used in the XAFS and tandem CHCRR. The different cell and somewhat different reaction conditions come naturally, albeit unfortunately, with the different monitoring methods as one strives to optimize each physical method for the problem at hand.

The intensity versus q data were processed using eq 12, described vide supra in the Experimental Section. The kinetics of nanoparticle volume were extracted from the SAXS data and yield a smooth, ascending, Ir(0) formation concentration versus time sigmoidal kinetics curve as shown in Figure 5A. The expanded part of the kinetics curves showing just the first ca. 3 h, Figure 5B, reveals that solvent scattering appears to dominate the SAXS signal in the first, ca. 1 h. Hence, nucleation is not well captured by these particular SAXS experiments nor could a reliable number of particles versus time be obtained from these particular experiments, an otherwise very valuable part of the SAXS method. However, the SAXS formation kinetics could be fit fairly closely by the two-step mechanism, eq 11, as displayed in Figure 5A.

All the curves are sigmoidal and once again in at least broad agreement, save the COA evolution monitored by GLC that is slowed noticeably and, hence, a bit of an outlier, as discussed more in a moment. The synchrotron-based SAXS kinetics data are, once again (i.e., as with the XANES data) a bit faster than the in-house CHCRR. Also noticeable is that the tandem CHCRR done in concert with the SAXS is visually rather different—again appearing sooner (faster) than the in-house

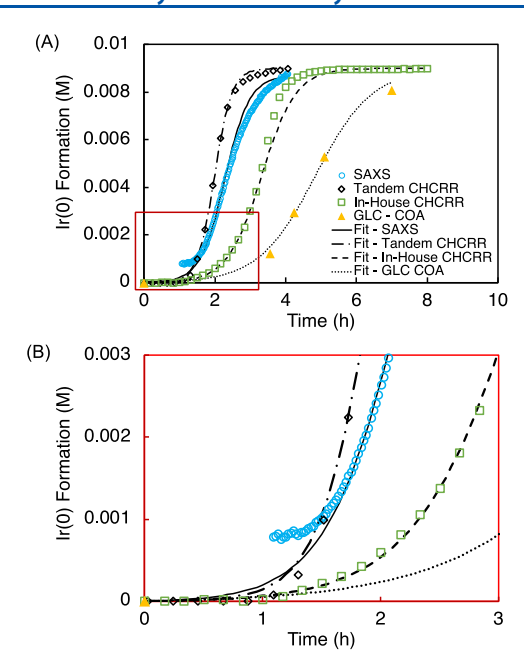


Figure 5. (A) SAXS (open blue circles), simultaneously collected tandem CHCRR (open black diamonds), in-house CHCRR (open green squares), and COA evolution (solid gold triangles) kinetics data are plotted with their fits to the two-step mechanism (solid, dot-dashed, dashed, and dotted lines, respectively). (B) A closer look at the first 3 h of the reaction, where the majority of nucleation is observed to take place. Experiments were conducted at 9.0 mM [(COD)Ir<sup>I</sup>(NCCH<sub>3</sub>)<sub>2</sub>][BF<sub>4</sub>] and 3.6 molar equiv of (Bu<sub>4</sub>N)<sub>2</sub>HPO<sub>4</sub>. Rate constants for all four experiments under XANES conditions are reported below in Table 2. For both CHCRR datasets, only every 10th data point is given for visual clarity.

CHCRR and even undercutting the SAXS data, much like the tandem CHCRR to the XANES undercut that data back in Figure 3. During the SAXS, some visually observable fouling of the cell windows occurred as the experiment progressed, presumably insoluble  $Ir(0)_n$  formation and plating, the possible origins of which are deferred until the Discussion section.

Looking at the results quantitatively by fitting to the twostep mechanism, the  $k_{1 \text{obs}}$  values in Table 2 are all within a

Table 2. Rate Constants from Synchrotron SAXS, Tandem CHCRR, In-House CHCRR, and COA Evolution at 9.0 mM  $[(1,5\text{-COD})\text{Ir}^I(\text{NCCH}_3)_2][\text{BF}_4]$  and 3.6 molar equiv  $(\text{Bu}_4\text{N})_2\text{HPO}_4$ 

	methods	$k_{1 \text{obs}} \; (h^{-1})$	$k_{2\text{obs}} \; (h^{-1} \; M^{-1})$
SAXS <sup>a</sup>		$(4 \pm 2) \times 10^{-3}$	$332 \pm 3$
tandem (	CHCRR <sup>a</sup>	$(1.1 \pm 0.2) \times 10^{-3}$	$460 \pm 3$
triplicate	in-house CHCRR <sup>b</sup>	$(2.4 \pm 0.5) \times 10^{-3}$	$401 \pm 85$
$GLC_{COA}$	a	$(2.9 \pm 0.8) \times 10^{-3}$	$138 \pm 7$

<sup>a</sup>Reported rate constant error for  $k_1$  and  $k_2$  is the fitting error. <sup>b</sup>Reported rate constant error for  $k_1$  and  $k_2$  is the standard error from three replicate measurements.

factor of 2 of one another, thereby paralleling what was seen for the XANES  $k_{1\text{obs}}$  values back in Table 1. Additionally, the average  $k_{1\text{obs}}$  for the data in Table 2 is  $k_{1\text{obs}} = (2.6 \pm 1.2) \times 10^{-3} \, \text{h}^{-1}$ , also within a factor of 2 of the average  $k_{1\text{obs}}$  back in Table 1 of  $k_{1\text{obs}} = (5.2 \pm 0.7) \times 10^{-3} \, \text{h}^{-1}$  (and after discarding the tandem CHCRR outlier back in Table 1). Once again the ~2-fold agreement is not what would make a small-molecule

chemist happy, but is actually at least 5-fold better than the  $\geq$   $\pm 10^1$  variation often seen for nucleation rate constants. 61,95,130

The  $k_{2\text{obs}}$  values in Table 2 are in general agreement, now within a factor of ca. 40% (the first vs second  $k_{2\text{obs}}$  entries in Table 2), other than the COA evolution  $k_{2\text{obs}}$  (which is a factor of ~3.3 off from the largest  $k_{2\text{obs}}$  in Table 2, beyond what is normally seen in comparison to the in-house CHCRR). The average  $k_{2\text{obs}}$  value for the SAXS data in Table 2 is  $k_{2\text{obs}} = (332 \pm 120) \, \text{h}^{-1} \, \text{M}^{-1}$ , an average  $k_{2\text{obs}}$  value that is pleasingly within 25% of (and thereby well within experimental error of) the average  $k_{2\text{obs}}$  value in Table 1 of  $k_{2\text{obs}} = (418 \pm 66) \, \text{h}^{-1} \, \text{M}^{-1}$ , and after discarding the tandem CHCRR outlier back in Table 1.

3.3. Global Fitting of the XANES Table 1, SAXS Table 2, and Combined Tables 1 and 2 Data to Obtain  $k_{1\text{obs,avg}}$  and  $k_{2\text{obs,avg}}$  and  $k_{1\text{obs,global avg}}$  and  $k_{2\text{obs,global avg}}$  Rate Constants. Overall, from the SAXS plus the XANES kinetics, along with the supporting CHCRR and GLC kinetics, one can conclude that: (i) the basic sigmoidal shape is seen in all kinetics curves, (ii) that a minimal two-step mechanism can be used to extract nucleation  $k_{1\text{obs}}$  and autocatalytic surface growth  $k_{2\text{obs}}$  rate constants, but (iii) that individual kinetic runs monitored by different methods can produce  $k_{1\text{obs}}$  as well as  $k_{2\text{obs}}$  values that differ by up to a factor of  $\sim$ 2.

We wondered how we might best treat the combined kinetics data (1178 total data points) in the absence of a resolution to issues such as possible X-ray radiation-induced artifacts and associated possible systematic errors in the XANES or SAXS data. Because it is not obvious what would constitute a better treatment of the composite data at this time, we simply combined the data in three different, arguably logical ways and looked at what a fit to each of those combined data sets yielded, thereby setting aside for the time being possible issues of different precision or errors and the different amounts of data from the various methods—an admittedly zeroth-order treatment of the kinetics data as is possible at this time

First, we compute the average of all the results in Table 1 for  $k_{1\text{obs}}$  and then  $k_{2\text{obs}}$  (again sans the entry 2 outlier) and then, separately, all of the  $k_{1\text{obs}}$  and then  $k_{2\text{obs}}$  data in Table 2, just to see what results. For the Table 1 data, a global average  $k_{1\text{obs}(\text{avg,Table 1})} = (2.2 \pm 0.3) \times 10^{-2} \text{ h}^{-1}$  and  $k_{2\text{obs}(\text{avg,Table 1})} = (3.7 \pm 0.1) \times 10^2 \text{ h}^{-1}$  M $^{-1}$ . For the Table 2 data, the global average  $k_{1\text{obs}(\text{avg,Table 2})} = (1.7 \pm 0.2) \times 10^{-2} \text{ h}^{-1}$  and  $k_{2\text{obs}(\text{avg,Table 2})} = (2.0 \pm 0.1) \times 10^2 \text{ h}^{-1}$  M $^{-1}$ . Plots of the Table 1 and then Table 2 experimental data in comparison to the global average fits are shown in Figure 6. A summary of the global fit  $k_{1\text{obs}}$  and  $k_{2\text{obs}}$  values is shown in Table 3, along with the results of a global fit to all the kinetics data from Tables 1 and 2 combined (the 1178 total data points). A section in the Supporting Information contains details on how the composite data were combined and treated, as well as Figure S9 that shows the fitted, global-average kinetics curve versus all of the input data.

As one expects, combining the data does yield an average curve that visually accounts for the (average) data. Combining the data also has the expected effect of lowering the resultant error bars while yielding the global-average estimates of  $k_{\rm 1obs,global~avg} = (1.5 \pm 0.1) \times 10^{-2}~{\rm h}^{-1}$  and  $k_{\rm 2obs,global~avg} = (2.4 \pm 0.1) \times 10^{2}~{\rm h}^{-1}~{\rm M}^{-1}$  of relative estimated precisions  $\pm 7$  and  $\pm 4\%$ , respectively. Despite the assumptions and approximations behind this zeroth-order treatment of the composite data, the  $k_{\rm 1obs,global~avg}$  and  $k_{\rm 2obs,global~avg}$  values are presently our most

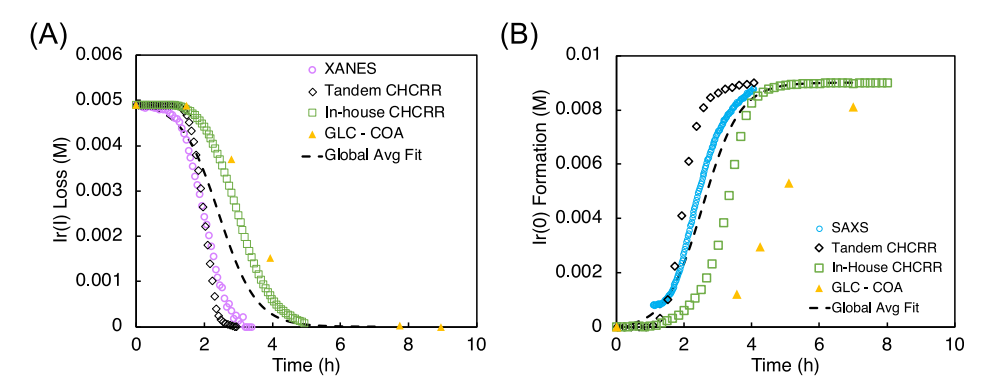


Figure 6. (A) Data reproduced from main text Figure 3a. A global fit of the data was performed and is given as a dashed black line. Resultant rate constants are  $k_{1\text{obs}(avg,Table 1)} = (2.2 \pm 0.3) \times 10^{-2} \text{ h}^{-1}$  and  $k_{2\text{obs}(avg,Table 1)} = (3.7 \pm 0.1) \times 10^{2} \text{ h}^{-1}$  M<sup>-1</sup>. (B) Data reproduced from main text Figure 5A. A global fit of the data was performed and is given, again, as a dashed black line. Resultant rate constants are  $k_{1\text{obs}(avg,Table 2)} = (1.7 \pm 0.2) \times 10^{-2} \text{ h}^{-1}$  and  $k_{2\text{obs}(avg,Table 2)} = (2.0 \pm 0.1) \times 10^{2} \text{ h}^{-1}$  M<sup>-1</sup>.

Table 3. Summary of the  $k_{1\text{obs,avg}}$  and  $k_{2\text{obs,avg}}$  Values from a Global Fitting of the Kinetic Data in Tables 1,2 and Tables 1 and 2 Combined

data source	$k_{ m lobs,avg}~({ m h}^{-1})~(\%~{ m std}~{ m deviation})$	$k_{ m 2obs,avg}~({ m h}^{-1}~{ m M}^{-1})~(\%~{ m std}~{ m deviation})$
Table 1 data <sup>a</sup> (XANES + other methods)	$(2.2 \pm 0.3) \times 10^{-2} (\pm 14\%)$	$(3.7 \pm 0.1) \times 10^2 (\pm 3\%)$
Table 2 data $^b$ (SAXS + other methods)	$(1.7 \pm 0.2) \times 10^{-2} (\pm 12\%)$	$(2.0 \pm 0.1) \times 10^2 (\pm 5\%)$
all the data (i.e., Tables 1 and 2 data combined) $^c$	$(1.5 \pm 0.1) \times 10^{-2} (\pm 7\%)$	$(2.4 \pm 0.1) \times 10^2 (4\%)$

"As detailed in the Experimental Section, these experiments refer to the specific conditions of 5 mM [{[(COD)Ir<sup>1</sup>·HPO<sub>4</sub>]<sub>2</sub>}<sup>2-</sup>] and 2.5 added equiv of HPO<sub>4</sub><sup>2-</sup>, as well as the initial ~1.65 M cyclohexene and ~55 psig H<sub>2</sub> of the experiment and associated CHCRR. <sup>b</sup>As detailed in the Experimental Section, these experiments refer to the specific conditions of 9 mM [{[(COD)Ir<sup>1</sup>·HPO<sub>4</sub>]<sub>2</sub>}<sup>2-</sup>] and 3.6 added equiv of HPO<sub>4</sub><sup>2-</sup> as well as the initial ~1.65 M cyclohexene and ~40 psig H<sub>2</sub> of the experiment and associated CHCRR. <sup>c</sup>Combining these data, given their slightly different reaction conditions, is an approximation that effectively assumes that there is minimal further dependence of either  $k_{1\text{obs}}$  and  $k_{2\text{obs}}$  within the 5–9 mM range of initial [{[(COD)Ir<sup>1</sup>·HPO<sub>4</sub>]<sub>2</sub>}<sup>2-</sup>] and minimal further dependence of either  $k_{1\text{obs}}$  and  $k_{2\text{obs}}$  within the 2.5–3.6 range of added equiv of HPO<sub>4</sub><sup>2-</sup>. Evidence that combining these data is acceptable for the purposes of the present work and within the reported error bars of the resultant rate constants is provided by Figures 4, 5, and S8 available in a 2019 publication. <sup>63</sup>

precise, and given the multiple (four) monitoring sources employed almost surely our most accurate, estimates of the rate constants for the nucleation and autocatalytic surfacegrowth PESteps of the two-step particle formation mechanism. Also illustrated in this section are the type(s) and amounts of data needed to get to the observed error estimates.

**3.4.** Collection of TEM-Determined Particle Size Distributions Versus Time. Under the same specific conditions as those of the XANES experiments, samples of the  $Ir(0)_n$  nanoparticle product were collected four times throughout the reaction and examined by STEM. The particle size distributions at 1.5, 3.25, 5.0, and 10.0 h are given in Figure 7. The average diameter, average nuclearity, and polydispersity at each time point are given in Table 4. Worth noting here is that a series of controls done in 1994 for our first  $Ir(0)_n$  nanoparticles are quite stable in typical TEM beams, one reason among others<sup>63</sup> as detailed in the Supporting Information that we picked them as our prototype system for study.

Ex situ STEM measurements show the rapid growth of particles past (i.e., larger than) the kinetics-determined kinetically effective nucleus (KEN)<sup>61</sup> of  $Ir(0)_2$ . By 0.75 h, the average particle size is  $\sim Ir(0)_{13}$ . At 1.5 h, where the induction period is over (i.e., in most of the kinetics curves in Figures 3 and 5, regardless of the monitoring method used), the average particle nuclearity is  $\sim$ 26. Hence, one can say that a catalytically effective nucleus (CEN)<sup>90</sup> of  $\leq$ 26 is for sure formed by the end of the 1.5 h induction period that can perform the hydrogenation catalysis required for the CHCRR.

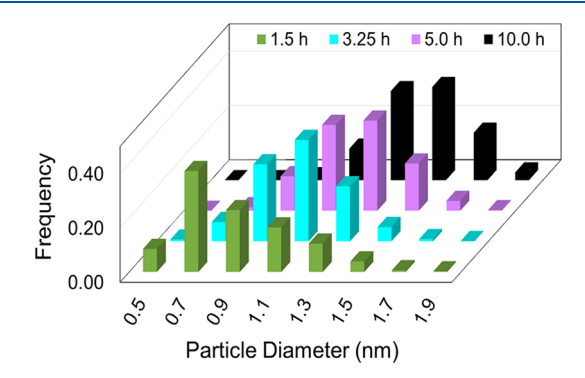


Figure 7. Particle size distributions for the formation of  $Ir(0)_n$  nanoparticles at 1.5 h (green), 3.25 h (teal), 5.0 h (purple), and 10.0 h (black). At each time point, a new reaction solution was prepared of 5.0 mM [(1,5-COD)Ir<sup>I</sup>(NCCH<sub>3</sub>)<sub>2</sub>][BF<sub>4</sub>] in the presence of 2.25 molar equiv of  $(Bu_4N)_2HPO_4$  in 3.33 mL acetone and 0.67 mL cyclohexene at 22.0  $\pm$  0.1 °C. Each data point represents >450 measured particles; across the 4 samples, >2700 particles were measured and binned in 0.2 nm bins. These TEM images confirm and expand those provided elsewhere, <sup>63</sup> images that can be consulted if the reader wants to see typical TEMs for this  $Ir(0)_n/HPO_4^{2-}$  nanoparticle system.

Additionally, the finding  $^{63}$  of a KEN of just  $Ir_2$  able to reduce/hydrogenate additional  $Ir^I(1,5\text{-COD})^+$  moieties to Ir(0) and COA implies that the CEN starts with  $Ir_2$ .

The growth continues to, on average, the next magic number size,  $\sim Ir(0)_{55}$ , at  $\sim 3.25$  h. Growth stops at an average within error of the next, third (Ir<sub>147</sub>) magic number, Ir(0) $_{\sim 150}$ , with HPO<sub>4</sub> $^{2-}$  stabilizer ligand-capping as an almost surely important

Table 4. Summary of Time-Resolved STEM under XANES Conditions, 5.0 mM Ir, and 2.25 molar equiv (Bu<sub>4</sub>N)<sub>2</sub>HPO<sub>4</sub>

time (h)	average diameter (nm)	average nuclearity	dispersity (%)
0.75	$0.7 \pm 0.4$	13	56
1.5	$0.9 \pm 0.3$	26	30
3.25	$1.1 \pm 0.2$	55	19
5.0	$1.2 \pm 0.2$	68	17
10.0	$1.4 \pm 0.2$	150	14

chemical component of attaining that relatively small, ~1.4 nm average-size particle that resists agglomeration to larger particles. Importantly, as the size increases, the distribution narrows with a size-focusing 4-fold decrease in polydispersity from an initially observed ±56% to a final ±14%, nearmonodisperse<sup>87</sup> (defined as  $\pm \le 15\%$ )<sup>87</sup> PSD. Note that the smooth progression of the particle sizes argues against any at least significant TEM-beam-induced reduction and then growth of nor damage to the  $Ir(0)_n$  nanoparticles, as expected because the gaseous H2 reductant needed for growth is gone once aliquots are removed and placed on a TEM grid. Also relevant here are extensive control experiments done as early as 45 1994 indicating that (i) third-row-metal  $Ir(0)_n$  nanoparticles are rather stable in TEM beams, and that (ii) at least the {(1,5-COD)Ir<sup>I</sup>·POM}<sup>8-</sup> precursor is stable in TEM beams, 45 two reason among others as detailed in the Supporting Information that the  $\{(1,5\text{-COD})\text{Ir}^{\text{I}}\cdot\text{Anion}\}^{n-1}$ precursor and  $Ir(0)_n$  nanoparticle systems were picked as preferred systems for nanoparticle formation kinetic and mechanistic studies.

An interesting question when scrutinizing the STEM data in Figure 7 and Table 4 is if one can discern any evidence for initial "small" (B) particle agglomeration,  $B + B \rightarrow C$ , as one might expect given the finding that "smaller particles are more reactive", at least in surface autocatalytic growth. 18,19 Intriguingly, the first, green-labeled PSD in Figure 7 shows a distribution of particles centering at ~0.75 nm (Ir<sub>~13</sub> on average) and then at ~0.9 nm (Ir<sub>~26</sub> on average), as well as substantial numbers of particles at  $\sim$ 1.1 nm (Ir $_{\sim55}$  on average). Hence, it is certainly possible that Ir 213 particles undergo aggregative dimerization to form ca. Ir 26 particles that themselves could dimerize to ca. Ir 255 particles. However, such "eye-ball" analysis of the data does not demand this, so that ME-PBM first without and then with aggregation B + B  $\rightarrow$ C in the code will be needed to test if aggregation is part of the particle formation mechanism. That said, one can reasonably infer that ~0.75 nm, on-average Ir<sub>~13</sub> could qualify as "B", smaller average-size particles while ~1.1 nm, on-average Ir<sub>~55</sub> might qualify as the "C", larger average-size particles in terms of the generalized "A, B, C" nomenclature of the minimal mechanisms summarized back in Scheme 2. This can be checked by the ME-PBM, which yields a B versus C cut-off parameter (M), that is predicted by the above analysis of the TEM to be between M = 13 to 55. Looking ahead, the best fitting ME-PBM to the PSD data reported herein yields M =23, vide infra.

3.5. Fitting the Kinetic Data to the New 2019 Three-Step Mechanism Allowing Size-Dependent Surface Growth. We know from the literature 45-63 (i) that the two-step mechanism used so far is the best place to start to analyze and compare the kinetics data of the various kinetics monitoring methods, consistent with (ii) statistical and mathematical considerations teaching that it is generally easier

to determine precisely as well as accurately fewer compared to more parameters, for example, 2- compared to 3- or 4-rate-constant parameters. In any rigorous approach to the determining mechanism, (iii) one must always obey Ockham's razor and add more steps and details to the mechanism only as additional data and evidence demand (see Section 2.6 elsewhere for a discussion of a rigorous, stepwise approach to the mechanisms of more complicated reactions such as nanoparticle formation).

However, we can predict with confidence based on our 2019 and 2020 ME-PBM work<sup>18,19</sup> that the two-step minimum mechanism employed to this point will not be sufficient to account for the observed PSD—a prediction confirmed in an upcoming ME-PBM section. We can also predict from that ME-PBM work<sup>18,19</sup> that the new, net three-step mechanism discussed in the Introduction and shown in eqs 19-i–19-iii, which allows for size-dependent growth, is the minimum mechanism that may be able to account for the observed PSD and, therefore, needs to be examined next.

Hence, we attempted fits of the Figures 3 and 5 kinetics data from the XANES and SAXS studies, respectively, to the new three-step mechanism, eqs 19-i-19-iii, employing as usual the numerical integration package COPASI, 114 with the expectation that (i) a good if not better fit would result, but (ii) that determining precisely additional, now three total rate constant parameters might prove challenging with the relatively limited amount of data from XANES or SAXS.

$$A \xrightarrow{k_1} B \tag{19-i}$$

$$A + B \xrightarrow{k_2} C \tag{19-ii}$$

$$A + C \stackrel{k_3}{\rightarrow} 1.5C \tag{19-iii}$$

The fits using the new, three-step mechanism to the XANES kinetics data (from Figure 3) and the SAXS kinetics data (from Figure 5) are shown in Figure 8A,B. The fits are very good, as expected because the two-step mechanism fits these kinetics curves and we now have one additional rate-constant (fitting) parameter.

The resulting rate constants and fit error estimates for the XANES data are:  $k_{\rm 1obs} = 0.0031 \pm 0.0002 \ {\rm h^{-1}}$ ,  $k_{\rm 2obs} \sim 3 \times 10^6 \ {\rm h^{-1}}$  M<sup>-1</sup>, and  $k_{\rm 3obs} = 1270 \pm 20 \ {\rm h^{-1}}$  M<sup>-1</sup>. The resulting rate constants and fit error estimates for SAXS are:  $k_{\rm 1obs} \sim 0.005 \ {\rm h^{-1}}$ ,  $k_{\rm 2obs} \sim 6 \times 10^6 \ {\rm h^{-1}}$  M<sup>-1</sup>, and  $k_{\rm 3obs} = 522 \pm 3 \ {\rm h^{-1}}$  M<sup>-1</sup>.

Several results from these fits merit noting: (i) the  $k_{\rm lobs}$  value for the XANES data, where there are data during the induction period is within 2-fold of the  $k_{\rm lobs,global~avg}=1.5\times10^{-2}~{\rm h}^{-1}$ , a reassuring result; (ii) in both cases,  $k_{\rm 2obs}>k_{\rm 3obs}$  so that the "smaller grow faster than larger" finding <sup>18,19</sup> is once again observed/supported, a second noteworthy result; but (iii) that for both sets of data  $k_{\rm 2obs}$  is not well determined to within even  $10^{\pm 1}$ , an expected, common problem once one has 3–4 nanoparticle formation rate constant parameters. <sup>59</sup> Nevertheless, a key result for the purposes of the present study is (iv) that the three-step mechanism merits high priority for testing by ME-PBM, as will be done in the next section and after a look first at the ME-PBM for the two-step minimum

3.6. ME-PBM Fitting of the TEM-Determined Particle Size Distribution: a Further, Demanding Test of the Proposed Mechanism. Although reported only in 2019, 18,19,92 ME-PBM has already proved to be a critical

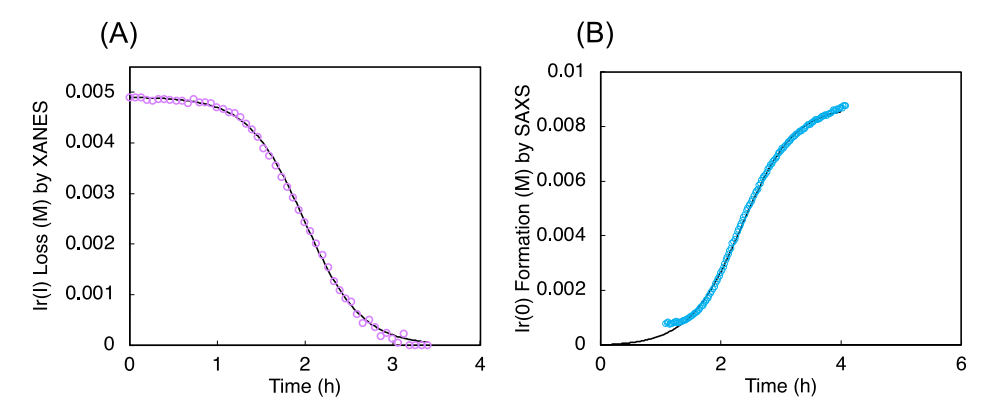


Figure 8. (A) Ir(I) concentration loss from XANES measurements (open purple circles) vs time data and fit using the new three-step mechanism (solid black line). (B) Ir(0) concentration formation from SAXS measurements (open blue circles) vs time data and fit to the new three-step mechanism (solid black line). The rate constants resulting from the fits are provided in the main text.

new tool for testing any proposed mechanism of particle formation. Indeed, our prior work led to the preliminary conclusion as a working hypothesis that "no mechanism of particle formation should be published without testing of and input from the information-rich PSD via ME-PBM". <sup>18</sup>

Hence, it is of considerable interest to further test the above working hypothesis using the TEM-determined PSD data back in Figure 8 obtained as part of the present study. The goal of the initial ME-PBM analysis that follows is primarily (i) to see if the two-step minimum mechanism, which proved capable of fitting the CHCRR, GLC, XANES, and SAXS data, is, however and as expected, <sup>18,19</sup> not able to account for the PSD because the two-step mechanism does not allow size-dependent growth; 18,19 and then (ii) to see if the new three-step mechanism discovered in 2019 can fit the PSD, or (iii) will ME-PBM indicate that some additional step, for example, agglomeration of "smaller" particles,  $B + B \rightarrow C$ , as hinted at in an "eye-ball analysis" of the TEM-determined PSD, be required to fit the observed PSD? Note that we know from our first ME-PBM studies that it is generally easy to get a ME-PBM fit to the CHCRR (and by analogy, the XANES and SAXS) curves themselves, but generally challenging to fit the PSD, and even more challenging to account fully for both the PSD and the kinetics curves. What follows is just our initial ME-PBM analysis given the length of the paper already to just this point. A full ME-PBM analysis, complete with Bayesian inversion statistical analysis and estimates of the reliability of and error bars on the ME-PBM-derived rate constants, is also underway and will be reported in due course.

**3.7. Two-Step Mechanism-Based ME-PBM.** To start, our expectation that the two-step mechanism will not be able to generate the observed PSD was tested by an attempted ME-PBM fitting of the final PSD after 10.0 h shown in Figure 9. We employed the MATLAB code <sup>18,19</sup> developed from the two-step mechanism shown back in Scheme 3, eqs 10 and 11, code that is archived via GITHUB and, hence, readily available to anyone that wants it, as detailed in the Experimental Section.

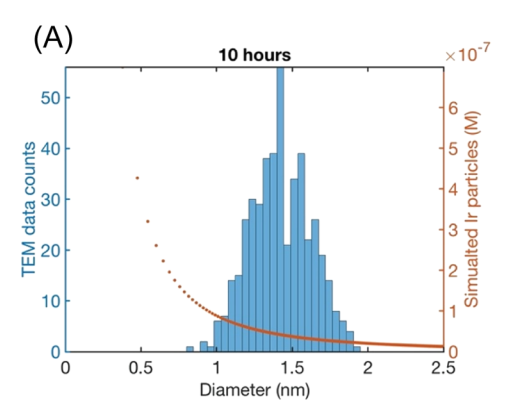
Figure 9 confirms the anticipated result  $^{18,19}$  that the two-step mechanism cannot fit the PSD at all, not even when including the experimentally supported nucleation mechanism. This is as expected,  $^{18,19}$  at a minimum one needs size-dependent growth as in the new three-step mechanism to be able to fit PSDs of at least the  $Ir(0)_n$  systems examined to date,  $^{18,19}$  and in all probability more generally to fit PSDs in other systems as well.  $^{18,19}$ 

**3.8.** New Three-Step Mechanism-Based ME-PBM. We quickly turned our attention next to trying a ME-PBM model based on the recently discovered three-step mechanism, <sup>18,19</sup> while also including the experimentally supported nucleation mechanism shown back in eqs 10 and 11. Recall that the three-step mechanism was able to fit closely the XANES and SAXS kinetics data as shown back in Figure 8.

Figure 10 shows the attempted fit of the PSD using a ME-PBM code based on the new three-step mechanism. While the right-most edge of the PSD is now reasonably accounted for, and the BFV has dropped considerably from 90.0 to a BFV = 37.2 indicating a better fit (as expected given the additional rate constant parameter in the three-step mechanism), the fit to the left-hand side of the PSD is poor indicating that this ME-PBM model yields too many small particles. Additionally, the predicted A-loss curve using the PSD-fitted rate constants is not even close to the experimental A-loss curve, taking off immediately without any observable induction period, indicating that a further revised mechanism and associated ME-PBM will need to somehow slow down the consumption of precursor A.

Overall, the ME-PBM model built off the new three-step mechanism and including the experimentally determined nucleation mechanism is telling us that (i) yes, we have taken a step in the right direction with the three-step mechanism and using the experimental nucleation pathway in the code, but that (ii) we still do not have the "precisely correct" mechanism. That mechanism (iii) needs a way to move smaller particles to larger particles more quickly while also slowing the A loss and associated particle-growth steps somehow. These first two two- and three-step-based ME-PBM models strongly support our finding 18,19 that (iv) it is not trivial to find a ME-PBM model that will fit the observed PSD. That is, ME-PBM-attempted fittings of PSDs using MATLAB code developed for each hypothesized mechanism are an important, demanding test of one's proposed mechanism of particle formation.<sup>18,1</sup>

3.9. Exploration of a ME-PBM Model Built Off the New Three-Step Mechanism but with Added "Small—Small" Aggregation,  $B + B \rightarrow C$ . As the last ME-PBM examined as part of the present paper and initial ME-PBM studies, we explored the addition of a  $B + B \rightarrow C$ , small—small aggregation step, as one rational way to move small particles "B" along while also slowing down precursor A-loss by consuming B and, hence, kinetic competition with the A + B



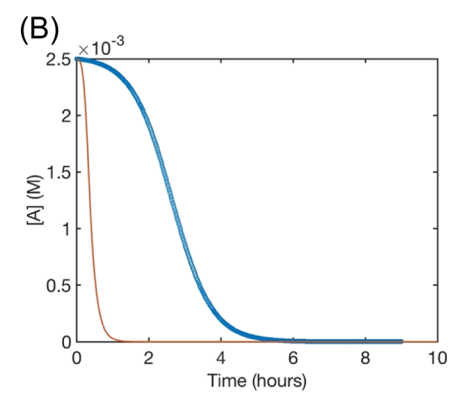


Figure 9. (A) Attempted fit to the end-time, 10.0 h histogram using ME-PBM built off of the two-step mechanism, but while also including the experimentally determined nucleation mechanism in the code so as to give the attempted fit the best chance of succeeding. No fit that is even close to the data is seen; the BFV<sup>18,19</sup> is also a relatively high 90.0 indicating a poor fit (lower BFVs indicate better agreement between the fit and the experimental data<sup>18,19</sup>). The resultant fit-determined rate constants (that refer to Scheme S1) are as follows:  $k_{\text{+Diss}} = 4.0 \times 10^{-1} \text{ h}^{-1} \text{ M}^{-2}$ ,  $k_{\text{-Diss}} = 3.7 \times 10^4 \text{ h}^{-1} \text{ M}^{-1}$ ,  $k_1 = 6.6 \times 10^{-1} \text{ h}^{-1}$ , and  $k_2 = 9.2 \times 10^3 \text{ h}^{-1} \text{ M}^{-1}$ , unreliable rate constants given the poor fit. The rate constants are provided here only because they are used to generate the predicted precursor loss curve discussed next. (B) Calculated precursor loss, [A]<sub>p</sub>, using the "best-fit" rate constants parameters from the above attempted fit to the PSD, are co-plotted with the experimental [A]<sub>t</sub> data from the global fitting of all [A]<sub>t</sub> loss data (see Figure S9 of the Supporting Information). The attempted fit to the PSD (left) and the attempted simulation of the CHCRR curve (right) are both totally inadequate. The clear implication is that, as before, <sup>18,19</sup> the two-step mechanism, while able to quantitatively account for all the kinetics data examined up to this point including all of the synchrotron X-ray based kinetics data, is insufficient to be able to account for the PSD.

→ C growth step of the three-step mechanism. Indeed, this next ME-PBM model, Scheme 4, shows how one can logically and systematically use the results from even failed ME-PBM models and their input mechanisms to rationally guide one toward a more "correct" mechanism able to account quantitatively for all of the available data, including the kinetics-information-rich PSD.

Scheme 4. Four-Step Mechanism Consisting of (i) Prior Equilibrium to Generate  $A_{solv}$ , (ii) Slow, Continuous Nucleation, (iii) Fast Small Particle Growth, (iv) Small Particle Agglomeration, and (v) Slow, Large Particle Growth

(PEq) 
$$A + 2 \text{ solv} \xrightarrow{k_{1}} A_{\text{solv}} + \text{HPO}_{4}^{2-}$$
  
(i)  $A_{\text{solv}} \xrightarrow{k_{1}} B + \text{HPO}_{4}^{2-}$   
(ii)  $A + B \xrightarrow{k_{2}} C + 2 \text{HPO}_{4}^{2-}$   
(iii)  $B + B \xrightarrow{k_{3}} C$   
(iv)  $A + C \xrightarrow{k_{4}} 1.5C + 2 \text{HPO}_{4}^{2-}$ 

While the PSD is better fit (as it should be with one additional rate constant fitting parameter) and while the predicted [A]-loss curve to the right in Figure 11 now shows some delay, the match to the experimental CHCRR kinetic curve is poor, indicating we still have more work to do to uncover the more detailed, even closer to the correct particle formation mechanism.

Several points are clear at this juncture: (i) ME-PBM analysis of the information buried in the PSD is critical to obtaining the more detailed, most reliable mechanism possible, and while getting closer (ii) we are not yet at that more detailed mechanism able to quantitatively account for all the kinetic and PSD data within experimental error. Hence, we have answered the question posed of: (iii) "can we fit the PSD and get the ostensibly correct mechanism in just three iterations of the ME-PBM (i.e., and given that the present,

second-generation system is for a relatively well-understood  $Ir(0)_n$  nanoparticle formation system close to the example where ME-PBM was first developed? 18,19)" The answer is "no", perhaps not surprisingly given that (iv) 11 known PEStep mechanisms were considered and ultimately disproved in our original ME-PBM on the first-generation, {(1,5-COD)Ir<sup>I</sup>· POM<sup>8-</sup> precursor to  $Ir(0)_n \cdot (POM^{9-})_x$  system en route to the new three-step mechanism discovered there via ME-PBM. 18,19 Additionally, (v) the dimeric nature of the secondgeneration,  $\{[(1,5\text{-COD})\text{Ir}^{\text{I}}\cdot\text{HPO}_4]_2\}^{2-}$  precursor introduces additional complexity into the ME-PBM analysis compared to the classic {(1,5-COD)Ir<sup>I</sup>·POM}<sup>8-</sup> precursor system. In particular, (vi) it is possible that an alternative nucleation mechanism is present, namely one involving the following dissociative equilibrium that can also account for the observed inverse (quadratic) dependence<sup>63</sup> on  $HPO_4^{2-}$ : {[(1,5-COD)-Ir<sup>1</sup>·HPO<sub>4</sub>]<sub>2</sub>}<sup>2-</sup> + 2 solvent  $\rightleftharpoons HPO_4^{2-}$  + [(1,5-COD)Ir<sup>1</sup>·HPO<sub>4</sub>}<sup>-</sup> + (1,5-COD)Ir<sup>1</sup>(solv)<sub>2</sub><sup>+</sup>, followed by precedented reduction of (1,5-COD)Ir<sup>1</sup>(solv)<sub>2</sub><sup>+</sup> by  $H_2$ .<sup>47</sup> That pathways would be expected to slow down the ME-PBM predicted [A]loss kinetic curve as is needed to fit the PSD as would the possibility that growth involves (1,5-COD)Ir<sup>I</sup>(solv)<sub>2</sub><sup>+</sup> or  $A(solv) = \{[(1,5-COD)Ir^{I}]_{2}HPO_{4}]\}^{0}$  rather than  $\{[(1,5-COD)Ir^{I}]_{2}HPO_{4}\}\}^{0}$ COD)Ir<sup>I</sup>·HPO<sub>4</sub>]<sub>2</sub>}<sup>2-</sup>. We (vii) will perform full Bayesian inversion statistical analysis as part of the needed additional ME-PBM studies. Those coding-time and computer-time intensive studies are in progress, will require their own substantial manuscript, and hence will be reported in due course.

3.10. Effects of Authentic tetra-Iridium-Hydride Cluster,  $Ir_4^lH_4(1,5\text{-COD})_4$ , on the Particle Formation Reaction: Does Addition of This Model of a Small, KEN<sup>61</sup> Accelerate the Particle formation Reaction? As we were writing up our studies, we realized that we were in a special position to be able to independently test if small,  $(Ir-H)_n$  clusters,  $n \le 4$ , could be kinetically competent intermediates for both the  $Ir(0)_n$  formation reaction as well as a CEN<sup>90</sup> for the indirect monitoring by the CHCRR?

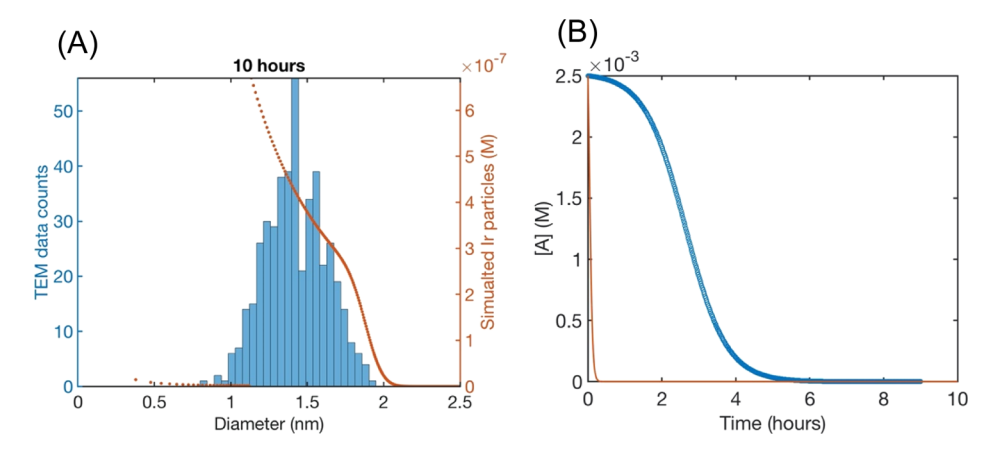


**Figure 10.** (A) Attempted fit to the end-time, 10.0 h histogram using ME-PBM encoded with the new three-step mechanism plus the experimentally supported nucleation mechanism so as to give the attempted fit the best chance of succeeding. The fit is decent on the right side of the PSD, but this particular ME-PBM does not properly capture particles ≤1.2 nm. The BFV<sup>18,19</sup> is 54.8. The resultant fit-determined rate constants (that refer to Scheme S2) are as follows:  $k_{+Diss} = 1.8 \times 10^{-1} \text{ h}^{-1} \text{ M}^{-2}$ ,  $k_{-Diss} = 1.2 \times 10^4 \text{ h}^{-1} \text{ M}^{-1}$ ,  $k_1 = 6.3 \text{ h}^{-1}$ ,  $k_2 = 6.1 \times 10^6 \text{ h}^{-1} \text{ M}^{-1}$ ,  $k_3 = 1.2 \times 10^4 \text{ h}^{-1} \text{ M}^{-1}$ , and M = 27. (B) Calculated precursor loss, [A]<sub>t</sub>, using the "best-fit" rate constants parameters from the above attempted fit to the PSD, is coplotted with the experimental [A]<sub>t</sub> data from the global fitting of all [A]<sub>t</sub> loss data (see Figure S9 of the Supporting Information).

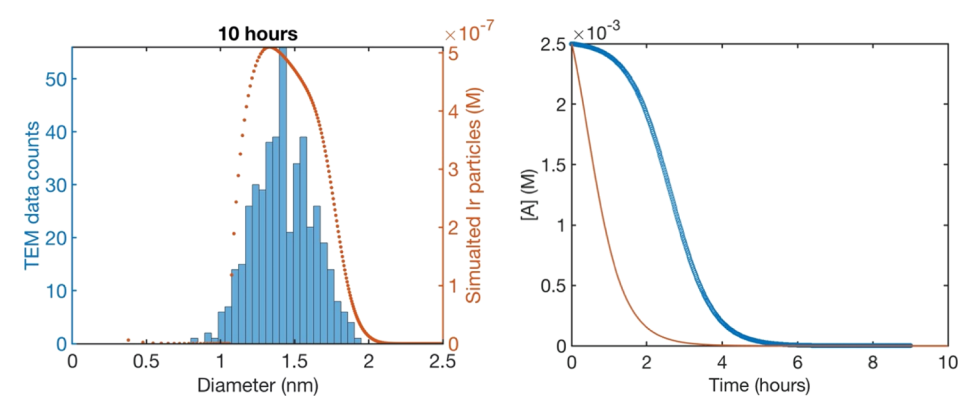


**Figure 11.** Attempted fit to the end-time, 10.0 h histogram using ME-PBM encoded with the new four-step mechanism plus the experimentally supported nucleation mechanism so as to give the attempted fit the best chance of succeeding. The general shape of the PSD is captured and the fit of the  $[A]_t$  curve is improved from either the fit using the two-step or three-step mechanisms. The BFV<sup>18,19</sup> is 25.4. The resultant fit-determined rate constants (refer to Scheme 4) are as follows:  $k_{+\text{Diss}} = 2.6 \times 10^{-1} \text{ h}^{-1} \text{ M}^{-2}$ ,  $k_{-\text{Diss}} = 2.2 \times 10^4 \text{ h}^{-1} \text{ M}^{-1}$ ,  $k_1 = 2.2 \text{ h}^{-1}$ ,  $k_2 = 5.4 \times 10^4 \text{ h}^{-1} \text{ M}^{-1}$ ,  $k_3 = 1.6 \times 10^6 \text{ h}^{-1} \text{ M}^{-1}$ ,  $k_4 = 1.0 \times 10^3 \text{ h}^{-1} \text{ M}^{-1}$ , and M = 23. (B) Calculated precursor loss,  $[A]_t$  using the "best-fit" rate constant parameters from the above attempted fit to the PSD, is coplotted with the experimental  $[A]_t$  data from the global fitting of all  $[A]_t$  loss data (see Figure S9 of the Supporting Information).

Highly relevant here is that we have excellent kinetics evidence for an iridium-hydride-based KEN<sup>61</sup> of  $\{Ir^{I}_{2}(H)_{2x}\cdot(HPO_{4})_{n}\}^{-2n}$  in the present system from our 2019 studies, <sup>63</sup> so that the discrete, tetra-iridium-hydride cluster,  $Ir^{I}_{4}H_{4}(1,5-COD)_{4}$  is just a dimer of that KEN (and once the 1,5-COD ligands are either replaced by added  $HPO_{4}^{2-}$  stabilizer or removed by hydrogenation, as shown back in eq 7). The novel tests reported below are uniquely possible for the present Ir-based nanoparticle system because we previously synthesized and unequivocally characterized <sup>50,51</sup> by crystallography (and five additional methods, NMR, IR, mass spectrometry, UV–vis, and XAFS<sup>50,51</sup>) the discrete, tetra-iridium-hydride cluster,  $Ir^{I}_{4}H_{4}(1,5-COD)_{4}$ , a rare, close model of potential early nucleation intermediates in a particle formation reaction.

We performed two sets of experiments, first with the  $\{[(1,5-COD)Ir^I\cdot HPO_4]_2\}^{2-}$  precursor system and then with a second precursor system, so as to test the generality of the results, specifically  $\{(1,5-COD)Ir^ICl\}_2$  (plus 3 molar equiv of  $(Bu_4N)^+Cl^-$  to slow the reaction kinetics into a measurable range). Each set of particle formation experiments was done to

start without, then with, 0.03 or 0.04 molar equiv (=1.5% or =2.0% in added Ir) of added authentic  $Ir^I_4H_4(1,S\text{-COD})_4$  for the cases of  $\{[(1,S\text{-COD})Ir^I\text{-HPO}_4]_2\}^{2-}$  and  $\{(1,S\text{-COD})Ir^I\text{-CI}\}_2$  (plus 3 molar equiv of  $(Bu_4N)^+\text{CI}^-$ ), respectively.

The results provided in Figure S6 show that even just 0.03 molar equiv (=1.5% in added Ir) of the reactive, discrete  $Ir_4H_4(1,5\text{-COD})_4$  cluster under  $H_2$  accelerated the observed  $k_1$  by ca. an order of magnitude in the case of the  $\{[(1,5\text{-COD})Ir^1\text{-HPO}_4]_2\}^{2-}$  precursor. The case of the  $\{(1,5\text{-COD})Ir^1\text{-CI}\}_2/3$  ( $Bu_4N$ )+Cl<sup>-</sup> precursor system proved even more interesting, the addition of the reactive, discrete  $Ir_4H_4(1,5\text{-COD})_4$  cluster under  $H_2$  shortens the reaction time from >120 h (ca. 5 days) to ~1 h, an acceleration of nucleation and growth by over  $10^2$ , Figure S6! The results strongly and independently support the hypothesis that small  $(Ir-H)_n$ ,  $n \le 4$  are both able KEN<sup>61</sup> as well able CEN<sup>90</sup> that can hydrogenate cyclohexene as required for the CHCRR to report with minimal delay on the  $Ir(0)_n$  particle formation process.

# 4. DISCUSSION

The following discussion is organized by returning to the seven specific questions posed in the Introduction.

Question #1: Will XANES and SAXS obtained kinetic data for the  $\{[(1,5\text{-COD})Ir^I\cdot HPO_4]_2\}^{2^-}$  precursor/ $Ir(0)_n\cdot (HPO_4^{2^-})_x$  nanoparticle system both be (i) sigmoidal as expected, and (ii) well-fit by the two-step mechanism as is found for the CHCRR and GLC-derived kinetics data?

All XANES and SAXS kinetic data revealed the expected, sigmoidal curves. All the kinetic data herein were reasonably fit by the minimal two-step mechanism as the recommended, well-precedented, <sup>45–52,54–80</sup> Ockham's razor obeying the starting point. Then, a good fit to an expanded, three-step mechanism was demonstrated for the key XANES and SAXS kinetic data

Question #2: What level of at least semiquantitative agreement is there between the rate constants obtained by CHCRR, GLC, XANES, and SAXS monitoring methods? What is the implied level of precision and, ideally, accuracy of the resultant rate constants?

The rate constants for the four monitoring methods are in agreement within a factor of ~2 for separate comparisons of  $k_{1\text{obs}}$  and  $k_{2\text{obs}}$  rate constants, Tables 1 and 2, vide supra. A global-fit to the composite kinetics data provided the global rate constants cited earlier of  $k_{1\text{obs,global}}$  avg =  $(1.5 \pm 0.1) \times 10^{-2}$  h<sup>-1</sup> and  $k_{2\text{obs,global}}$  avg =  $(2.4 \pm 0.1) \times 10^{2}$  h<sup>-1</sup> M<sup>-1</sup> of respective  $\pm 7$  and  $\pm 4\%$  estimated precisions. Given that these estimates cover the four different methods used to monitor the reaction, these global averages are our best estimates and current working hypothesis of ostensibly accurate rate constants for nucleation and autocatalytic surface growth in the second-generation system. What is perhaps noteworthy is the amount of time and effort it has taken to achieve these just two rate constants at the desired level of precision and, perhaps, also accuracy.

Question #3, part I: When looking in more detail at the now well-established, prototype  $Ir^{I}(1,5\text{-COD})^{+}$ -containing precursor systems,  $^{45-47,51,52,54-63,87-93}$  what are the known, primary sources of experimental error in measuring accurate nucleation and growth rate constants?

Effects of Common Dust on the Classic {(1,5-COD)Ir<sup>I</sup>· POM}<sup>8-</sup> Precursor and  $Ir(0)_n \cdot (POM^{9-})_x$  Nanoparticle System. There is little doubt that the presence of common room dust in solvents, on glassware and in reactors is a main source of approaching an order-of-magnitude error in nucleation rate measurements and hence rate constants. 62,63 In prior work on the first-generation {(1,5-COD)Ir<sup>I</sup>·POM}<sup>8-</sup> precursor and  $Ir(0)_n \cdot (POM^{9-})_x$  nanoparticle system,<sup>62</sup> by using 0.20  $\mu$ m microfiltered solvent (and then also washing the F-P bottle reactor and any glassware used with that filtered solvent to lower the dust content) the  $k_{1\text{obs(bimolecular)}}$  in that work was lowered by up to  $\sim$ 7.6-fold.<sup>62</sup> Interestingly, the absolute error seemed to remain constant as judged by the relative error in  $k_{
m lobs(bimolecular)}$  being  $\pm 47\%$  and hence larger compared to the smaller, ±27% relative error in the up to 7.6-fold faster  $k_{\text{lobs(bimolecular)}}$  for the unfiltered solutions. 62 The  $k_{\text{2(obs)}}$  rate constants were not changed within experimental error and serve as an "internal standard" of sorts arguing for the reliability of the results. Remarkably, the  $Ir(0)_n$  PSD narrowed by a factor of 2.4 with the microfiltration treatment, from  $\pm 19\%$  to a rather narrow  $\pm 8\%$ , 62 not far off of the record minimum ~5% PSD from any nanoparticle self-assembly reaction as documented elsewhere. 62 The 2.4-fold narrowing of the PSD could be accounted for by a slowed nucleation rate constant,  $k_{1\text{obs}}$ , along with an unchanged autocatalytic growth rate constant,  $k_{2\text{obs}}$ , and with a KEN that includes dust,  $Ir_3H_\nu(POM)_1$ ·dust.

Effects of Microfiltration on the Current  $\{[(1,5\text{-COD})Ir^I\text{-}HPO_4]_2\}^{2^-}$  Precursor and  $Ir(0)_n$ .  $(HPO_4^{2^-})_x$  Nanoparticle Product System. We have also examined the effects of incorporating the microfiltration protocol on the  $Ir(0)_n$ .  $(HPO_4^{2^-})_x$  nanoparticle system,  $^{63}$  with similar results to those described above. Specifically, the expected slowing of  $k_{1\text{obs}}$  with  $0.2~\mu\text{m}$  filtration is seen, albeit at a somewhat lower,  $\sim 1.5-5$ -fold level in the  $\{[(1,5\text{-COD})Ir^I\text{-}HPO_4]_2\}^{2^-}$  precursor system of reduction in  $k_{1\text{obs}}$  for the  $\{[(COD)Ir^I\text{-}HPO_4]_2\}^{2^-}$  system. Hence, the KEN in this system also includes dust,  $Ir_2H_x(HPO_4)_1$ ·dust. The studies reported herein by design include the presence of room dust (as discussed in greater detail in the Supporting Information) as room dust is present in probably >99% of all reported particle syntheses.

Literature Revealing Analogous Effects of Dust Removal by Microfiltration on Particle Formation Reactions. Interestingly, both of the effects of an increase in the relative error (in the J rate, 94 vide infra) and a narrowing of the PSD have been observed before when using microfiltration as part of the experimental protocol in a study by Kulkarni and coworkers examining the crystallization of isonicotinamide.<sup>94</sup> Although the high-precision particle formation, J, rates were not adequately deconvoluted into separate nucleation and growth rate constants in this otherwise state-of-the-art study (discussed a bit more in the Supporting Information for the interested reader), the authors do report that the  $\pm 5\%$  error bars in the their J rates for the filtered solutions from 144 measurements<sup>94</sup> are reduced 3.6-fold to  $\pm 1.4\%$  in the unfiltered solution, results that once again imply a relatively constant, absolute error source in the kinetic measurements. The effects of microfiltration were attributed to room dust by the authors although, direct evidence for dust, the size or type of the dust (i.e., "inorganic" and/or "organic" 62), and hence compelling evidence for its removal by the filtration step, was not provided.

Also meriting mention is a seminal 1963 paper from Matijevic and co-workers <sup>119</sup> studying the PSD of sulfur (S)<sub>n</sub> sols reports that careful attention to the purity of the starting reagents, the water solvent, efficient mixing, temperature control, and the removal of dust by use of a 0.22  $\mu$ m microfilter is required to achieve a reproducible synthesis. Significantly, that careful experimental work narrowed the final size distribution 2-fold for 95% of the observed particles to 0.48  $\pm$  0.04  $\mu$ m (i.e.,  $\pm$ 8%)<sup>119</sup> from that seen of 0.51  $\pm$  0.08  $\mu$ m (i.e.,  $\pm$ 16%) in an earlier, <sup>120</sup> ostensibly closely analogous synthesis. <sup>119</sup> Intriguing is that the 2-fold narrowing in the (S)<sub>n</sub> system is nearly identical to the 2.4-fold narrowing we see for the Ir(0)<sub>n</sub>·(POM<sup>9-</sup>)<sub>x</sub> nanoparticle system when using the microfiltration treatment of the solvent and rinsing the reactor and glassware surfaces with the microfiltered solvent.

The take home message is clear: dust is an omnipresent, kinetically important component of the nucleation process and the resultant particle-size and PSD. Nucleation is, indeed "almost always heterogeneous" (see p 542 of the proceedings of a 2015 workshop of experts on nucleation<sup>121</sup>). Relevant here is that common room dust has been known since the 1880s to be critical in vapor-phase nucleation and particle formation processes, <sup>122–128</sup> yet to this day the effects of dust are not considered in most particle formation reactions one finds in

the literature. Until and unless the effects of omnipresent dust are taken into account, valuable synchrotron radiation and research time are arguably being largely wasted in studies claiming to examine nucleation but that have not examined the effects of omnipresent dust.

Other Factors Affecting Nucleation and Growth in the Prototype  $Ir(0)_n$  Nanoparticle Systems. The other, often adventitious factors that we have found that influence the nucleation and growth of nanoparticles (i.e., factors other than the common, known ones of ligands, temperature, solvent, and so on) include the following, a growing list since 1994 studies that document such effects: acetone solvent impurities, water,  $^{46}$  O<sub>2</sub>,  $^{46}$  H<sup>+</sup>,  $^{46}$  trace residual solvents such as EtOAc 129 used in syntheses, dust,  $^{62,63}$  and additives such as the diprotonated (Bu<sub>3</sub>NH)<sub>2</sub>(H<sub>2</sub>P<sub>2</sub>O<sub>7</sub>).  $^{63}$ 

In summary, the Ir<sup>I</sup>(1,5-COD)<sup>+</sup>-based first- and secondgeneration systems provide well-studied systems that others can refer to about experimentally established factors that affect nucleation and growth rate constants. The above factors and the dominance of heterogeneous nucleation <sup>121,130</sup> over true homogeneous nucleation are among the reasons nucleation rate constants in particular are notoriously hard to measure reproducibly, precisely, and accurately.

Question #3, part II: What more generally are the error bars on the nucleation and growth rate constants and how do those error bars compare to the most precise nucleation and growth kinetics in the literature? 94,95

Historically, agreement of specifically nucleation rates and rate constants within  $\pm 10^{1-2}$  have been considered to be<sup>62,130</sup> "of great success". That said, a good place to start en route to answering the above question more globally is the firstgeneration  $\{(1,5\text{-COD})\text{Ir}^{\text{I}}\cdot\text{POM}\}^{8-}$  precursor and  $\text{Ir}(0)_{\sim300}\cdot$  $(POM^{9-})_x$  product system. 95 From over ~1500 kinetic runs to date using the CHCRR methodology by 11 researchers from studies that began before 1997,52 the interinvestigator and intrainvestigator error bars on the  $k_{1\text{obs}}$  and  $k_{2\text{obs}}$  for the twostep mechanism are  $k_1 \pm 10^{1.2}$  (i.e.,  $\pm 15.9$ -fold)<sup>95</sup> inter- and  $\pm 50\%$  intrainvestigator, and  $k_2 \pm 50\%$  inter- and  $\pm 15\%$ intrainvestigator, respectively. Even with great efforts to eliminate sources of experimental variability (specifically those discussed in the first part of this question #3) and to reduce the error via 17 repeat experiments, 61 a singleinvestigator error of 21% was attainable after 17 repeat experiments focused on nucleation, a second-order rate constant  $k_{\text{lobs(bimolecular)}} = 6.1 \pm 1.3 \text{ h}^{-1} \text{ M}^{-1}$  in that particular study.6

For the second-generation  $\{[(1,5\text{-COD})\text{Ir}^{\text{I}}\cdot\text{HPO}_4]_2\}^{2-}$  precursor and  $\{\text{Ir}(0)_{\sim 150}\cdot(\text{HPO}_4)_x\}^{-2x}$  product system studied in the present work, the interinvestigator error among three primary researchers (over the  $\geq 7$  years since this study began in earnest prior to 2013 and among all the physical methods and synchrotron or in-house locations employed) is the  $\sim 2$ -fold variation in the individual  $k_{1\text{obs}}$  and  $k_{2\text{obs}}$  detailed back in Tables 1 and 2. However, as detailed earlier, if one combines all the 1178 total kinetic data points underlying Tables 1 and 2 and then fits that composite data set, global-average estimates of  $k_{1\text{obs},\text{global}}$  and  $k_{2\text{obs},\text{global}}$  and

In summary, reproducible nucleation and growth rate constants of precision ≤10% are possible with sufficient experimental care and a sufficiently large amount of raw data from a sufficiently high number of repeat experiments plus some assumptions in treating the data. Accurate rate constants are another matter, requiring a suitable range of ideally complimentary physical methods according to all our evidence or knowledge of the literature.

Question #4: Are synchrotron-based methods alone, specifically XANES and SAXS, sufficient for the present example to obtain the ostensibly "correct" mechanism according to all the available data? An underlying, broader question—one only fully addressable by the communities involved—is if synchrotron XANES and SAXS direct methods are pretty much fool-proof, or do these generally powerful methods also have limitations that merit additional investigation?

For the present system, not even the generally powerful, fairly direct methods of XANES and SAXS were sufficient to reveal the true underlying mechanism. ME-PBM analysis of the PSD versus time data was also required to get closer to the "correct" mechanism, again at least for the present example.

Additionally, synchrotron X-ray based methods do not appear to be absolutely fool-proof due to possibility of wellprecedented, 104-108 but underappreciated and underdiscussed, X-ray-induced radiolysis of solvent or other molecules (even the highly endoergic process  $Zn^{2+} \rightarrow Zn^{3+} + e^{-})^{104}$  as a source of e- and, hence, possible artifacts, especially in the sensitive nucleation step. In the present example, nucleation is expected to be triggered by solvated e reduction of Ir(I) to produce Ir(0), "B" in the present case, B that then grows autocatalytically, which means exponentially. The exponential magnification of the [A]-loss curve post any nucleation is why even trace nucleation due to solvated e- needs to be considered in our opinion in any and all studies employing the otherwise powerful synchrotron X-ray radiation-based methods, where autocatalytic growth can then follow in that system. However, further studies of multiple systems by the broader community are needed to support, or refute, the working hypothesis of possible X-ray radiolysis in especially the nucleation step(s) of particle formation being monitored by synchrotron X-ray radiation methods.

Question #5: Does the application of ME-PBM to the TEMdetermined PSDs support or refute the best fitting mechanism? Is our recent conclusion, that ME-PBM is likely to become a "must use" tool<sup>18,19</sup> prior to publishing any particle formation mechanism, supported<sup>18,19</sup> or refuted?

ME-PBM proved powerful and, overall, essential as before,  $^{18,19,92}$  at least for the two  $Ir(0)_n$  nanoparticle systems examined to date. As already noted, quantitative fitting of the XANES, SAXS, CHCRR, and GLC-based kinetics proved possible, but did not by themselves lead to a final mechanism able to account quantitatively for all the data, including the PSD and [A]-loss kinetics. Overall, the results herein like those before  $^{18,19,92}$  argue strongly that ME-PBM is very likely a "must use" tool  $^{18,19}$  before a reliable particle formation mechanism can be claimed to be in-hand.

Question #6: What, then, is (are) deemed to be "best" physical method(s) for monitoring especially the notoriously hard to measure nucleation step(s) $^{61}$  and to obtain accurate rate constants, at least for the present  $Ir(0)_n \cdot (HPO_4^{2-})_x$  nanoparticle system? What are the strengths and weaknesses of each method in at least our hands, and how can they be used in a complimentary fashion? What roles do indirect, but in-house and hence convenient, methods

such as the CHCRR have in comparison to the XANES and SAXS monitoring methods?

Synchrotron XAFS and SAXS. Based on the extensive use of synchrotron XAFS and SAXS to monitor particle formation reactions in the literature <sup>131</sup> as well as our own studies herein, there is little doubt that the relatively direct methods of XAFS and SAXS will continue to be forefront methods for monitoring particle formation reactions. That said, XANES is somewhat limited by both the precision and amount of data (as seen back in Figure 3) and SAXS is limited by the weaker scattering by smaller compared to larger particles. Both methods suffer in principle from possible X-ray radiation induced radiolysis 104-108 and, hence, the little tested effects of that radiolysis on nucleation and growth in all but a few important papers and systems. 104-108 The synchrotron methods do not provide large amounts of high-precision kinetic data, nor are they "infinitely available" to any investigator. The latter is probably one reason that very basic studies such as measuring even the rate law for the particle formation process, or the effects of dust on nucleation, are largely nonexistent in the broader XAFS and SAXS literature examining particle formations, at least presently. In this regard, machine learning-assisted analysis of XANES data<sup>13</sup> merits mention as a recently discovered way to improve the sensitivity of XANES, even for harsh conditions of low metal loadings, high temperatures, and the presence of reactor walls that complicate the use of the workhorse method for nanoparticle studies, EXAFS. 137-139 The advance of machine learning-assisted analysis of XANES has recently been successfully applied to analyze the formation of metal nanoparticles under in situ conditions in ionic liquids 140,141 and ionic salt melts. 104

In-House, Direct and Indirect Methods. Over the years, we have examined NMR, UV-visible, GLC, CHCRR, and TEM as in-house methods<sup>45-63</sup> to monitor the loss of precursor (NMR, UV-vis), COA reaction byproduct formation (GLC) or particle formation (CHCRR and TEM). Only the CHCRR is in situ (actually in operando) due to the issue of H<sub>2</sub> gas also being a reactant so that the other methods require the removal and examination of reaction aliquots. Only NMR and, arguably, TEM are more direct, TEM bordering on being a "more direct" method due to multiple controls performed when we first used TEM in 1994. Those key early controls demonstrate that third-row-metal  $Ir(0)_n$  nanoparticles have high stability in the TEM beam, one of the multiple advantages of the  $\{(1,5\text{-COD})\text{Ir}^{\text{I}}\cdot\text{POM}\}^{8-}$  and  $\{[(1,5\text{-COD})\text{Ir}^{\text{I}}\cdot\text{POM}\}^{8-}\}$ HPO<sub>4</sub>]<sub>2</sub>}<sup>2-</sup> precursor systems detailed in the Supporting Information and one reason we picked  $Ir(0)_n$  (and not  $Rh(0)_n$  or  $Au(0)_n$ , e.g.) for emphasis >25 years ago. <sup>45,46</sup> Only the CHCRR gives continuous kinetic data and anything like >1500 data points of intrinsic ±0.01 psig precision and ~±0.5% precision as applied herein, the other aliquot-based methods giving ≤10 time-resolved data points of ~5-15% precision.

As nature would have it, the CHCRR monitoring method that is by far the most convenient, the most precise data generating, as well as a continuous monitoring method is also the most indirect. The CHCRR kinetic method relies on the facile hydrogenation of cyclohexene, under experimental conditions where controls demonstrate the required zero-order dependence on cyclohexene  $^{52}$  (i.e., so that it is not rate limiting in any way), by any and all the Ir-species from the  ${\rm Ir}^1_2({\rm H})_{2x}\cdot({\rm HPO_4})_n^{-2n}$  KEN forward, including  ${\rm Ir}(0)_n$ . The

choice of the so-called "structure-insensitive" 142 reaction of hydrogenation, which shows a minimal, often  $\leq$  ca. 3-fold dependence on particle size, <sup>142</sup> is an important, deliberate part of the design of the CHCRR. <sup>45,46,52</sup> The size  $Ir(0)_n$  present by the end of the induction period is estimable by both TEM and GLC of aliquots taken before and after the induction period and has been defined as the Catalytically Effective Nucleus (CEN). The CEN was determined to start at Ir<sub>2</sub>, be highly active at Ir<sub>4</sub> as modeled by a discrete Ir<sub>4</sub>H<sub>4</sub>(ligand)<sub>4</sub> cluster added to the reaction, and overall  $\text{Ir}_{\leq 26}$  by the end of the observed induction period. The understanding and careful use of the PEStep method back in Scheme 1 and eqs 1-7 underlie the CHCRR as do critical controls done at the start<sup>52</sup> (and repeated for each new system<sup>57-60,63</sup>) showing that GLC monitoring yields the same kinetics and  $k_{1\text{obs}}$  and  $k_{2\text{obs}}$  rate constants within experimental error. Typically, only the first 1/ 3 to 1/2 of the CHCRR data are used to ensure the zero-order in [cyclohexene] conditions needed for the CHCRR. Earlier papers contain additional details and discussions about the use of and approximations underlying the CHCRR. 52,54,56-63

An issue since simulations done back in 2001<sup>54</sup> has been that the formation of even a  $\mbox{Ir}_{\sim 13} \mbox{ CEN}^{90}$  could lengthen the induction period (and thereby slow the apparent kinetics of the CHCRR) by as much as a factor of 54 10 (a derivation plus discussion of how the formation of a CEN can influence the CHCRR kinetics is provided in the Supporting Information). However, compelling evidence small even Ir<sub>2-3</sub> KEN can both hydrogenate additional Ir<sup>I</sup>(1,5-COD)<sup>+</sup> (via surface autocatalytic growth) as well as hydrogenate cyclohexene in the CHCRR is now strongly supported by six lines of evidence: (i) the agreement within a factor of  $\sim$ 2 of the  $k_{1\text{obs}}$  and  $k_{2\text{obs}}$  rate constants from the four kinetic methods back in Tables 1 and 2; (ii) the demonstration that the authentic, tetra-iridiumhydride cluster, Ir<sub>4</sub><sup>I</sup>H<sub>4</sub>(1,5-COD)<sub>4</sub>, is able to both nucleate  $Ir(0)_n$  particle formation as well as support the CHCRR; and (iii) that nothing even close to a factor of 10 that simulations indicate is possible for a putative Ir<sub>13</sub> CEN is seen in Figures 3 or 5—at most a factor of ~2 in Figure 3b, for example. Previous evidence that the CHCRR methodology was working largely as believed includes (iv) the GLC controls yielding roughly equivalent kinetics; 52 (v) the ability to determine nucleation kinetics via the CHCRR that yielded small, Ir<sub>2-3</sub> KENs<sup>47,63</sup> —something inconsistent with having to reach a CEN of Ir<sub>~26</sub> before the CHCRR started "reporting" on the particle formation process; and that (vi) the CHCRR experimentally derived nucleation rate law and mechanism are at least generally supported by the ME-PBM—indeed are a required component of any ME-PBM able to fit the PSD data. 18,19 The amplification of the signal (i.e., the amount of Ir product) by the CHCRR catalysis is another, valuable part of the CHCRR method. In short, six lines of evidence strongly support the conclusion that the CHCRR is a valuable in-house tool for monitoring  $Ir(0)_n$  and other  $metal(0)_m$  nanoparticle formation reactions. 45-63

Complimentary Nature of the Direct and Indirect Methods. The above discussion of the XANES, SAXS, GLC (or NMR, UV—vis, etc), and CHCRR methods makes apparent that each method has its strengths and weaknesses. Also apparent is that the more physical methods—and especially the more complimentary the multiple physical methods employed—the better. SAXS is especially valuable as a relatively direct method<sup>131</sup> ("relatively", due to possibility of radiolysis <sup>104–108</sup> effects) if one can also obtain the number of particles versus

time along with precursor conversion via standard radius versus time data—Karim's point that SAXS, then, counts as "two methods".<sup>32</sup>

However, in-house methods can be invaluable for scouting out experimental conditions for more direct, but less-accessible and more-expensive, methods such as trips to a synchrotron radiation source. The CHCRR is a case in point: over 1500 kinetic runs with 11 independent researchers over a 26 year period since 45,46 1994 and accelerating after 52 1997 have been performed with the CHCRR. Even for just the secondgeneration  $\{[(1,5\text{-COD})\text{Ir}^{\text{I}}\cdot\text{HPO}_4]_2\}^{2-}$  precursor system, the CHCRR and GLC methods have allowed one of us (CBW) to collect ~70 datasets per year over 3 years for a total of ~210 experimental datasets under a range of conditions. Without the CHCRR, we would not have the minimum mechanisms in Scheme 2<sup>46-52,55-63</sup> nor any nucleation mechanisms<sup>47,63</sup> as working hypotheses for going forward, nor the paradigm shifting low molecularity, KENs of  $^{47,63}$  Ir<sub>2-3</sub>, nor the development of ME-PBM,  $^{18,19}$  nor the important "smaller" particles grow faster than larger particles" insight. The total number of nanoparticle formation kinetic experiments we have performed using the CHCRR exceeds by nearly 2 orders of magnitude the number of synchrotron trips and associated kinetic studies (3 total) that at least we have been able to perform during the same time frame of this research. That said, access to synchrotron XANES and SAXS methods has been absolutely crucial to checking the fidelity of the CHCRR and other in-house methods and results.

Question #7. Finally, what additional studies are recommended going forward en route toward an even more detailed understanding of particle formation nucleation, growth, and agglomeration across nature?

The literature that at least we have assembled seems 100% clear on this point: <sup>64,65,93,131,143</sup> (i) more experimental studies of especially nucleation by multiple, complimentary physical methods, especially efforts to obtain experimental rate laws for nucleation of a variety of precursor systems and, hence, the KEN<sup>47,61,63</sup> for each system under consideration; (ii) the use of SAXS<sup>131</sup> while getting both radius data and the number of particles versus time<sup>32</sup> along with any controls possible to test for the effects of X-ray induced radiolysis; 104-108 and (iii) expansion of and testing all proposed mechanisms by ME-PBM to see if the information-rich PSD supports or refutes the proposed particle formation mechanism. (iv) The combination of SAXS PSD data vs time with ME-PBM analyses constructed stepwise and separately from each and every reasonable alternative mechanism(s) is expected to prove especially powerful. Depending on what other, in-house particle formation kinetics or, for example, TEM product versus time data are available, it may actually prove most efficient to perform initial ME-PBM before going to the synchrotron in order to help plan and optimize the more expensive, lessroutine SAXS experiments. (v) XANES studies to have a separate look at the early, nucleation part of the kinetics and to check the SAXS results should continue to prove useful, especially when employing recently developed machine learning methods for nanoparticle structure characterization based on the XANES data. All the above should also (vi) follow Karim's urgings<sup>9,32,39</sup> to vary conditions as widely as possible, especially concentrations and the temperature, temperature-dependent kinetic studies of particle formation reactions being relatively rare to date. Additionally recommended to more rapidly advance particle formation science are

(vii) careful consideration of heterogeneous nucleation 121,130 and the role of impurities such as common room dust 62,63,92,122-128 in nucleation and growth studies of particle formation; and (viii) moving beyond—ultimately discarding classical nucleation theory (CNT) for most systems. CNT simply does not work for, nor was it intended to be used for, strongly bonding systems, 65 where the monomer loses its identity in the nucleus in what is a kinetic process such as n M  $\rightarrow$  (M)<sub>n</sub> (M = metals, e.g.) and not a reversible, thermodynamically controlled process as CNT posits. 65 This is why CNT works best for gas-phase systems aggregating with weak forces such as  $nRH \iff (RH)_n$ , the classic case where CNT does makes sense and can be applied.<sup>65</sup> Additionally, recommended is (ix) moving beyond—basically abandoning the 70 year-old LaMer model of particle formation of putative "instantaneous/burst nucleation" and "diffusion-controlled growth", a mathematical model that has zero compelling support in nearly 2000 papers over 70 years as detailed in two, 2019 and 2021 reviews; <sup>64,65</sup> (x) moving beyond—effectively discarding—old, controversial, semiempirical, nonmechanistic models for phase changes such as Avrami-based models for phase changes that do not treat nucleation in any physically real, reliable way, and that yield nonphysical, convoluted parameters, the interpretation of which continue to confuse even experts that rely on those outdated models; <sup>143</sup> and (xi) use of the available minimum, disproof-based mechanistic models for particle formation summarized in a table in a recent review<sup>131</sup> —including following Karim's lead using minimum mechanisms that explicitly deal with added ligand, L, effects. 9,32,39 Additional recommendations are (xii) the use of a time-tested, superior disproof-based 15-17 approach to the science, including use of the five classes of ≥96 distinct particle formation mechanisms now available elsewhere 131 that include ligand effects; 9,32,39 (xiii) applying those minimum mechanisms and their associated mechanism-based differential equations to the results of expert-obtained XAFS and SAXS kinetic data, rather than just presenting pictorial, schematic ("cartoon") representations and restatements of, often, the particle sizes versus time that are just a pictorial restatement of the raw data; 131 (xiv) emphasis on the minimum requirements of a reliable, minimum reaction mechanism of a balanced reaction stoichiometry plus kinetics as the first two of four key criteria to a reliable mechanism; 64 (xv) consideration of and overlap with mechanisms of particle formation in the wellstudied area of protein aggregation involving nucleation, growth, and agglomeration processes; 76 and (xvi) greater reliance on modern methods of computation and theory (and not CNT) to better understand nucleation 144,145

We realize the above list is written from our personal, hence by definition biased, perspective. It is nevertheless our perspective based on, now, over a quarter century of effort including several older and more recent key contributions <sup>18,19,47,52,61–65,93,131,143</sup> striving to achieve a firmer, kinetics-, mechanism-, and ME-PBM-based understanding of particle formation kinetics and mechanisms across nature.

## 5. CONCLUSIONS

Herein, we have examined seven questions via the second-generation,  $\{[(1,5\text{-COD})\text{Ir}^{\text{I}}\cdot\text{HPO}_4]_2\}^{2-}$  precursor to  $\text{Ir}(0)_{\sim 150}\cdot(\text{HPO}_4^{2-})_x$  nanoparticle system. The reported studies achieve our goal of checking the kinetics and mechanism of  $\text{Ir}(0)_n$  particle formation by more direct, synchrotron-based methods. Disproof-based experimentation that utilized a series of five

experimental techniques (CHCRR, GLC, XAFS, SAXS, and TEM) plus ME-PBM revealed that  $Ir(0)_{\sim 150} \cdot (HPO_4^{2-})_x$ nanoparticle formation kinetics are sigmoidal by all methods examined. The observed kinetics from each physical method can be described quantitatively by a minimal two-step mechanism of slow, continuous nucleation (A  $\rightarrow$  B,  $k_{1obs}$ ) followed by autocatalytic surface growth (A + B  $\rightarrow$  2B,  $k_{2obs}$ ). The resultant  $k_{1\text{obs}}$  and  $k_{2\text{obs}}$  rate constants for all methods under XANES conditions were found to fall within a range of average values and error limits of ~2-fold. A global-average fitting of all of the data yielded  $k_{1\text{obs,global avg}} = (1.5 \pm 0.1) \times 10^{-2} \text{ h}^{-1}$  and  $k_{2\text{obs,global avg}} = (2.4 \pm 0.1) \times 10^{2} \text{ h}^{-1} \text{ M}^{-1}$  of respective ±7 and ±4 estimated precisions. A comparison of the sigmoidal curve corresponding to the global fit, Figure S9 in the Supporting Information, reveals that the separate XANES and SAXS kinetic curves are closest to and hence most representative of (actually spanning) the global average kinetic curve. However, ME-PBM was also required as before 18,19 to extract mechanistic information from the information-rich PSD and as a check of the proposed particle formation mechanism.

The results were then used to go back and answer the seven questions raised in the Introduction. The seventh and final question of "what additional studies are recommended going forward en route towards an even more detailed understanding of particle formation nucleation, growth, and agglomeration across nature?" was answered with a list of 16 recommendations. The 16 recommendations draw heavily from our recent reviews<sup>64,65,93,131</sup> and a Response to a Comment, 143 hence are unavoidably infused with our opinions and any accumulated biases. However, in this final experimental paper from us examining the instructive  $Ir(0)_n$  nanoparticle formation systems, our recommendations are offered with the hope that they will stimulate the reader's own critical thinking, improved experiments, improved experimental design, and then critical, disproof-based analysis and interpretation of the resultant data for particle formations across nature. We offer our best wishes to each and every one of those endeavors!

# ASSOCIATED CONTENT

# Supporting Information

The Supporting Information is available free of charge at https://pubs.acs.org/doi/10.1021/acs.jpcc.1c03475.

CHCRR methodology and PEStep treatment of CHCRR kinetics; EXAFS analysis of end-time, product  $Ir(0)_n$  nanoparticles; temperature re-equilibration and acetone solvent plus cyclohexene vapor-pressure correction; SAXS cell construction; SAXS data processing; methods employed for measuring  $k_{2,\text{surface}}$  versus  $k_{2,\text{Total}}$  $(=k_{2.\text{Volume}})$  plus the ME-PBM report; control experiments for examining authentic, crystallographically characterized Ir<sup>1</sup><sub>4</sub>H<sub>2</sub>(1,5-COD)<sub>4</sub> plus HPO<sub>4</sub><sup>2-</sup>; fitting the XANES-type CHCRR tandem data with a constrained  $k_{2\text{obs}}$  rate constant; composite, global fitting of all the data; TEM-determined average diameter versus time under XANES conditions; consideration and analysis of a CEN of  $B_n$ , with  $n \le 26$ ; a comparison with the results of our 2001 numerical integration simulations; ME-PBM and the specific mechanistic models and associated ODEs; five advantages of the {(1,5-COD)Ir<sup>I</sup>·POM}<sup>8-</sup> nanoparticle formation system; seven advantages of the second-generation  $\{[(1,5-$ COD)Ir<sup>I</sup>·HPO<sub>4</sub>]<sub>2</sub>}<sup>2-</sup> nanoparticle precursor system;

limiting explanations for the quantitative differences in the  $k_{1\text{obs}}$  and  $k_{2\text{obs}}$  values; additional discussion of why dust was deliberately not removed as part of the present studies; and discussion of the state-of-the-art, high-precision particle formation, J, rates in Kulkarni and coworkers' study examining the crystallization of isonicotinamide (PDF)

## AUTHOR INFORMATION

### **Corresponding Author**

Richard G. Finke — Department of Chemistry, Colorado State University, Fort Collins, Colorado 80523, United States; orcid.org/0000-0002-3668-7903; Email: Richard.Finke@colostate.edu

#### **Authors**

Christopher B. Whitehead – Department of Chemistry, Colorado State University, Fort Collins, Colorado 80523, United States

Derek R. Handwerk — Department of Mathematics, Colorado State University, Fort Collins, Colorado 80523, United States; © orcid.org/0000-0003-4614-9954

Patrick D. Shipman – Department of Mathematics, Colorado State University, Fort Collins, Colorado 80523, United States; © orcid.org/0000-0003-4741-9370

Yuanyuan Li — Department of Materials Science and Chemical Engineering, Stony Brook University, Stony Brook, New York 11794, United States; orcid.org/0000-0003-3074-9672

Anatoly I. Frenkel — Department of Materials Science and Chemical Engineering, Stony Brook University, Stony Brook, New York 11794, United States; Division of Chemistry, Brookhaven National Laboratory, Upton, New York 11973, United States; orcid.org/0000-0002-5451-1207

Bridget Ingham – Callaghan Innovation, Lower Hutt 5040, New Zealand

Nigel M. Kirby – Australian Synchrotron, Clayton 3168, Australia

Complete contact information is available at: https://pubs.acs.org/10.1021/acs.jpcc.1c03475

#### Notes

The authors declare no competing financial interest.

# ACKNOWLEDGMENTS

We greatly appreciate and acknowledge Patrick Kent for his contributions beginning before 2014. We further thank Patrick for providing us with his XANES work as cited herein, so this long-term effort could finally be published without further delay. We offer our heartfelt condolences to Patrick on the tragic passing of his wife due to cancer in the otherwise prime of her and his lives. Professor Murielle Watzky's always careful and thoughtful comments on the manuscript and proofreading help are a pleasure to acknowledge as are the thoughtful, helpful comments from two referees. The Stanford Synchrotron Radiation Lightsource and Australian Synchrotron are thanked and acknowledged for providing access to conduct synchrotron XAFS and SAXS, respectively. Use of the Stanford Synchrotron Radiation Lightsource, SLAC National Accelerator Laboratory, is supported by the U.S. Department of Energy, Office of Science, Office of Basic Sciences under Contract no. DE-AC-02-76SF00515. Operations at the beamlines BL2-2 of the National Synchrotron Light Source-I were

supported in part by the Synchrotron Catalysis Consortium (U.S. DOE, Office of Basic Energy Sciences, grant no. DE-SC0012335). XAS analysis work of A.I.F. was supported in part by the Catalysis Center for Energy Innovation, an Energy Frontier Research Center funded by the U.S. Department of Energy, Office of Science, Office of Basic Energy Sciences under Award no. DESC0001004. The SAXS portion of this research was undertaken on the SAXS/WAXS beamline at the Australian Synchrotron, part of ANSTO. The work at Colorado State University was supported by the U.S. Department of Energy, Office of Science, Basic Energy Sciences, Catalysis Science Program, via Award SE-FG402-02ER15453.

## REFERENCES

- (1) Astruc, D.; Lu, F.; Aranzaes, J. R. Nanoparticles as Recyclable Catalysts: The Frontier between Homogeneous and Heterogeneous Catalysis. *Angew. Chem., Int. Ed.* **2005**, 44, 7852–7872.
- (2) Chen, T.; Rodionov, V. O. Controllable Catalysis with Nanoparticles: Bimetallic Alloy Systems and Surface Adsorbates. *ACS Catal.* **2016**, *6*, 4025–4033.
- (3) Crooks, R. M.; Zhao, M.; Sun, L.; Chechik, V.; Yeung, L. K. Dendrimer-Encapsulated Metal Nanoparticles: Synthesis, Characterization, and Applications to Catalysis. *Acc. Chem. Res.* **2001**, *34*, 181–190
- (4) Zhao, S.; Jin, R.; Jin, R. Opportunities and Challenges in  $\rm CO_2$  Reduction by Gold- And Silver-Based Electrocatalysts: From Bulk Metals To Nanoparticles and Atomically Precise Nanoclusters. *ACS Energy Lett.* **2018**, 3, 452–462.
- (5) Eguchi, D.; Sakamoto, M.; Teranishi, T. Ligand Effect on the Catalytic Activity of Porphyrin-Protected Gold Clusters in the Electrochemical Hydrogen Evolution Reaction. *Chem. Sci.* **2018**, *9*, 261–265.
- (6) Cao, S.; Tao, F.; Tang, Y.; Li, Y.; Yu, J. Size- and Shape-Dependent Catalytic Performances of Oxidation and Reduction Reactions on Nanocatalysts. *Chem. Soc. Rev.* **2016**, *45*, 4747–4765.
- (7) Gabrielli, L.; Rosa-Gastaldo, D.; Salvia, M.-V.; Springhetti, S.; Rastrelli, F.; Mancin, F. Detection and Identification of Designer Drugs by Nanoparticle-Based NMR Chemosensing. *Chem. Sci.* **2018**, 9, 4777–4784.
- (8) Webb, J. A.; Bardhan, R. Emerging Advances in Nanomedicine with Engineered Gold Nanostructures. *Nanoscale* **2014**, *6*, 2502–2530.
- (9) Mozaffari, S.; Li, W.; Dixit, M.; Seifert, S.; Lee, B.; Kovarik, L.; Mpourmpakis, G.; Karim, A. M. The Role of Nanoparticle Size and Ligand Coverage in Size Focusing of Colloidal Metal Nanoparticles. *Nanoscale Adv.* **2019**, *1*, 4052–4066.
- (10) Ahmadi, T. S.; Wang, Z. L.; Green, T. C.; Henglein, A.; El-Sayed, M. A. Shape-Controlled Synthesis of Colloidal Platinum Nanoparticles. *Science* **1996**, *272*, 1924–1925.
- (11) Somorjai, G. A.; Park, J. Y. Colloid Science of Metal Nanoparticle Catalysts in 2D and 3D Structures. Challenges of Nucleation, Growth, Composition, Particle Shape, Size Control and Their Influence on Activity and Selectivity. *Top. Catal.* **2008**, *49*, 126–135
- (12) Jin, R.; Qian, H.; Wu, Z.; Zhu, Y.; Zhu, M.; Mohanty, A.; Garg, N. Size Focusing: A Methodology for Synthesizing Atomically Precise Gold Nanoclusters. *J. Phys. Chem. Lett.* **2010**, *1*, 2903–2910.
- (13) Baek, J.; Allen, P. M.; Bawendi, M. G.; Jensen, K. F. Investigation of Indium Phosphide Nanocrystal Synthesis Using a High-Temperature and High-Pressure Continuous Flow Microreactor. *Angew. Chem., Int. Ed.* **2011**, *50*, 627–630.
- (14) Hoffmann, R.; Minkin, V. I.; Carpenter, B. K. Ockham's Razor and Chemistry. Bull. Soc. Chim. Fr. 1996, 133, 117–130.
- (15) Chamberlin, T. C. Studies for Students. The Method of Multiple Working Hypotheses. *J. Geol.* **1897**, *5*, 837–848.

- (16) Platt, J. R. Strong Inference: Certain systematic methods of scientific thinking may produce much more rapid progress than others. *Science* **1964**, *146*, 347–353.
- (17) Scott, S. L. The Burden of Disproof. ACS Catal. **2019**, *9*, 4706–4708
- (18) Handwerk, D. R.; Shipman, P. D.; Whitehead, C. B.; Özkar, S.; Finke, R. G. Mechanism-Enabled Population Balance Modeling of Particle Formation en Route to Particle Average Size and Size Distribution Understanding and Control. *J. Am. Chem. Soc.* **2019**, *141*, 15827–15839.
- (19) Handwerk, D. R.; Shipman, P. D.; Whitehead, C. B.; Özkar, S.; Finke, R. G. Particle Size Distributions via Mechanism-Enabled Population Balance Modeling. *J. Phys. Chem. C* **2020**, *124*, 4852–4880.
- (20) Durán, N.; Nakazato, G.; Seabra, A. B. Antimicrobial Activity of Biogenic Silver Nanoparticles, and Silver Chloride Nanoparticles: An Overview and Comments. *Appl. Microbiol. Biotechnol.* **2016**, *100*, 6555–6570.
- (21) Panfil, Y. E.; Oded, M.; Banin, U. Colloidal Quantum Nanostructures: Emerging Materials for Display Applications. *Angew. Chem., Int. Ed.* **2018**, 57, 4274–4295.
- (22) Das, K.; Baruah, S. Quantum Dots for Solar Energy Harvesting. *Curr. Sci.* **2018**, *115*, 659–668.
- (23) Jing, L.; Kershaw, S. V.; Li, Y.; Huang, X.; Li, Y.; Rogach, A. L.; Gao, M. Aqueous Based Semiconductor Nanocrystals. *Chem. Rev.* **2016**, *116*, 10623–10730.
- (24) Wu, L.; Lian, H.; Willis, J. J.; Goodman, E. D.; McKay, I. S.; Qin, J.; Tassone, C. J.; Cargnello, M. Tuning Precursor Reactivity toward Nanometer-Size Control in Palladium Nanoparticles Studied by in Situ Small Angle X-ray Scattering. *Chem. Mater.* **2018**, *30*, 1127–1135.
- (25) Finney, E. E.; Finke, R. G. Nanocluster Nucleation and Growth Kinetic and Mechanistic Studies: A Review Emphasizing Transition-Metal Nanoclusters. *J. Colloid Interface Sci.* **2008**, *317*, 351–374.
- (26) Polte, J. Fundamental Growth Principles of Colloidal Metal Nanoparticles—A New Perspective. *CrystEngComm* **2015**, 17, 6809—6820
- (27) Turkevich, J.; Stevenson, P. C.; Hillier, J. A Study of the Nucleation and Growth Processes in the Synthesis of Colloidal Gold. *Discuss. Faraday Soc.* **1951**, *11*, 55–75.
- (28) Turkevich, J.; Stevenson, P. C.; Hillier, J. The Formation of Colloid Gold. *J. Phys. Chem.* **1953**, *57*, 670–673.
- (29) Drews, T. O.; Katsoulakis, M. A.; Tsapatsis, M. A Mathematical Model for Crystal Growth by Aggregation of Precursor Metastable Nanoparticles. *J. Phys. Chem. B* **2005**, *109*, 23879–23887.
- (30) Skrdla, P. J. Use of Dispersive Kinetic Models for Nucleation and Denucleation to Predict Steady-State Nanoparticle Size Distributions and the Role of Ostwald Ripening. *J. Phys. Chem. C* **2012**, *116*, 214–225.
- (31) Tong, F.; Hanson, M. P.; Bardeen, C. J. Analysis of Reaction Kinetics in the Photomechanical Molecular Crystal 9-methylanthracene Using an Extended Finke-Watzky Model. *Phys. Chem. Chem. Phys.* **2016**, *18*, 31936–31945.
- (32) Mozaffari, S.; Li, W.; Thompson, C.; Ivanov, S.; Seifert, S.; Lee, B.; Kovarik, L.; Karim, A. M. Colloidal Nanoparticle Size Control: Experimental and Kinetic Modeling Investigation of the Ligand–Metal Binding Role in Controlling the Nucleation and Growth Kinetics. *Nanoscale* **2017**, *9*, 13772–13785.
- (33) McMurtry, B. M.; Qian, K.; Teglasi, J. K.; Swarnakar, A. K.; De Roo, J.; Owen, J. S. Continuous Nucleation and Size Dependent Growth Kinetics of Indium Phosphide Nanocrystals. *Chem. Mater.* **2020**, *32*, 4358–4368.
- (34) Harada, M.; Asakura, K.; Toshima, N. Structural Analysis of Polymer-Protected Platinum/Rhodium Bimetallic Clusters Using Extended X-ray Absorption Fine Structure Spectroscopy. Importance of Microclusters for the Formation of Bimetallic Clusters. *J. Phys. Chem.* **1994**, *98*, 2653–2662.
- (35) Calandra, P.; Giordano, C.; Longo, A.; Liveri, V. T. Physiochemical Investigation of Surfactant-Coated Gold Nano-

- particles Synthesized in the Confined Space of Dry Reversed Micelles. *Mater. Chem. Phys.* **2006**, *98*, 494–499.
- (36) Harada, M.; Einaga, H. In Situ XAFS Studies of Au Particle Formation by Photoreduction in Polymer Solutions. *Langmuir* **2007**, 23, 6536–6543.
- (37) Meneau, F.; Sankar, G.; Morgante, N.; Cristol, S.; Catlow, C. R. A.; Thomas, J. M.; Greaves, G. N. Characterization of Zinc Oxide Nanoparticles Encapsulated into Zeolite-Y: An In-Situ Combined X-ray Diffraction, XAFS, and SAXS Study. *Nucl. Instrum. Methods Phys. Res., Sect. B* **2003**, *199*, 499–503.
- (38) Abécassis, B.; Testard, F.; Kong, Q.; François, B.; Spalla, O. Influence of Monomer Feeding on a Fast Gold Nanoparticles Synthesis: Time-Resolved XANES and SAXS Experiments. *Langmuir* **2010**, *26*, 13847–13854.
- (39) Karim, A. M.; Al Hasan, N.; Ivanov, S.; Siefert, S.; Kelly, R. T.; Hallfors, N. G.; Benavidez, A.; Kovarik, L.; Jenkins, A.; Winans, R. E.; Datye, A. K. Synthesis of 1 nm Pd Nanoparticles in a Microfluidic Reactor: Insights from in Situ X-ray Absorption Fine Structure Spectroscopy and Small-Angle X-ray Scattering. *J. Phys. Chem. C* **2015**, *119*, 13257–13267.
- (40) Chen, X.; Schröder, J.; Hauschild, S.; Rosenfeldt, S.; Dulle, M.; Förster, S. Simultaneous SAXS/WAXS/UV-Vis Study of the Nucleation and Growth of Nanoparticles: A Test of Classical Nucleation Theory. *Langmuir* **2015**, *31*, 11678–11691.
- (41) Yang, L.; Cheng, H.; Jiang, Y.; Huang, T.; Bao, J.; Sun, Z.; Jiang, Z.; Ma, J.; Sun, F.; Liu, Q.; Yao, T.; Deng, H.; Wang, S.; Zhu, M.; Wei, S. In Situ Studies on Controlling An Atomically-Accurate Formation Process of Gold Nanoclusters. *Nanoscale* **2015**, *7*, 14452–14459.
- (42) Cormary, B.; Li, T.; Liakakos, N.; Peres, L.; Fazzini, P.-F.; Blon, T.; Respaud, M.; Kropf, A. J.; Chaudret, B.; Miller, J. T.; Mader, E. A.; Soulantica, K. Concerted Growth and Ordering of Cobalt Nanorod Arrays as Revealed by Tandem in Situ SAXS-XAS Studies. *J. Am. Chem. Soc.* **2016**, *138*, 8422–8431.
- (43) Sandoe, H. E.; Watzky, M. A.; Diaz, S. A. Experimental Probes of Silver Metal Nanoparticle Formation Kinetics: Comparing Indirect Versus More Direct Methods. *Int. J. Chem. Kinet.* **2019**, *51*, 861–871.
- (44) Georgiev, P.; Bojinova, A.; Kostova, B.; Momekova, D.; Bjornholm, T.; Balashev, K. Implementing Atomic Force Microscopy (AFM) for Studying Kinetics of Gold Nanoparticle's Growth. *Colloids Surf., A* **2013**, 434, 154–163.
- (45) Lin, Y.; Finke, R. G. Novel Polyoxoanion- and Bu<sub>4</sub>N<sup>+</sup>-Stabilized, Isolable, and Redissolvable, 20-30 Å Ir<sub>~300-900</sub> Nanoclusters: The Kinetically Controlled Synthesis, Characterization, and Mechanism of Formation of Organic Solvent-Soluble, Reproducible Size, and Reproducible Catalytic Activity Metal Nanoclusters. *J. Am. Chem. Soc.* **1994**, *116*, 8335–8353.
- (46) Lin, Y.; Finke, R. G. A More General Approach to Distinguishing "Homogeneous" from "Heterogeneous" Catalysis: Discovery of Polyoxoanion- and  $Bu_4N^+$ -Stabilized, Isolable and Redissolvable, High Reactivity  $Ir_{\sim 190-450}$  Nanocluster Catalysts. *Inorg. Chem.* 1994, 33, 4891–4910.
- (47) Özkar, S.; Finke, R. G. Nanoparticle Nucleation Is Termolecular in Metal and Involves Hydrogen: Evidence for a Kinetically Effective Nucleus of Three {Ir<sub>3</sub>H<sub>2</sub>,•P<sub>2</sub>W<sub>15</sub>Nb<sub>3</sub>O<sub>62</sub>}6<sup>-</sup> in Ir(0)<sub>n</sub> Nanoparticle Formation From [(1,5-COD)Ir<sup>1</sup>•P<sub>2</sub>W<sub>15</sub>Nb<sub>3</sub>O<sub>62</sub>]-8<sup>-</sup> Plus Dihydrogen. *J. Am. Chem. Soc.* **2017**, *139*, 5444–5457. Please also see the references therein
- (48) Edlund, D. J.; Saxton, R. J.; Lyon, D. K.; Finke, R. G. Trisubstituted Heteropolytungstates as Soluble Metal Oxide Analogs. 4. The Synthesis and Characterization of Organic Solvent-Soluble  $(Bu_4N)_{12}H_4P_4W_{30}Nb_6O_{123}$  and  $(Bu_4N)_9P_2W_{15}Nb_3O_{62}$  and Solution Spectroscopic and Other Evidence for the Supported Organometallic Derivatives  $(Bu_4N)_7[(C_5Me_5)Rh\bullet P_2W_{15}Nb_3O_{62}]$  and  $(Bu_4N)_7[(C_6H_6)Ru\bullet P_2W_{15}Nb_3O_{62}]$ . Organometallics 1988, 7, 1692–1704. Please also see the references cited therein
- (49) Ott, L. S.; Finke, R. G. Transition-Metal Nanocluster Stabilization for Catalysis: A Critical Review of Ranking Methods and Putative Stabilizers. *Coord. Chem. Rev.* **2007**, *251*, 1075–1100.

- (50) Yih, K.-H.; Hamdemir, I. K.; Mondloch, J. E.; Bayram, E.; Özkar, S.; Vasić, R.; Frenkel, A. I.; Anderson, O. P.; Finke, R. G. Synthesis and Characterization of  $[Ir(1,5-Cyclooctadiene)(\mu-H)]_4$ : A Tetrametallic  $Ir_4H_4$ -Core, Coordinatively Unsaturated Cluster. *Inorg. Chem.* **2012**, *51*, 3186–3193.
- (51) Laxson, W. W.; Özkar, S.; Folkman, S.; Finke, R. G. The Story of a Mechanism-Based Solution to an Irreproducible Synthesis Resulting in an Unexpected Closed-System Requirement for the LiBEt<sub>3</sub>H-Based Reduction: The Case of the Novel Subnanometer Cluster,  $[Ir(1,5\text{-COD})(\mu\text{-H})]_4$ , and the Resulting Improved, Independently Repeatable, Reliable Synthesis. *Inorg. Chim. Acta* **2015**, 432, 250–257.
- (52) Watzky, M. A.; Finke, R. G. Transition Metal Nanocluster Formation Kinetic and Mechanistic Studies. A New Mechanism When Hydrogen Is the Reductant: Slow, Continuous Nucleation and Fast Autocatalytic Surface Growth. *J. Am. Chem. Soc.* **1997**, *119*, 10382–10400. This and a number of our later papers  $^{54-63}$  also check the precursor, A = {(1,5-COD)Ir^I-POM}<sup>8-</sup> conversion by GLC monitoring of the COA produced due to hydrogenation of the 1,5-COD ligand in the precursor, A, under the reaction conditions
- (53) Field, R. J.; Noyes, R. M. Oscillations in Chemical Systems. 18. Mechanisms of Chemical Oscillators: Conceptual Bases. *Acc. Chem. Res.* 1977, 10, 214–221.
- (54) Widegren, J. A.; Aiken, J. D., III; Özkar, S.; Finke, R. G. Additional Investigations of a New Kinetic Method To Follow Transition-Metal Nanocluster Formation, Including the Discovery of Heterolytic Hydrogen Activation in Nanocluster Nucleation Reactions. *Chem. Mater.* **2001**, *13*, 312–324. In the main text of this reference, see Figure 7 and Scheme 2 in comparison to Supporting Information Figure E to see the simulated effect of introducing a hypothetical Ir<sub>13</sub> CEN90 before the CHCRR could begin or, presumably, before COA evolution as monitored by GLC could begin
- (55) Özkar, S.; Finke, R. G. Transition-Metal Nanocluster Stabilization Fundamental Studies: Hydrogen Phosphate as a Simple, Effective, Readily Available, Robust, and Previously Unappreciated Stabilizer for Well-Formed, Isolable, and Redissolvable Ir(0) and Other Transition-Metal Nanoclusters. *Langmuir* **2003**, *19*, 6247–6260.
- (56) Hornstein, B. J.; Finke, R. G. Transition-Metal Nanocluster Kinetic and Mechanistic Studies Emphasizing Nanocluster Agglomeration: Demonstration of a Kinetic Method That Allows Monitoring All Three Phases of Nanocluster Formation and Aging. *Chem. Mater.* **2004**, *16*, 139–150. (See also the addition/correction: Chem. Mater. 2004, *16*, 3972.)
- (57) Besson, C.; Finney, E. E.; Finke, R. G. A Mechanism for Transition-Metal Nanoparticle Self-Assembly. *J. Am. Chem. Soc.* **2005**, 127, 8179–8184.
- (58) Besson, C.; Finney, E. E.; Finke, R. G. Nanocluster Nucleation, Growth and Then Agglomeration Kinetic and Mechanistic Studies: A More General, Four-Step Mechanism Involving Double Autocatalysis. *Chem. Mater.* **2005**, *17*, 4925–4938.
- (59) Finney, E. E.; Finke, R. G. The Four-Step, Double-Autocatalytic Mechanism for Transition-Metal Nanocluster Nucleation, Growth and Then Agglomeration: Metal, Ligand, Concentration, Temperature, and Solvent Dependency Studies. *Chem. Mater.* **2008**, 20, 1956–1970.
- (60) Kent, P. D.; Mondloch, J. E.; Finke, R. G. A Four-Step Mechanism for the Formation of Supported-Nanoparticle Heterogeneous Catalysts in Contact with Solution: The Conversion of  $Ir(1,5-COD)Cl/\gamma-Al_2O_3$  to  $Ir(0)_{\sim 170}/\gamma-Al_2O_3$ . *J. Am. Chem. Soc.* **2014**, *136*, 1930–1941.
- (61) Laxson, W. W.; Finke, R. G. Nucleation is Second Order: An Apparent Kinetically Effective Nucleus of Two for Ir(0)<sub>n</sub> Nanoparticle Formation From [(1,5-COD)Ir<sup>I</sup>•P<sub>2</sub>W<sub>15</sub>Nb<sub>3</sub>O<sub>62</sub>]8<sup>-</sup> Plus Hydrogen. *J. Am. Chem. Soc.* **2014**, *136*, 17601−17615. Please also see the references therein to the importance of nucleation to particle formation reaction across nature, the difficulties in measuring nucleation kinetics and their rate constants, hence the rarity of detailed nucleation mechanisms, and now also the emerging paradigm

- of low-molecularity nucleation in at least strong-bonding chemical systems. The emerging importance of and references to prenucleation clusters are provided in a recent review, <sup>65</sup> along with a discussion of the issue of if such clusters are on vs off the kinetically dominant pathway. <sup>65</sup>
- (62) Özkar, S.; Finke, R. G. Dust Effects On Nucleation Kinetics and Nanoparticle Product Size Distributions: Illustrative Case Study of a Prototype  ${\rm Ir}(0)_{\rm n}$  Transition-Metal Nanoparticle Formation System. Langmuir 2017, 33, 6550–6562. Please also see also the list of references in this paper to the history and prior key literature on the effects of dust on particle formation and nucleation kinetics
- (63) Whitehead, C. B.; Finke, R. G. Nucleation Kinetics and Molecular Mechanism in Transition-Metal Nanoparticle Formation: The Intriguing, Informative Case of a Bimetallic Precursor, {[(1,5-COD)Ir⁴•HPO₄]₂}²-. Chem. Mater. 2019, 31, 2848–2862.
- (64) Whitehead, C. B.; Özkar, S.; Finke, R. G. LaMer's 1950 Model for Particle Formation of Instantaneous Nucleation and Diffusion-Controlled Growth: A Historical Look at the Model's Origins, Assumptions, Equations, and Underlying Sulfur Sol Formation Kinetics Data. *Chem. Mater.* **2019**, *31*, 7116–7132.
- (65) Whitehead, C. B.; Özkar, S.; Finke, R. G. LaMer's 1950 Model of Particle Formation: A Review and Critical Analysis of Its Classical Nucleation and Fluctuation Theory Basis, of Competing Models and Mechanisms for Phase-Changes and Particle Formation, and then of Its Application to Silver Halide, Semiconductor, Metal, and Metal-Oxide Nanoparticles. *Mater. Adv.* 2021, 2, 186–235. See also the extensive list of references therein
- (66) LaMer, V. K.; Dinegar, R. H. Theory, Production and Mechanism of Formation of Monodispersed Hydrosols. *J. Am. Chem. Soc.* **1950**, 72, 4847–4854.
- (67) Patakfalvi, R.; Papp, S.; Dékány, I. The Kinetics of Homogeneous Nucleation of Silver Nanoparticles Stabilized by Polymers. J. Nanopart. Res. 2007, 9, 353–364.
- (68) Kytsya, A.; Bazylyak, L.; Simon, P.; Zelenina, I.; Antonyshyn, I. Kinetics of Ag<sub>300</sub> Nanoclusters Formation: The Catalytically Effective Nucleus Via a Steady-State Approach. *Int. J. Chem. Kinet.* **2019**, *51*, 266–273.
- (69) Moiraghi, R.; Douglas-Gallardo, O. A.; Coronado, E. A.; Macagno, V. A.; Pérez, M. A. Gold Nucleation Inhibition by Halide Ions: A Basis for Seed-Mediated Approach. *RSC Adv.* **2015**, *5*, 19329–19336.
- (70) Munnik, P.; de Jongh, P. E.; de Jong, K. P. Recent Developments in the Synthesis of Supported Catalysts. *Chem. Rev.* **2015**, *115*, *6687*–*6718*.
- (71) Scheeren, C. W.; Machado, G.; Dupont, J.; Fichtner, P. F. P.; Texeira, S. R. Nanoscale Pt(0) Particles Prepared in Imidazolium Room Temperature Ionic Liquids: Synthesis from an Organometallic Precursor, Characterization, and Catalytic Properties in Hydrogenation Reactions. *Inorg. Chem.* **2003**, *42*, 4738–4742.
- (72) Jaska, C. A.; Manners, I. Heterogeneous or Homogeneous Catalysis? Mechanistic Studies of the Rhodium-Catalyzed Dehydrocoupling of Amine-Borane and Phosphine-Borane Adducts. *J. Am. Chem. Soc.* **2004**, *126*, 9776–9785.
- (73) Desforges, A.; Deleuze, H.; Mondain-Monval, O.; Backov, R. Palladium Nanoparticle Generation within Microcellular Polymeric Foam and Size Dependence under Synthetic Conditions. *Ind. Eng. Chem. Res.* **2005**, *44*, 8521–8529.
- (74) Borgia, M. B.; Nickson, A. A.; Clarke, J.; Hounslow, M. J. A Mechanistic Model for Amorphous Protein Aggregation of Immunoglobulin-like Domains. *J. Am. Chem. Soc.* **2013**, *135*, 6456–6464.
- (75) Gillam, J. E.; MacPhee, C. E. Modelling Amyloid Fibril Formation Kinetics: Mechanisms of Nucleation and Growth. *J. Phys.: Condens. Matter* **2013**, 25, 373101.
- (76) Morris, A. M.; Watzky, M. A.; Finke, R. G. Protein Aggregation Kinetics, Mechanism, and Curve-Fitting: A Review of the Literature. *Biochim. Biophys. Acta, Proteins Proteomics* **2009**, 1794, 375–397.

- (77) Chen, D. P.; Fu, J.; Skrabalak, S. E. Towards Shape Control of Metal Oxide Nanocrystals in Confined Molten Media. *ChemNanoMat* **2015**, *1*, 18–26.
- (78) Salzillo, T.; Zaccheroni, S.; Della Valle, R. G.; Venuti, E.; Brillante, A. Micro Raman Investigation of the Photodimerization Reaction of 9-Cyanoanthracene in the Solid State. *J. Phys. Chem. C* **2014**, *118*, 9628–9635.
- (79) Avinash, M. B.; Sandeepa, K. V.; Govindaraju, T. Emergent Behaviors in Kinetically Controlled Dynamic Self-Assembly of Synthetic Molecular Systems. ACS Omega 2016, 1, 378–387.
- (80) Oladoja, N. A. A Critical Review of the Applicability of Avrami Fractional Kinetic Equation in Adsorption-Based Water Treatment Studies. *Desalin. Water Treat.* **2015**, *57*, 15813–15825.
- (81) Randolph, A. D. A Population Balance for Countable Entities. *Can. J. Chem. Eng.* **1964**, *42*, 280–281.
- (82) Hulburt, H. M.; Katz, S. Some problems in particle technology. Chem. Eng. Sci. 1964, 19, 555–574.
- (83) Randolph, A. D.; Larson, M. A. The Population Balance. *Theory of Particulate Processes. Analysis and Techniques of Continuous Crystallization*; Academic Press: New York and London, 1971; Vol. 46. Page 46 contains McCabe's law, which states that the growth rate is independent of diameter (length) of the particles.
- (84) Ramkrishna, D. The Status of Population Balances. *Rev. Chem. Eng.* 1985, 3, 49–95.
- (85) Ramkrishna, D. Population Balances. Theory and Application to Particulate Systems in Engineering; Academic Press: New York, 2000.
- (86) Ramkrishna, D.; Mahoney, A. W. Population Balance Modeling. Promise for the Future. *Chem. Eng. Sci.* **2002**, *57*, 595–606.
- (87) Aiken, J. D., III; Lin, Y.; Finke, R. G. A Perspective on Nanocluster Catalysis: Polyoxoanion and  $(n-C_4H_9)_4N^+$  Stabilized Ir(0) $_{\sim 300}$  Nanocluster "Soluble Heterogeneous Catalysts". *J. Mol. Catal. A: Chem.* **1996**, *114*, 29–51. See p 33 for the definition of "near-monodisperse" particle-size distributions
- (88) Özkar, S.; Finke, R. G. The Hydrogenphosphate Complex of (1,5-cyclooctadiene)iridium(I), {[Bu₄N][(1,5-COD)Ir•HPO₄]}<sub>n</sub>: Synthesis, Spectroscopic Characterization, and ES-MS of a New, Preferred Precursor to HPO₄2⁻ and Bu₄N⁺ Stabilized Ir(0)<sub>n</sub> Nanoclusters. *J. Organomet. Chem.* **2004**, *689*, 493−501.
- (89) Mondloch, J. E.; Finke, R. G. Kinetic Evidence for Bimolecular Nucleation in Supported-Transition-Metal-Nanoparticle Catalyst Formation in Contact with Solution: The Prototype Ir(1,5-COD)- $Cl/\gamma$ - $Al_2O_3$  to  $Ir(0)_{\sim 600-900}/\gamma$ - $Al_2O_3$  System. ACS Catal. **2012**, 2, 208–205
- (90) Watzky, M. A.; Finney, E. E.; Finke, R. G. Transition-Metal Nanocluster Size vs. Formation Time and the Catalytically Effective Nucleus Number: A Mechanism-Based Treatment. *J. Am. Chem. Soc.* **2008**, *130*, 11959–11969.
- (91) Mondloch, J. E.; Finke, R. G. Supported-Nanoparticle Heterogeneous Catalyst Formation in Contact with Solution: Kinetics and Proposed Mechanism for the Conversion of  $Ir(1,5\text{-COD})Cl/\gamma$   $Al_2O_3$  to  $Ir(0)_{\sim 900}/\gamma$ – $Al_2O_3$ . *J. Am. Chem. Soc.* **2011**, 133, 7744–7756.
- (92) Handwerk, D. R.; Shipman, P. D.; Özkar, S.; Finke, R. G. Dust Effects on Ir(0)<sub>n</sub> Nanoparticle Formation Nucleation and Growth Kinetics and Particle Size-Distributions: Analysis by and Insights from Mechanism-Enabled Population Balance Modeling. *Langmuir* **2020**, 36, 1496–1506.
- (93) Whitehead, C. B.; Watzky, M. A.; Finke, R. G. Burst Nucleation vs Burst Growth in Near-Monodisperse Particle Formation Reactions: A Perspective. *J. Phys. Chem. C* **2020**, *124*, 24543–24554.
- (94) Kulkarni, S. A.; Kadam, S. S.; Meekes, H.; Stankiewicz, A. I.; ter Horst, J. H. Crystal Nucleation Kinetics from Induction Times and Metastable Zone Widths. *Cryst. Growth Des.* **2013**, *13*, 2435–2440.
- (95) Widegren, J. A.; Bennett, M. A.; Finke, R. G. Is It Homogeneous or Heterogeneous Catalysis? Identification of Bulk Ruthenium Metal as the True Catalyst in Benzene Hydrogenations Starting with the Monometallic Precursor,  $Ru(II)(\eta 6C_6Me_6)(OAc)_2$ , Plus Kinetic Characterization of the Heterogeneous Nucleation, Then Autocatalytic Surface-Growth Mechanism of Metal Film Formation. *J.*

- Am. Chem. Soc. 2003, 125, 10301–10310. This work documents the level of error in  $k_{1\text{obs}}$  and  $k_{2\text{obs}}$  one can see when heterogeneous, vs homogeneous, nucleation is involved
- (96) Day, V. W.; Klemperer, W. G.; Main, D. J. Niobotungstate, Nb<sub>2</sub>W<sub>4</sub>O<sub>19</sub>4 and Triphosphate, P<sub>3</sub>O<sub>9</sub>3, Complexes of (cyclooctadiene)-iridium(I): Synthesis, Structure, and Stability of Tetra-nbutylammonium Salts of  $\{[(C_8H_{12})Ir]_5(Nb_2W_4O_{19})_2\}3$ ,  $\{[(C_8H_{12})Ir]_2H(Nb_2W_4O_{19})_2\}5$ , and  $[(C_8H_{12})Ir(P_3O_9)]2$ . Inorg. Chem. 1990, 29, 2345–2355.
- (97) Guthrie, J. P. Hydration and Dehydration of Phosphoric Acid Derivatives: Free Energies of Formation of the Pentacoordinate Intermediates for Phosphate Ester Hydrolysis and of Monomeric Metaphosphate. J. Am. Chem. Soc. 1977, 99, 3991–4001.
- (98) Wazer, J. R. V.; Griffith, E. J.; McCullough, J. F. Hydrolysis of Condensed Phosphates. J. Am. Chem. Soc. 1952, 74, 4977–4978.
- (99) Cotton, F. A.; Wilkinson, G. Advanced Inorganic Chemistry, 5th ed.; John Wiley & Sons: New York, 1988.
- (100) Ramirez, F.; Marecek, J. F. Oxyphosphorane and Monomeric Metaphosphate Ion Intermediates in Phosphoryl Transfer from 2,4-Dinitrophenyl Phosphate in Aprotic and Protic Solvents. *J. Am. Chem. Soc.* 1979, 101, 1460–1465.
- (101) Newville, M. IFEFFIT: Interactive XAFS Analysis and FEFF Fitting. J. Synchrotron Radiat. 2001, 8, 322–324.
- (102) Frenkel, A. I.; Kleifeld, O.; Wasserman, S. R.; Sagi, I. Phase Speciation by Extended X-ray Absorption Fine Structure Spectroscopy. *J. Chem. Phys.* **2002**, *116*, 9449–9456.
- (103) Wang, Q.; Hanson, J. C.; Frenkel, A. I. Solving the Structure of Reaction Intermediates by Time-Resolved Synchrotron X-ray Absorption Spectroscopy. *J. Chem. Phys.* **2008**, *129*, 234502.
- (104) Dias, E. T.; Gill, S. K.; Liu, Y.; Halstenberg, P.; Dai, S.; Huang, J.; Mausz, J.; Gakhar, R.; Phillips, W. C.; Mahurin, S.; Pimblott, S. M.; Wishart, J. F.; Frenkel, A. I. Radiation-Assisted Formation of Metal Nanoparticles in Molten Salts. *J. Phys. Chem. Lett.* **2021**, *12*, 157–164. An estimate of  $\sim 10^{16}$  solvated electrons result from the rough estimation reported in the Supporting Information of this reference. Therein, it is calculated that 1 photon of 8 keV energy results in the formation of  $\sim 300$  absorbed electrons. Hence, given the observed complete absorption of radiation in the system examined, it was calculated that (300 absorbed electrons/photon)  $\times$  ( $\sim 3 \times 10^{13}$  photons/s) =  $\sim 10^{16}$  solvated electrons per second are produced
- (105) Ma, J.; Zou, Y.; Jiang, Z.; Huang, W.; Li, J.; Wu, G.; Huang, Y.; Xu, H. An In Situ XAFS Study—The Formation Mechanism of Gold Nanoparticles from X-ray-Irradiated Ionic Liquid. *Phys. Chem. Chem. Phys.* **2013**, *15*, 11904—11908.
- (106) Bharti, A.; Bhardwaj, R.; Agrawal, A. K.; Goyal, N.; Gautam, S. Monochromatic X-Ray Induced Novel Synthesis of Plasmonic Nanostructure for Photovoltaic Application. *Sci. Rep.* **2016**, *6*, 22394. (107) Grand, J.; Ferreira, S. R.; de Waele, V.; Mintova, S.; Nenoff, T. M. Nanoparticle Alloy Formation by Radiolysis. *J. Phys. Chem. C* **2018**, *122*, 12573–12588.
- (108) Quinson, J.; Jensen, K. M. Ø. From Platinum Atoms in Molecules to Colloidal Nanoparticles: A Review on Reduction, Nucleation and Growth mechanisms. *Adv. Colloid Interface Sci.* **2020**, 286, 102300.
- (109) Remita, S.; Fontaine, P.; Lacaze, E.; Borensztein, Y.; Sellame, H.; Farha, R.; Rochas, C.; Goldmann, M. X-ray Radiolysis Induced Formation of Silver Nano-Particles: A SAXS and UV-Visible Absorption Spectroscopy Study. *Nucl. Instrum. Methods Phys. Res.*, Sect. B 2007, 263, 436–440.
- (110) Bondaz, L.; Fontaine, P.; Muller, F.; Pantoustier, N.; Perrin, P.; Morfin, I.; Goldmann, M.; Cousin, F. Controlled Synthesis of Gold Nanoparticles in Copolymers Nanomolds by X-ray Radiolysis. *Langmuir* **2020**, *36*, 6132–6144.
- (111) Yamaguchi, A.; Fukuoka, T.; Okada, I.; Ishihara, M.; Sakurai, I.; Utsumi, Y. Caltrop Particles Synthesized by Photochemical Reaction Induced by X-Ray Radiolysis. *J. Synchrotron Radiat.* **2017**, 24, 653–660.
- (112) Stachowski, T. R.; Snell, M. E.; Snell, E. H. SAXS Studies of X-ray Induced Disulfide Bond Damage: Engineering High-Resolution

- Insight from a Low-Resolution Technique. PLoS One 2020, 15, No. e0239702.
- (113) Aiken, J. D., III; Finke, R. G. Nanocluster Formation Synthetic, Kinetic and Mechanistic Studies. The Detection of, and then Methods to Avoid, Hydrogen Mass-Transfer Limitations in the Synthesis of Polyoxoanion- and Tetrabutylammonium- Stabilized, Near Monodisperse  $40 \pm 6$  Å Rh(0) Nanoclusters. *J. Am. Chem. Soc.* 1998, 120, 9545.
- (114) Hoops, S.; Sahle, S.; Gauges, R.; Lee, C.; Pahle, J.; Simus, N.; Singhal, M.; Xu, L.; Mendes, P.; Kummer, U. COPASI-a COmplex PAthway SImulator. *Bioinformatics* **2006**, *22*, 3067–3074.
- (115) Li, T.; Senesi, A. J.; Lee, B. Small Angle X-ray Scattering for Nanoparticle Research. *Chem. Rev.* **2016**, *116*, 11128–11180.
- (116) Sun, Y.; Ren, Y. In Situ Synchrotron X-Ray Techniques for Real-Time Probing of Colloidal Nanoparticles Synthesis. *Part. Part. Syst. Charact.* **2013**, *30*, 399–419.
- (117) Woehrle, G. H.; Hutchison, J. E.; Özkar, S.; Finke, R. G. Analysis of Nanoparticle Transmission Electron Microscopy Data Using a Public- Domain Image-Processing Program, Image. *Turk. J. Chem.* **2006**, *30*, 1–13.
- (118) Bentea, L.; Watzky, M. A.; Finke, R. G. Sigmoidal Nucleation and Growth Curves Across Nature Fit by the Finke—Watzky Model of Slow Continuous Nucleation and Autocatalytic Growth: Explicit Formulas for the Lag and Growth Times Plus Other Key Insights. *J. Phys. Chem. C* 2017, 121, 5302—5312.
- (119) Kerker, M.; Daby, E.; Cohen, G. L.; Kratohvil, J. P.; Matijevic, E. Particle Size Distribution in LaMer Sulfur Sols. *J. Phys. Chem.* **1963**, 67, 2105–2111.
- (120) Petro, A. J. Particle Size Distribution in Monodisperse Sulfur Hydrosols. *J. Phys. Chem.* **1960**, *64*, 1508–1511.
- (121) Nucleation—a Transition State to the Directed Assembly of Materials; Faraday Discussions; Royal Society of Chemistry: U.K., 2015; Vol. 179, pp 9–557.
- (122) Spurny, K. R. Atmospheric Condensation Nuclei P. J. Coulier 1875 and J. Aitken 1880 (Historical Review). *Aerosol Sci. Technol.* **2000**, 32, 243–248.
- (123) Coulier, P. J. Note Sur Une Nouvelle Propriete de L'air. J. Pharm. Chim. 1875, 4, 165–173.
- (124) Aitken, J. On the Dust, Fog, and Clouds. Proc. R. Soc. 1882, 11, 14–18.
- (125) Aitken, J. On the Numbers of Dust Particles in the Atmosphere in Certain Places in Great Britain and on the Continent, with Remarks on the Relation Between the Amount of Dust and Meteorological Phenomena. *Trans. R. Soc. Edinburgh: Earth Sci.* **1889**, 35, 1–19.
- (126) Aitken, J. On Improvements in the Apparatus for Counting the Dust Particles in the Atmosphere. *Proc. R. Soc.* **1890**, *16*, 135–172.
- (127) Aitken, J. On a Simple Pocket Dust-Counter. *Proc. R. Soc.* **1892**, *18*, 39–52.
- (128) Wilson, C. T. R. Condensation of Water Vapour in the Presence of Dust-Free Air and Other Gases. *Philos. Trans. R. Soc. London* **1897**, *189*, 265–307.
- (129) Kent, P.; Mondloch, J. E.; Finke, R. G. Synthesis of Heterogeneous  $Ir0_{\sim 600-900}/\gamma$ -Al<sub>2</sub>O<sub>3</sub> in One Pot From the Precatalyst  $Ir(1,5\text{-COD})Cl/\gamma$ -Al<sub>2</sub>O<sub>3</sub>: Discovery of Two Competing Trace "Ethyl Acetate Effects" on the Nucleation Step and Resultant Product. *ACS Catal.* **2016**, *6*, 5449–5461.
- (130) Oxtoby, D. W. Homogeneous nucleation: theory and experiment. J. Phys.: Condens. Matter 1992, 4, 7627–7650.
- (131) Whitehead, C. B.; Finke, R. G. A Review of Metal, Metal-Oxide, and Semiconductor Nanoparticle Formation Based on In Situ Synchrotron XAFS and SAXS Investigations En Route to Reliable Minimum Mechanisms. 2021, submitted for publication.
- (132) Timoshenko, J.; Frenkel, A. I. "Inverting" X-ray Absorption Spectra of Catalysts by Machine Learning in Search for Activity Descriptors. ACS Catal. 2019, 9, 10192–10211.
- (133) Timoshenko, J.; Lu, D.; Lin, Y.; Frenkel, A. I. Supervised Machine-Learning-Based Determination of Three-Dimensional Struc-

- ture of Metallic Nanoparticles. J. Phys. Chem. Lett. 2017, 8, 5091–5098.
- (134) Marcella, N.; Liu, Y.; Timoshenko, J.; Guan, E.; Luneau, M.; Shirman, T.; Plonka, A. M.; van der Hoeven, J. E. S.; Aizenberg, J.; Friend, C. M.; Frenkel, A. I. Neural Network Assisted Analysis of Bimetallic Nanocatalysts Using X-ray Absorption Near Edge Structure Spectroscopy. *Phys. Chem. Chem. Phys.* **2020**, *22*, 18902–18910.
- (135) Liu, Y.; Marcella, N.; Timoshenko, J.; Halder, A.; Yang, B.; Kolipaka, L.; Pellin, M. J.; Seifert, S.; Vajda, S.; Liu, P.; Frenkel, A. I. Mapping XANES Spectra on Structural Descriptors of Copper Oxide Clusters Using Supervised Machine Learning. *J. Chem. Phys.* **2019**, *151*, 164201.
- (136) Timoshenko, J.; Halder, A.; Yang, B.; Seifert, S.; Pellin, M. J.; Vajda, S.; Frenkel, A. I. Subnanometer Substructures in Nanoassemblies Formed from Clusters under a Reactive Atmosphere Revealed Using Machine Learning. *J. Phys. Chem. C* **2018**, 122, 21686–21693.
- (137) Frenkel, A. I.; Hills, C. W.; Nuzzo, R. G. A View from the Inside: Complexity in the Atomic Scale Ordering of Supported Metal Nanoparticles. *J. Phys. Chem. B* **2001**, *105*, 12689–12703.
- (138) Frenkel, A. I. Solving the Structure of Nanoparticles by Multiple-Scattering EXAFS Analysis. *J. Synchrotron Radiat.* **1999**, *6*, 293–295.
- (139) Frenkel, A. I. Applications of Extended X-ray Absorption Fine-Structure Spectroscopy to Studies of Bimetallic Nanoparticle Catalysts. *Chem. Soc. Rev.* **2012**, *41*, 8163–8178.
- (140) Roese, S.; Kononov, A.; Timoshenko, J.; Frenkel, A. I.; Hövel, H. Cluster Assemblies Produced by Aggregation of Preformed Ag Clusters in Ionic Liquids. *Langmuir* **2018**, *34*, 4811–4819.
- (141) Timoshenko, J.; Roese, S.; Hövel, H.; Frenkel, A. I. Silver Clusters Shape Determination from In-Situ XANES Data. *Radiat. Phys. Chem.* **2020**, *175*, 108049.
- (142) Che, M.; Bennett, C. O. The Influence of Particle Size on the Catalytic Properties of Supported Metals. *Adv. Catal.* **1989**, *36*, 55–172. See p 110, Figure 9 for example
- (143) Finke, R. G.; Watzky, M. A.; Whitehead, C. B. Response to: Particle Size is a Primary Determinant for Sigmoidal Kinetics of Nanoparticle Formation: A "disproof" of the Finke-Watzky (F-W) nanoparticle nucleation and growth mechanism. *Chem. Mater.* **2020**, 32, 3657–3672.
- (144) Kathmann, S. M.; Schenter, G. K.; Garrett, B. C. Understanding the Sensitivity of Nucleation Kinetics. *J. Chem. Phys.* **2002**, *116*, 5046–5057.
- (145) Kathmann, S. M.; Schenter, G. K.; Garrett, B. C.; Chen, B.; Siepmann, J. I. Thermodynamics and Kinetics of Nanoclusters Controlling Gas-to-Particle Nucleation. *J. Phys. Chem. C* **2009**, *113*, 10354–10370. See also the refs 16, 25–37 therein concerning DFT studies that strive to go beyond classical nucleation theory